OPTICAL PROPERTIES OF AMORPHOUS
MAGNESIUM-BISMUTH ALLOYS

BY

IBRAHIM M. ODEH

A thesis submitted for the degree of M.Sc., to the
University of Glasgow.   May, 1978.

TO THE ODEHS

A B S T R A C T

The amorphous magnesium-bismuth alloys were prepared by the co-evaporation technique . The compositions of these alloys were determined from the rate of deposition of the two constituents using the quartz crystal oscillators. A new method to calculate the densities of the alloys from the rates of deposition is outlined. The electrical measurements of the d.c. resistivity shows that the Mg-Bi alloys close to the stoichiometric composition Mg_3Bi_2 has a very high resistivity. From the optical measurements, the stoichiometric Mg_3Bi_2 compound is found to have an optical band gap 0.264 ∓ 0.006 ev. The dramatic changes in the optical band gap due to annealing make the proposed model densities of states of doubtful relevance

ACKNOWLEDGEMENTS

I should like to thank Professor R.P. Ferrier for giving me the opportunity to carry out this work at the Department of Natural Philosophy.

I am grateful to Dr. A.R. Long for his continued advice, help and encouragement during the course of this work. Dr. Long has also given me his valuable time during the writing of this thesis.

I wish to thank the technical staff of the Solid State Physics Group, D. Blackwell, G. MacGregor, D. MacDonald, and A. Young in the workshop for constructing the sample insert and the crystal holders and the help during this work.

My thanks are due to Mrs. M. Blackwell for typing this thesis.

During my stay in Glasgow, I have been financially supported by my brothers Fuad Odeh, Isa Odeh and Abdul-Fattah Odeh. To them and to my parents I am grateful.

C O N T E N T S

C H A P T E R   1

I N T R O D U C T I O N

There has been a considerable and growing interest
in theoretical and experimental investigation of the
properties of non-crystalline materials during the last
decade.   Their interesting properties and possible tech-
nological applications have led to research to elucidate
these properties.

In this work amorphous Magnesium-Bismuth alloy films
were prepared and some optical and electrical measurements
were made on this system.

1.1   Crystalline and Non-crystalline materials:

Crystalline solids have been extensively studied, and
very well established theories have been available to
explain their electronic, thermal and optical properties.
A perfect crystal is constructed by the infinite regular
repetition in space (Lattice) of identical structural units.
In the case of crystalline materials, the electrons are
usually described in terms of plane wave functions of the
type

$$\psi_k(r) = e^{ik \cdot r}$$

where   k   is the wave vector (Free electron model).
When the electron wave is Bragg reflected at the Lattice
positions, at particular values of k (k = $\mp n\pi/a$,   n   is an

integer and a is the interatomic spacing in one dimension),
then standing waves will be created and travel in opposite
directions.   These standing waves pile up electrons at
different regions relative to the ions, due to which the
difference between the potential energies gives rise to
the energy gap..   In this way,
the electron states are separated into energy bands each
corresponding to a particular relation between the energy
and the wave vector $\underline{k}$.   From these relations, a density
of electron states (number of states per unit energy) can
be derived.   The distribution of the electrons into energy
bands determines whether a crystal is conductor, insulator
or semiconductor.   However, the description of individual
electron states, labelled by the wave vector $\underline{k}$, used for
crystalline materials, is not appropriate for the non-
crystalline case.   When scattering of electrons is
considered, a mean free path L is introduced.   Assuming
the $kL \gg 1$, $\underline{k}$ remains a good quantum number.   In the
case of noncrystalline materials, where the long range order
of the structural units is lost, though a short range order
is still preserved, we have two possibilities.   One is the
mean free path is large, so that $kL \gg 1$, and wave vector
$\underline{k}$ is still a good quantum number, e.g. in most liquid
metals.   Second, if in a liquid or amorphous material the
atomic potential is strong enough to produce a band gap
and large deviation from the free electron form, then it
must give strong scattering and a short mean free path
$kL \sim 1$.   Under this latter condition, the wave vector $\underline{k}$
is meaningless.   This is responsible for many of the
differences between the theories of crystalline and non-

crystalline materials (Mott and Davis (1971))

Ioffe and Regel (1960) emphasized that values of the mean free path such that $kL < 1$ are impossible. It was first conjectured by Gubanov (1963) and Banyai (1964) that near the edges of conduction or valence bands in most non-crystalline materials the states are localized. This is the new concept applying to amorphous materials alone (Mott and Davis (1971)) , that a continuous density of states, $N(E)$, can exist in which for a range of energies the states are all localized, and for which the mobility at the zero of temperature vanishes, even though the wave functions of neighbouring states overlap.

1.2   Previous Work on Magnesium-Bismuth Alloys:

The electrical and optical properties of Magnesium-Bismuth alloy in liquid, amorphous and crystalline states have been under extensive investigation over the last twenty years. Ilschner and Wagner (1958) reported a minimum in the electrical conductivity for liquid Mg-Bi of composition near 40 at.% Bi. Ferrier and Herrell (1969) studied the electrical conductivity and the thermoelectric power of the amorphous Mg-Bi alloy films as a function composition. They reported a minimum electrical conductivity of the order 10^{-1} ohm^{-1}. cm^{-1} for composition of the stoichiometric composition Mg_3Bi_2. These authors interpreted their results in terms of a rigid band model for the electronic density of states with a pseudogap between the bands, states in the gap being localised. As the composition varied, it was proposed that the fermi level moved through the pseudogap. Sik and Ferrier (1974) have

made further measurements of the electrical and the optical properties of amorphous Mg-Bi alloy system. They have interpreted their results in terms of the same rigid band model proposed by Ferrier and Herrell, and reported an optical gap of the order 0.7 eV. Slowik and Brown (1972) have studied the soft X-ray absorption of these alloys and found sharp exciton lines for alloys of low conductivity. Sutton (1975) has made extensive optical measurements as well as an electrical study. This author emphasized that the optical gap for the amorphous Mg-Bi alloy films near the composition 40 at.% Bi was 0.152 ∓ 0.005 eV. Sutton interpreted his results in terms of a new model for the electronic density of states. He proposed a model for the density of states with parabolic valence and conduction bands tailing exponentially into the gap. Sutton also suggested that the fermi level remained fixed in the pseudo-gap as composition varied, and that away from the conductance minimum at 40 at.% Bi the pseudogap was gradually filled in.

1.3 Plan of Thesis

The aim of this work was to measure the optical and electrical properties of amorphous Mg-Bi alloys particularly alloys with composition near 40 at.% Bi. The annealing effects were also studied and found to involve significant changes in the structure of these alloys. In Chapter 2 we have briefly reviewed the preparation techniques used to prepare the Mg-Bi alloys. The coevaporation method is described. The method used to determine the composition of the alloys is given in detail. Specifically designed

equipment for this research is described in Chapter 3.

A new method of evaluating the density of the coevaporated alloys is described in Chapter 4.   The electrical measurements of the d.c. resistivity as a function of temperature are included in Chapter 4. The last chapter is completely devoted to the optical properties.

C H A P T E R   2

PRINCIPLES OF SAMPLE PREPARATION AND MEASUREMENT

2.1   Review of Preparation Methods:

Amorphous Mg-Bi alloy films have been prepared by a number of different techniques.   In this section we briefly review these techniques.

a. Co-evaporation from two independent sources:

This widely used technique is capable of an overall accuracy of better than 1%, but fluctuations in the composition through the thickness of the film generally occur.   With care these can be kept to about 1%.   This is generally the most successful technique of preparation, and we have used it to prepare our samples.

b. Flash evaporation:

Powders of the two elements are weighed and mixed in the correct ratio,   then spread thinly into a molybdenum tape.   The tape is drawn across two electrodes and a high current of about 100 amp is passed through the ribbon.   As the mixture is drawn onto heated portion, nearly instantaneous evaporation of both constituents takes place.   This method has previously been used successfully to prepare Thallium-Tellurium alloys, (Prado (1972)) .   This author prepared two samples close to Mg_3Bi_2 by this method, but Sik (1974) later concluded that "flash evaporation" is not suitable for Mg-Bi alloy system since magnesium sublimes at high rate

and a large amount of spitting and powder loss occurs.

c. <u>Thermal Evaporation from a Bulk Alloy</u>:

Sik and Ferrier (1974) successfully obtained a range
of compositions close to the intermetallic compound
Mg_3Bi_2 by adding small amount of magnesium to a slightly
bismuth rich melt of Mg_3Bi_2. The conventional method of
weighing out the elements into a cilica tube, which is
then evacuated and placed in a furnace, fails as the mag-
nesium reacts with tube walls to form magnesium silicate
(Sik (1974)). Wallace et. al. (1977) repeated this
method and found that the mixture was bismuth rich as
expected, and further chemical analysis showed signifi-
cant magnesium loss. This method also suffers from
the disadvantage that the alloy composition is not
directly known.

d. <u>R.F. Co-sputtering from a split target</u>:

The phenomenon of sputtering is ejection of atoms from
the surface of material by bombardment with energetic
particles. The energetic particles are provided by
introducing high purity argon into an R.F. glow discharge,
the resulting positive argon ions are accelerated towards
the cathode by the electric field where they impinge on
the target. This technique was investigated by Wallace
et. al. (1977) , who sought to use the expected composi-
tion gradient in the sputtering yield from a split
target in a line perpendicular to the division on it.
The magnesium-bismuth alloy samples were sputtered onto
sapphire substrates, which were kept near liquid nitro-
gen temperature. However, with this method

it has not proved possible to control the sputtering
conditions sufficiently well.

2.2 Preparation of Amorphous Mg-Bi Alloy Films by Co-evaporation Method

Introduction

The amorphous Mg-Bi alloy films investigated in this
work, were prepared by vacuum deposition of the two consti-
tuents evaporated simultaneously from two independent
sources, and quenched onto a substrate cooled down to near
liquid nitrogen temperature. This method has been proved
to produce successfully amorphous Mg-Bi alloy films for
compositions in the 20 - 60 at.% Bi (Ferrier and Herrell
(1969)) . It was also used by Sutton (1975) to generate
thin films for electrical and optical investigations. The
composition of the amorphous alloy samples prepared by this
technique is determined from the rates of deposition of
magnesium and bismuth.

2.2.1 Design of Sources

The two independent sources used to evaporate the two
elements were constructed from Molybdenum foil. The design
of sources is illustrated in figure (2.1).They , gave satis-
factory rates of evaporation at currents approximately 40 amps.
Preliminary tests with open resistance heated sources gave
unsteady and unreproducable rates of evaporation, that was
partly due to sublimation of magnesium. Hence, each
source was covered with a lid, and the evaporants passed
through holes in them. The substrate saw a sufficiently
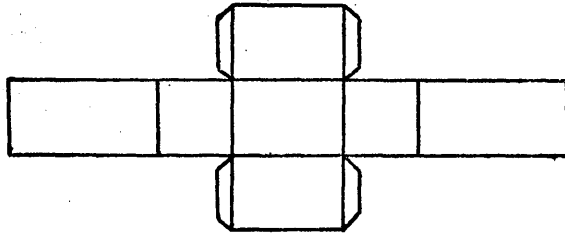
(a)
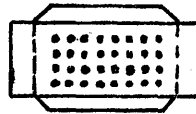
(b)
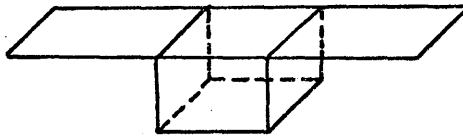
(c)

(d)

Figure (2.1)   Design of evaporation sources.

(a) The Base.   · (b) The Lid

(c) Magnesium Source   (c) Bismuth Source

well defined area of the evaporants through the holes in
the lids.   Each source was heated by a separate power
supply, which was a stepdown transformer driven from a
variac connected across the mains.   The two variacs were
controlled manually to establish the desired rates of
evaporation.   It was noted that if the source current was
held steady (slight adjustment was necessary) the rate of
evaporation tended to stay stable.   The currents were
supplied to the sources through high current feed throughs
attached to the lower section of the vacuum system.   The
two sources were apart from each other, and a copper shield
was placed midway between them, plate (1).

2.2.2 Substrates

Synthetic sapphire (Al_2O_3) was chosen as the substrate
material, for this material has excellent thermal and
optical properties.   The substrate has a thermal conduct-
ivity 200 watt. cm^{-1}. deg^{-1} at $30^{o}K$. It passes radiation
with the wavelength limits 0.17 - 5.5μm, and has absorption
coefficient 1.9 cm^{-1} at 5.35 μm wavelength.   Also sapphire
has excellent homogeniety and extreme surface hardness.   By
using sapphire substrates we were able to make transmission
measurements in the near infra-red region with the sample
held close to liquid nitrogen temperature.

Typical transmittance curve for the substrates used in
the present work together with similar curve from Hackforth
(1960) is shown in figure (2.2).   The quality of the sub-
trate surface proved to be satisfactory after the following
cleaning procedure was carried out to remove any previous
alloy films.   Duraglit was used to remove any alloy films
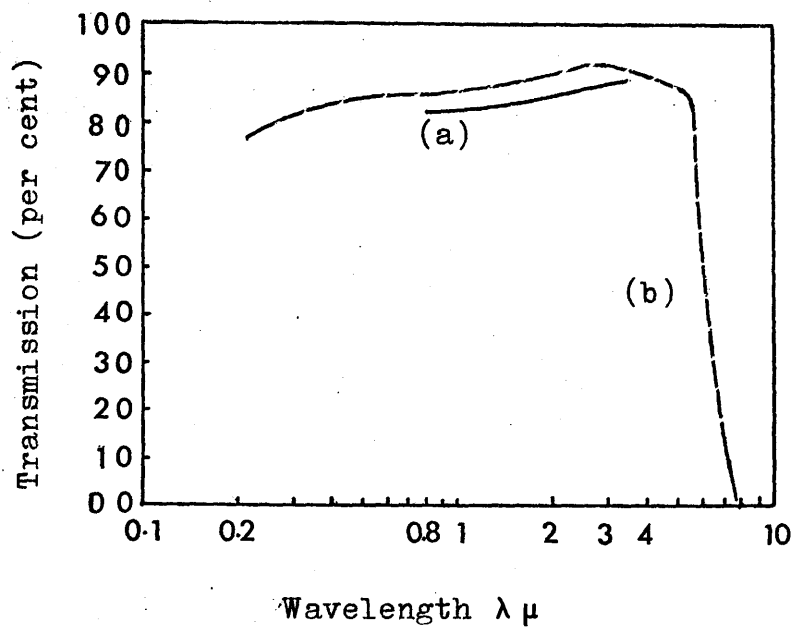
Figure (2.2)   Optical transmission of sapphire substrate

(a)   For substrates used in this work

(b)   From Hackforth (1960)

previously deposited on the substrate followed by immersion in an acetone bath for 5 - 10 minutes. The substrate was rinsed in analar acetone and, then ultrasonically agitated in inhibisol, quadralene and ionised water. The ultrasonic bath speeded up the cleaning procedure. The substrate was left in a hot pure isopropyl alcohol bath to get rid of any further water or grease. This cleaning method proved to be sufficiently adequate to get clean substrates suitable for the optical and electrical measurements. The "Breath Test" was used to test the cleanliness of the substrates. The clean substrates were resistant to forming breath patterns. Any breath pattern formed disappeared quickly and uniformly.

2.3 Deposition Rate Monitor:

2.3.1 Principle of Quartz Crystal Oscillator

In recent years crystal oscillators have been widely used to monitor directly the rates of deposition of evaporated materials. An accurately calibrated crystal oscillator may also be used to determine the thickness of the deposited films. The growing interest in this device is due to its high sensitivity and simplicity. The principle of this device is as follows (Behrndt (1966)) :
If a quartz crystal is excited to thickness shear-oscillation, the thickness of the plate corresponds to a half-wavelength of the fundamental frequency (Mason (1956))

$$f = V_{tr}/2d = N/d .$$ (2.3.1)

where V_{tr} is the velocity of the elastic transverse wave in

the direction of the plate thickness d and N is the
frequency constant.   For AT-cut crystals **N** = 1670 KHz.mm
(Heising (1946)) .   Writing

$$M = d A\rho$$

where M is the mass of the vibrating plate, A is the
plate area and ρ is the density of the quartz.
From equation (2.3.1) we get

$$f = NA\rho /M \qquad\qquad (2.3.2)$$

Differentiation of equation (2.3.2) with respect to M
gives

$$df = -(f_o^2 / NA\rho) . dM \qquad (2.3.3)$$

Where f_o is the starting frequency of the crystal.

$$dM = (NA\rho / -f_o^2) \quad df \qquad (2.3.4)$$

From equations (2.3.3) and (2.3.4) we can see that the
frequency shift is proportional to a small change in mass
of the crystal, and higher starting frequency should be
chosen for thin films applications.   Since an antinode is
formed in thickness-shear oscillations on the surface of
the quartz plate, only the mass of the material deposited
will effect the frequency, provided that dM is sufficiently
small.   This means that a truly "thin" film of any material
will result in the same frequency shift as the equivalent
mass of quartz.

Some of the crystal properties which must be taken
into account when using this device are given here.

a. Sensitivity of the quartz crystal which is
    defined as the frequency change corresponding
    to unit mass deposited on unit are

$$C_{fo} = -(f^2 / N \rho) \quad \text{Hz. cm}^2/\text{gm}$$

b. The minimum detectable mass per unit area for a
    frequency shift $df = 1$ Hz .

$$dM/A = -(df / C_f) \text{ gm/cm}^2$$

c. The permissable frequency shift $(df)_p$ for 1%
    deviation from linearity

$$(df)_p = 5 \times 10^{-3} f \text{ Hz}$$

d. The mass per unit area corresponding to $(df)_p$ is

$$(dM/A)_p = \rho_q N \, df / 0.99 \, f^2$$

For the purpose of monitoring the rates of deposition,
in order to calculate the composition of the alloy films,
At-cut quartz crystals with starting frequency 6MHz were
used.

2.3.2 Crystal Holder

Frequency shifts of the crystals (apart from those
due to mass deposition) may also result due to other
factors (Berhrndt (1966)) , for example, variations of
the surrounding gas pressure change the damping of the
crystal (Pacey (1959)) . However, pressure variation
during the deposition cause negligibly small changes in
frequency. Mechanical shocks are also not of practical

importance if the holder makes the changes of the crystal position impossible. Most serious are frequency shifts due to variations of crystal temperature. Radiation from the sources and condensation of the evaporants causes heating of the crystal which cannot be avoided. To reduce the resultant temperature variations in such a way that does not restrict the flexibility of the technique, a water cooled crystal holder was designed, figure (2.3).

The crystal was clamped to a 2 x 2 x ¼ inch copper plate by a copper cap, which also served as an electrode, and was relieved to a diameter of 3/8" to allow the crystal to vibrate. The sensitive area of the crystal saw a well defined area of the evaporated material through a connical hole. A U-shaped copper tube was attached (hard soldered) to the tope surface of the copper plate, through which the water was passed for a good time prior to and during the alloy preparation. To avoid any mechanical shocks, the holder was clamped to the base plate of the lower section of the vacuum system. The At-cut quartz crystals were supplied with keyhole-shaped gold electrodes deposited on each side. A phosphor bronze. spring was used to clamp down the copper cap, which was in contact with the gold electrode on the top surface of the crystal, and was used as the live electrode. The circuit to the driving oscillator was completed by means of the earth return. A P.T.F.E. ring was clamped to the copper plate in order to keep the copper cap in place. The driving oscillator circuit used is shown in figure (2.4).

Spring and copper electrode

Copper plate

Crystal

Side View

Copper tubes for water cooling

Teflon ring

Copper plate
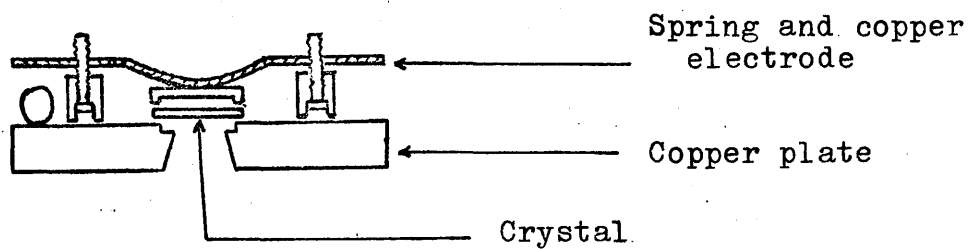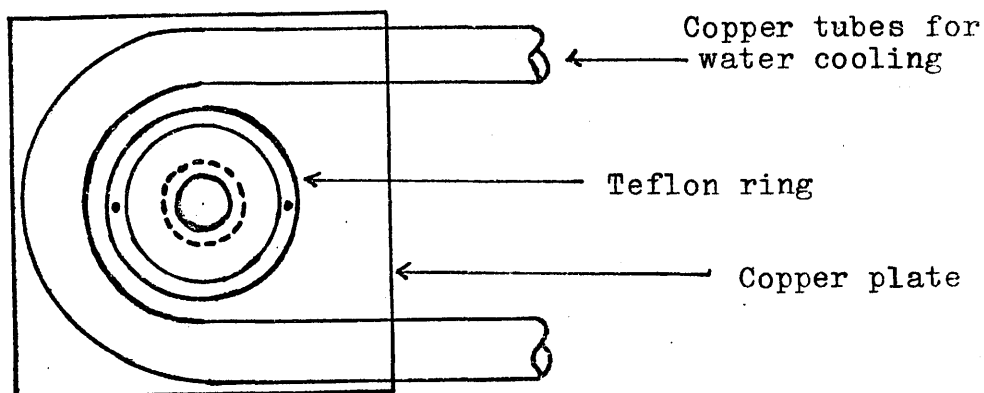
Top View

Figure (2.3) Water-cooled holder for crystal oscillator
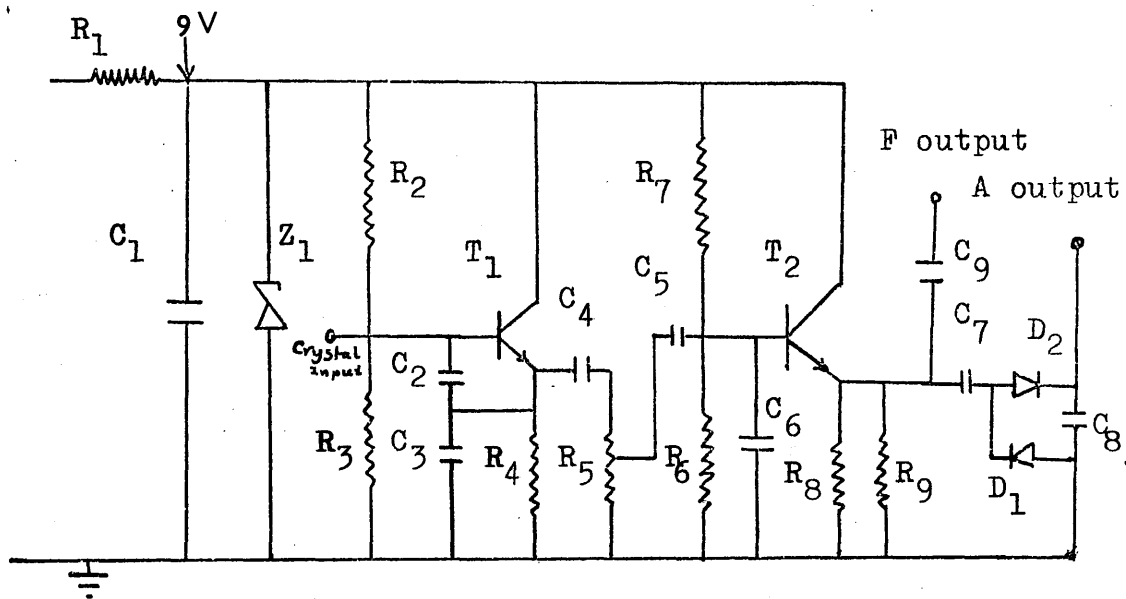
Figure (2.4)   Electronic circuit diagram for the crystal oscillator

Components:

R_1	=	100 Ohm	R_5	=	22 k-ohm
R_2, R_3	=	10 k.ohm	C_5, C_6	=	BC108
Z_1	=	BZY 85C12	R_8, R_9	=	4.7 k-ohm
C_2	=	1200 pF	D_1, D_2	=	OA90
C_3	=	82 pF	C_7	=	10pF
T_1	=	BC108	C_8, C_9	=	0.01μF
C_4	=	270pF			
R_4	=	1k-ohm			

2.4 Determination of Composition

The composition of the alloy samples prepared by simultaneous evaporation of the two elements was determined from the relative rates of the deposition of these materials onto two quartz crystal monitors. These rates, frequency shifts per unit time, were recorded by a "Twin source control system" specifically designed for the purpose of this work (MacLeod and Long (to be published)). The actual rate of deposition onto the substrate was determined by mounting a substrate crystal (Sutton (1975)) in place of the optical sample. The frequency shifts of the substrate crystal and the crystal monitors were related to each other by a geometric factor k_m,

$$df_s = k_m df_m \qquad (2.4.1)$$

or

$$df_s/dt = k_m(df_m/dt) \qquad (2.4.2)$$

k_m was determined experimentally for each source position.

Using $df = -^Cfo/A \quad .dM$

and $df_s = k_m df_m$

we may obtain

$$dM = -Ak_m df_m/C_{fo} \qquad (2.4.3)$$

we know that the number N of atoms in mass dM of any element is

$$N = N_o \, dM/W \qquad (2.4.4)$$

where N_o is Avogradro's number and W is the atomic

weight of that element. Hence, when masses dM_{Mg} and dM_{Bi} of magnesium and bismuth respectively were deposited simultaneously onto the substrate to form any alloy, the ratio of magnesium atoms to bismuth atoms was given by

$$r = \left(\frac{N_o}{W_{Mg}} \cdot dM_{Mg}\right) / \left(\frac{N_o}{W_{Bi}} \cdot dM_{Bi}\right)$$

$$= \frac{W_{Bi}}{W_{Mg}} \cdot \frac{dM_{Mg}}{dM_{Bi}} \qquad (2.4.5)$$

Using equation (2.4.3) we get

$$r = \frac{W_{Bi}}{W_{Mg}} \cdot \frac{-Ak_{Mg} \cdot df_{Mg}/^C f_{Mg}}{-Ak_{Bi} \cdot df_{Bi}/^C f_{Bi}}$$

Re arranging

$$r = \frac{W_{Bi}}{W_{Mg}} \cdot \frac{k_{Mg}}{k_{Bi}} \cdot \frac{f_{Bi}^2}{f_{Mg}^2} \cdot \frac{df_{Mg}}{df_{Bi}} \qquad (2.4.6)$$

where $df \ll f$

The ratio of atoms r could also be found from the ratio of rates of changes of monitor crystal frequencies since

$$\frac{df_{Mg}}{df_{Bi}} = \frac{df_{Mg}}{dt} / \frac{df_{Bi}}{dt} \qquad (2.4.7)$$

Hence

$$r = \frac{W_{Bi}}{W_{Mg}} \cdot \frac{k_{Mg}}{k_{Bi}} \left\langle \frac{df_{Mg}}{dt} / \frac{df_{Bi}}{dt} \right\rangle \frac{f_{Bi}^2}{f_{Mg}^2} \qquad (2.4.8)$$

One bismuth atom to every $r \times$ magnesium atoms corresponds to an atomic concentration X of bismuth, given by

$$X = 100 / (1 + r) \text{ at.\% Bi} \qquad (2.4.9)$$

Equations (2.4.8) and (2.4.9) allowed the composition of each layer being deposited as a function of time to be determined. This gave us information about the homogeniety of the deposited films. Equations (2.4.6) and (2.4.9) could be used to determine the overall composition, interpreting df_{Mg} and df_{Bi} as the total frequency shifts.

2.5 Temperature Measurement
2.5.1 Introduction

An accurately determined temperature is required for the measurement of electrical and optical properties of an alloy sample as a function of temperature. It is important to measure the actual temperature at the surface of the substrate. A thin film thermocouple deposited on the surface of the substrate may be used to measure the actual surface temperature (Herrell (1969)) . The disadvantage of this method is that thin film thermocouples lack reproducibility from one sample to another unless extreme precautions are taken in their preparation. Calibration is generally required for each thermocouple. Another method of ensuring that the actual surface temperature of a substrate is measured by the use of thermocouple in the conventional form, when the sensing junction is clamped to the surface of the substrate and the other junction is kept at constant temperature, (e.g. in crushed ice at 0°C), a small variation in the temperature of the sensor may be determined from the e.m.f. produced by the thermocouple. This method is capable of measuring a small change of temperature ~1°C.

Resistance thermometers may also be used to determine the temperature of the substrate and the surroundings. Dauphinee and Preston-Thomas (1954) reported that fine commercial copper wire, attached with Formel varnish to a copper base, has sufficiently stable and reproducible resistance temperature characteristics to be used as a resistance thermometer in the temperature range 20 - 320°K. For our work on Mg-Bi alloy films prepared at near liquid nitrogen temperature and annealed to room temperature, thermocouples of copper and Eureka wires, and a copper resistance thermometer were used to determine the temperature of the substrate surface and the surroundings.

2.5.2   Thermocouple Calibration:

The wire materials used for the thermocouple were 44 S.W.G. copper and 38 S.W.G. Eureka.   It was found that different batches of the same couple wire gave slightly different readings when referenced to identical temperature baths.   For this reason the actual thermocouples used in the vacuum chamber were calibrated.   The reference baths used were crushed ice, liquid nitrogen and boiling water. One junction was placed in the crushed ice as constant reference whilst the other end (sensor) was placed in liquid nitrogen and boiling water.   The e.m.f's produced in the thermocouple due to these temperature references were

-5.554 ∓ 0.002 mV between 0°C and -196°C

4.300 ∓ 0.002 mV between 0°C and 100°C

-9.840 ∓ 0.002 mV between -196°C and 100°C

The above calibration was used to check the temperatures determined by the copper resistance thermometer.

2.5.3 Copper Resistance Thermometer:

A fine varnished copper wire (44 S.W.G) was wound γ.ound a copper base, varnish was used to attach copper windings together. This was clamped tightly to the main base copper plate of the sample holder. In this way a small variation of the copper base plate temperature resulted in a change of the copper windings resistance. A constant current was passed through t he windings, and the voltage between its terminals was measured employing the standard 4-point probe. The circuit used to supply the constant current is shown in figure (2.5). The current was monitored across a standard 1 kilo-ohm resistance to monitor any change in its amount. A Keithley digital voltmeter capable of resolving 0.01 mV was used for this purpose. Prior to installation of the thermometer, it was calibrated using iced water and liquid nitrogen baths. A current of 1.0215 milli-amp. was passed through the wire while it was immersed in the two reference baths. The resistances were then determined at these two reference temperatures and fitted to form

$$R = R_o + a \rho (T) \qquad (2.5.10)$$

where $\rho(T)$ given by (Dauphinee and Preston-Thomas (1954)) , enabling R_o and a to be determined.

on/off

18v

Z_1 T_2

R_3

T_1

R_1 R_2

Z_2

Z_3

R_4

8 way
R/S Socket

Radial Socket
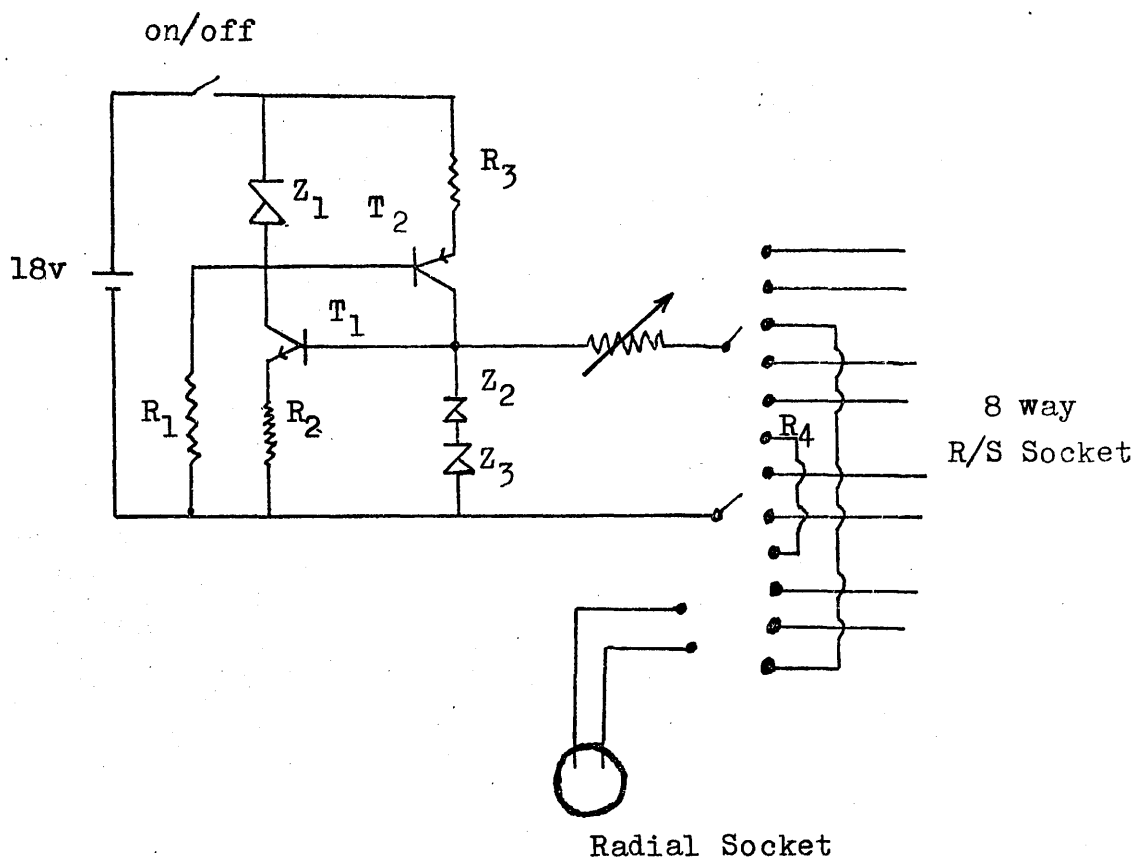
Figure (2.5) Electronic circuit diagram for constant
current supply

Components:

Z_1 = 4.7 volts

Z_2, Z_3 = 5.6 volts

R_1 = 100 k-ohm

R_2 = 2 k-ohm

R_3 = 1 k-ohm

T_1 = 2N1306

T_2 = 2N1307

R_4 = 1 k-ohm

CHAPTER 3

EQUIPMENT

In this chapter we describe the equipment designed
and used to carry out the measurements described in this
dissertation.   It was decided to prepare the amorphous
Mg-Bi alloy films by vapour quenching of the two consti-
tuents from two independent sources (co-evaporation tech-
nique), see section 2.2, onto substrates kept near liquid
nitrogen temperature, $77^{\circ}K$.   The equipment allowed us to
carry out the electrical and the optical measurements
in situ.

3.1   Vacuum System

A conventional oil vapour diffusion pump (E04)
supplied from Edwards Vacuum Components Limited, was used
to evacuate the vacuum chamber.   The ultimate vacuum is
quoted as 10^{-7} torr.   Typical base pressure of $2 - 4 \times 10^{-7}$
torr was achieved when the diffusion pump trap, Meissner
trap and the sample holder reservoir were filled with
liquid nitrogen.

The vacuum chamber was constructed in two sections.
First, the lower section (plate 1) was a 12 inch stain-
less steel ring mounted on a stainless base plate.   This
section contained the two evaporation sources, and the two
crystal holders.   The magnesium and bismuth sources were
attached between two of the feed throughs and a central
bar, on which was clamped a shield to restrict the region

of evaporation of each source, and prevent undersirable
cross evaporation of magnesium on the bismuth crystal and
vice versa.   The two crystal holders were mounted directly
above the two sources in such a way that each crystal
monitor saw only one source.   A 35 mm spacing between the
two crystal holders allowed for evaporants to pass through
to the substrates.   This geometry, figure (3.1), allowed
for the substrates to see a well defined cross section of
the evaporants of both elements through the spacing.

The top section of the vacuum system was a stainless
steel cylinder containing two windows (sapphire windows)
used for optical transmittance measurements.   The two
windows were at the same height as the source beam and
the optical sample, and were protected from the evaporant
streams by sylindrical shields.   Magnesium particularly
causes contamination of the windows unless they are care-
fully shielded, because it sublimes at low temperatures.
A top plate (plated steel) was used to close the vacuum
chamber with a portal in it allowing for the sample holder
(including the liquid nitrogen reservoir) to be placed
above the sources.   A cylindrical copper plate with a
copper tube soldered to it (Meissner trap) was attached
to the top plate.   The liquid nitrogen was passed through
the copper tube which improved the vacuum inside the
vacuum chamber.   The top section could be shifted to
allow for the optical alignment, cleaning the lower
section of the vacuum chamber and preparation for the
next evaporation runs.

Plate(1)

3.2   The Sample Holder and Liquid Nitrogen Reservoir

The sample holder was designed to allow for the preparation of the amorphous alloy samples on two liquid nitrogen cooled substrates, and for optical and electrical measurements to be carried out in situ.   One substrate was used to prepare films for the optical measurements while the other substrate was used for the electrical measurements.   The holder assembly attached to a liquid nitrogen reservoir is shown in plate (2).

The sample for resistance measurements was screwed to a copper block which was itself attached in the main baseplate of the sample holder.   The electrical connections for the electrical sample are described in section (4.6) The sample substrate used for the optical measurements was placed on a rotatable copper mask, and cooled using flexible copper braid screwed to the main copper base plate.   Both electrical and optical substrates were coplanar during the preparation of the alloy films.   The optical sample was rotated 90° to allow for the trans-mittance measurement to be carried out.   The rotatable mask was clamped to a stainless steel bridge attached to the main base plate.   A sample shutter was also screwed to the main base plate.   Both the sample mask and the shutter were operated by two gear wheel shafts passed through the sample holder top plate.   A copper resistance thermometer was clamped to the main plate.

A stainless steel cylinder with a copper disc base was used as a liquidnitrogen reservoir.   The capacity of this reservoir was sufficient to keep the sample holder,

Plate (2)
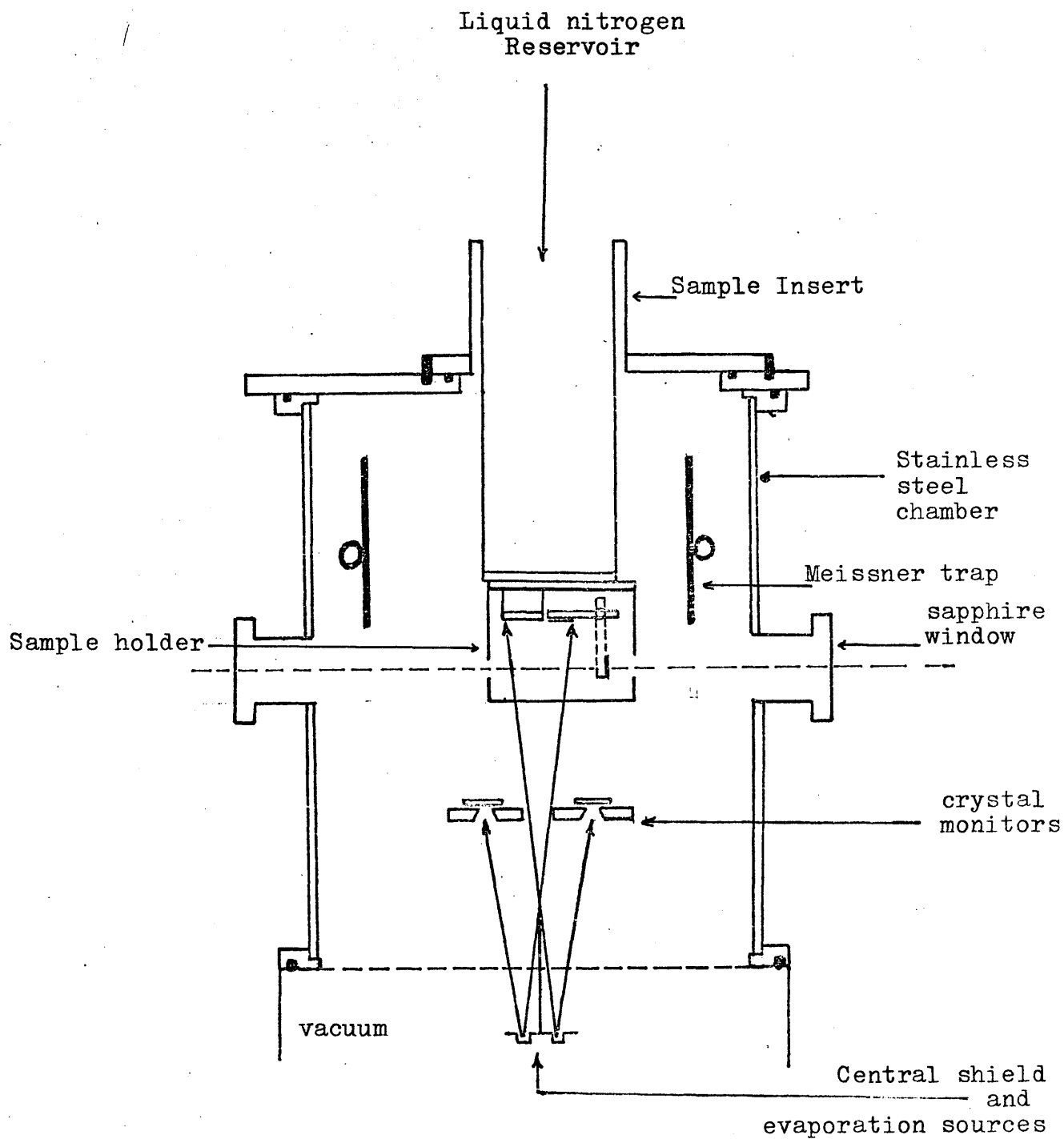
Figure (3.1)   Vertical section of the vacuum system (in
the plane of the light beam) and the evaporation
geometry.

hence the substrate, at near liquid nitrogen temperature for four hours. The reservoir was normally kept full of liquid nitrogen during the alloy preparation and the optical measurement. An automatic timed control system was used to fill the reservoir with liquid nitrogen, every three hours, overnight.

3.3   Optical System and Geometry of the Optical Bench

The optical system used to measure the normal incidence transmittance   consisted of the single beam monochrommater, the optical bench, light chopper and the infra-red detector. The light signal was measured using a phase sensitive detector and a digital (Keithly) voltmeter connected to the output socket of the phase sensitive detector.

3.3.1 Optics Geometry

The optical configuration used to measure the transmitted intensities of the reference and the attenuated signals was Source-Sample-Monochromater-Detector, figure (3.2). Plate (3) also shows a general view of the optical bench and the vacuum system. The mirrors were all either plane or spherical with reflecting surface of vacuum deposited aluminium. The beam from the light source was focussed at the sample by mirrors M1 and M2. The radiation transmitted through the sample was collected by M3 and reflected from M4 to M5 which, with mirror M6, focussed it at the entrance slit S1 of the monchromater. A beam displacer operating like a rotating periscope was placed in front of the sapph ire window (in the stainless steel vacuum
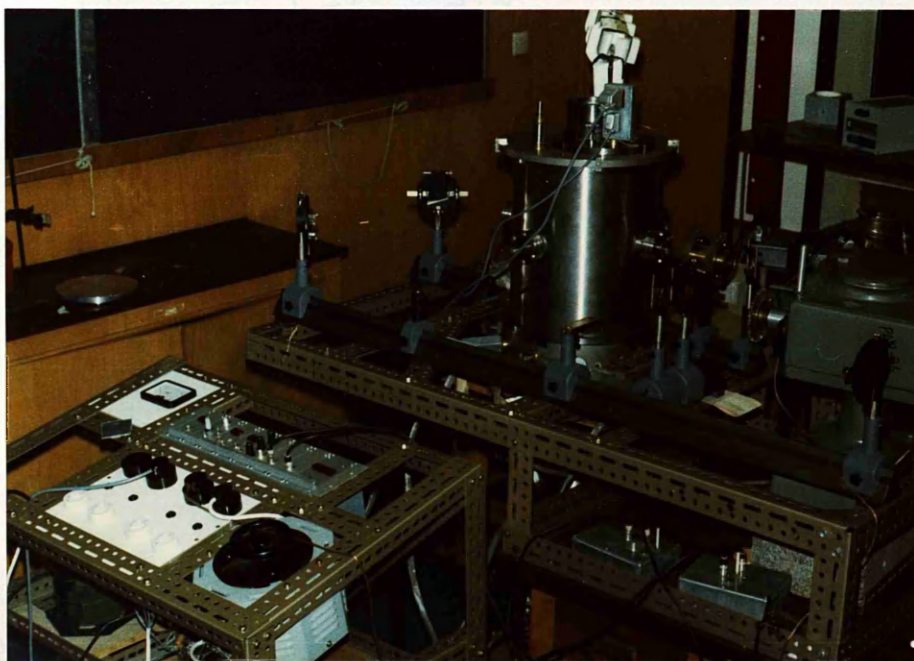
Plate(3)
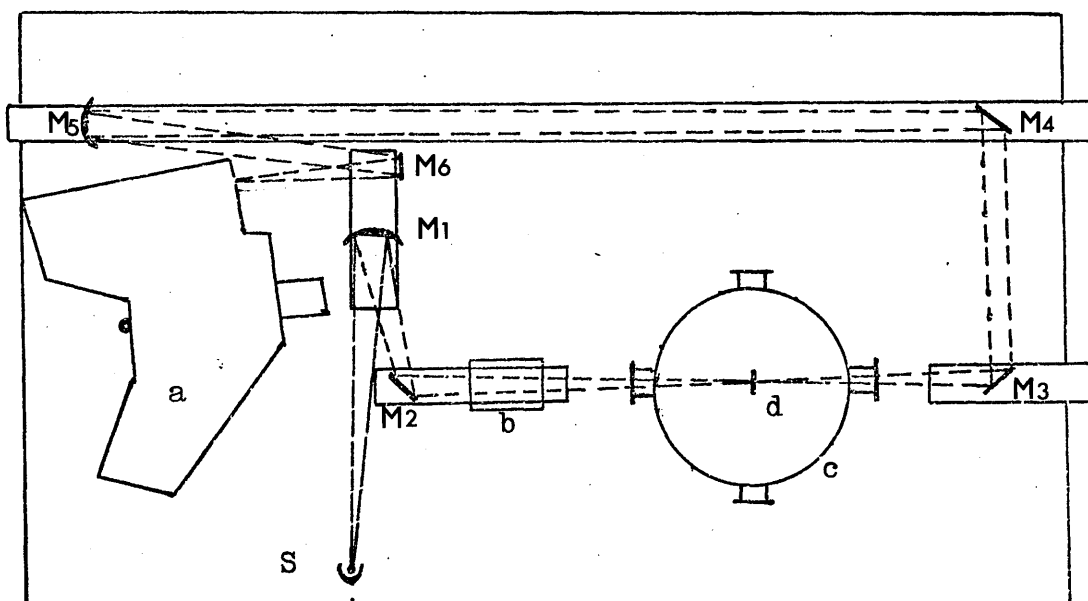
Figure (3.2) The optical system for transmittance

measurements

(a) Spectrometer

(b) Beam displacer

(c) Vacuum chamber

(d) Sample

(S) Light source

chamber) allowed to measure the transmittance at four position on the two film thickness, see section (5.5)

3.3.2   The Single Beam Spectrometer

The single beam spectrometer used (Hilger and Watts D600) was a form of the Wadsworth mirror-prism configuration.   The spectrometer was supplied with a direct wavelength read-out (wavelength range 0.2 μm to 3.5 μm). The read-out was further checked using emission lines of known wavelengths in the spectra of sodium, mercury and helium.   In Table (3.1) we have tabulated the lines used and their wavelengths, and the read-out of spectrometer drum.   The resolution of the spectrometer was determined from the inverse dispersion curve, figure (3.3) of the crystalline quartz prism (the dispersive element used in the spectrometer), and the width of the entrace and exit slits which were generally kept at 0.3 mm.   The resolutions, at any particular wavelength in the range 0.5 - 2.8 μm, are tabulated in Table (3.2).   Thes results show that the spectrometer had a satisfactory resolution as $\dfrac{\Delta \lambda}{\lambda}$ was small.

3.4   Signal Measurement

3.4.1   Radiation Source

The radiation source chosen was a 100 watt quartz halogen lamp with tungsten filament transmitting light up to 3 μm.   The lamp was contained in a water-cooled copper holder, figure (3.4).   The power was supplied to the lamp by a stabilised D.C. Power supply (to eliminate any 100 Hz

Drum read out $\mp 1 \%$	Wavelength (μm)	Source
0.5	0.4983	Na
0.57	0.5688	Na
0.59	0.5985	Na
0.62	0.6160	Na
0.71	0.7065	He
1.08	1.083	He
2.07	2.0583	He

Table 3.1

Some of the wavelength calibration points.

Reference used for the wavelengths in Column 2 was "The International Critical Tables". National Research Council, Edited by E.W. Washburn, McGraw-Hill, New York, (1926).
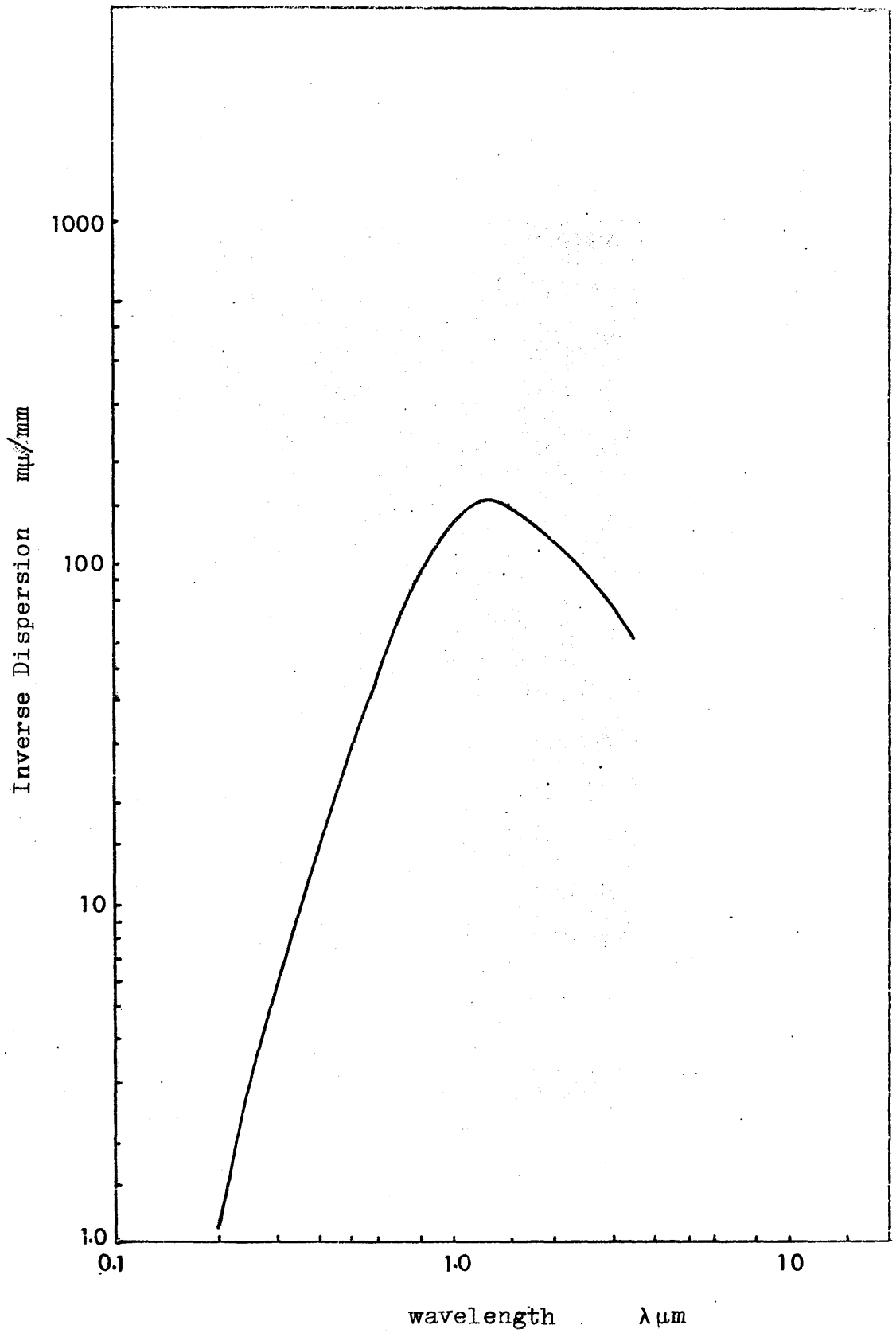
Figure (3.3)   Inverse dispersion curve of the crystalline
quartz prism (Hilger and Watts Ltd. manual)

Wavelength μm	$\Delta\lambda$ (Å)	$\Delta\lambda/\lambda$
0.8	95	0.0118
0.9	115	0.0127
1.0	130	0.013
1.1	140	0.0127
1.2	148	0.0123
1.3	150	0.0115
1.4	148	0.0106
1.5	145	0.0097
1.6	140	0.0088
1.7	135	0.0079
1.8	130	0.0072
1.9	120	0.0063
2.0	115	0.0058
2.1	110	0.0052
2.2	105	0.0048
2.3	102	0.0044
2.4	98	0.0041
2.5	92	0.0037
2.6	87	0.0033
2.7	85	0.0031
2.8	80	0.0029

Table 3.2   Resolution of spectrometer.

$\Delta\lambda$. the spectral slit width.
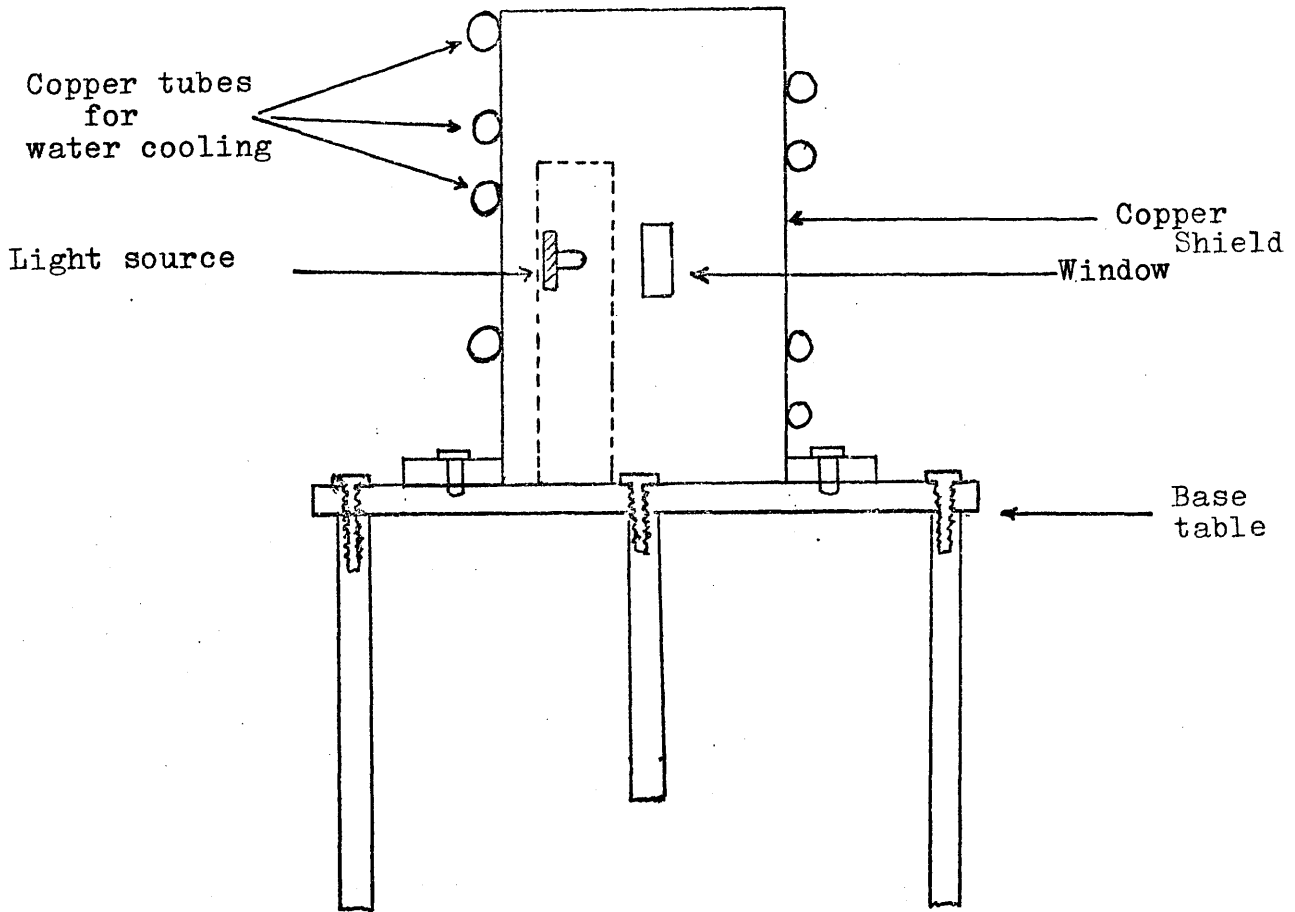
Figure (3.4)   Water-cooled holder for the light source
(100 watt) quartz halogen lamp

component in the output).   The stability of the source
output signal was tested, a drift of typically less than
5 per cent was observed over a period of 10 hours.

A set of I_o and I_t (the reference and transmitted
intensities respectively) measurements was completed in
less than 30 minutes, or alternatively point to point
comparison procedure was carried out.   In this way we
avoided any significant error in the estimated trans-
mittance due to drift in the source signal.

The light focussed (reference and transmitted signals)
at the entrance slit of the spectrometer was chopped at a
fixed standard 110 Hz $\mp$ 2%.   The reference output of the
light chopper (supplied by Edinburgh Intruments Limited),
used to trigger the reference channel of the phase sensitive
detector, was a 2V r.m.s. sinewave.

3.4.2   Signal Detection

An indium-antimonide photoconductive infra-red
detector (supplied by Mullard) operated at liquid nitrogen
temperature (77^oK) was used to detect the radiation at the
exit slit of the spectrometer.   The area of the sensitive
element of the detector was 4 x 4 mm.   The output signal
from the infra-red detector was amplified using a lock-in
amplifier (Brookdeal 9501).   A digital Keithly voltmeter
(giving a resolution of one part in 2000) was used to
display the signal.

C H A P T E R   4

BASIC PROPERTIES AND ELECTRICAL MEASUREMENTS

Introduction

This chapter is divided into two parts.   First we describe procedure during alloy preparation.   The composition analysis of sample 7 is given in detail to illustrate the method used to evaluate the composition of the alloy films.   Also the methods used to determine the thicknesses and the densities of the coevaporated films are described. The second part of this chapter is devoted to the electrical measurements.

4.1   Procedure during Alloy Preparation

It was decided to prepare two alloy samples for the electrical and the optical measurements.   The sample geometry used for the electrical sample measurements is described later in section (4.6).   The optical sample prepared in the form of two films with different thicknesses but with the same composition.   Prior to films preparation the vacuum system was cleaned and any previous alloy was removed.   The alignment of the optics was carried out with the sample holder in position.   A calibration of the two crystal monitors was carried out in order to determine the geometrical factors k_{Mg} and k_{Bi}. These factors were used to determine the actual rates of

deposition on the optical sample. Magnesium and bismuth were deposited onto a cooled crystal substrate and $_{Mg}$ and $_{Bi}$ were evaluated using equation (2.4.3) After the above steps had been completed the two substrates were transferred to their positions on the sample holders. The electrical leads for the d.c. resistance measurements were connected. The oil diffusion pump was left overnight to evacuate the vacuum chamber. The Meissner trap, the liquid nitrogen reservoir (sample holder) and the pump trap were topped up with liquid nitrogen. At this point the pressure inside the vacuum chamber was typically $2 - 4 \times 10^{-7}$ torr, and the temperatures of the substrates and the surroundings were near liquid nitrogen temperature. The rate monitor crystals were checked and the frequencies recorded. The rate monitor scales were set and the evaporation rate outputs zeroed.

The system was now ready for the alloy to be deposited. The currents passing through the two evaporation sources were gradually increased. The magnesium and bismuth deposition rates were monitored on the twin source control system until the desired rates were reached. The main shutter was then opened and the rates of deposition of the two elements were stored in the memory of the twin source control system. The electrical substrate and half of the optical substrate were exposed to the components, the optical substrate shutter was opened after a certain length of time in order to deposit the thin films of the optical sample. The duration of the alloy deposition varied from one sample to another. Small adjustments were made if the

rates of evaporation deviated from the desired rates.
The resistance of the deposited alloys were measured
immediately after the deposition had been completed.
The compositions of the alloy films were calculated
using equations (2.4.8) and (2.411).   The compositional
 analysis of one of the samples is described in detail
in the next section.

4.2   Composition of Alloy Films

The atomic composition of the amorphous alloy films,
prepared by the coevaporation method described in the last
section, was evaluated from the rates of deposition of the
two elements.   These rates were recorded as a function of
time (df_{Mg}/dt and df_{Bi}/dt) during the alloy deposition.
This gave us information about the composition as a function
of depth.   The total frequency shifts (df_{Mg} and df_{Bi})
of the two crystal monitors were also used to determine the
overall atomic composition.   The composition analysis of
sample 7 is given here to illustrate the method used to
evaluate the composition of the alloy films.   The geome-
trical factors K_{Mg} and K_{Bi} determined from equation (2.4.3)
were 0.453 $\mp$ 0.001 and 0.495 $\mp$ 0.003 respectively.   The
magnesium rate monitor was multiplied by a calibration
factor M = 5.26.   This multiplication factor was estimated
from

$$\frac{W_{Bi} \text{ X C}}{W_{Mg}(1-C)} \text{ X } \frac{K_{Mg}}{K_{Bi}}$$

where C is the atomic concentration of bismuth.   For

sample 7 the atomic concentration desired was C = 0.4.
Equations (2.4.8) and (2.4.11) were then used to evaluate
the ratio (r) of magnesium to bismuth atoms and the percen-
tage (X) of bismuth in the alloy deposited onto the substrate.
The duration of the alloy deposition of this sample was 115
seconds.   The rates of deposition of the two elements, the
ratio (r) and the atomic composition as a function of
depth are tabulated below (Table 1).   Also the overall
composition calculated from the total frequency changes
is given.   The compositions of other films are summarized
in Table 2.

Table 1

Time sec	Deposition Rates (Hz/Sec)		r = 8.6 $\dfrac{f^2_{Bi}}{f^2_{Mg}} \dfrac{df_{Mg}/dt}{df_{Bi}/dt}$	Composition X at.% Bi
	Mg	Bi		
5	8.44	48.81	1.49	40.2
10	8.53	53.36	1.38	42.1
15	8.63	50.69	1.46	40.6
20	8.56	42.67	1.73	36.7
25	8.73	46.13	1.63	38.1
30	8.73	52.07	1.44	41.0
35	9.45	55.14	1.47	40.4
40	8.63	55.74	1.33	42.9
45	8.65	53.76	1.38	42.0
50	8.63	52.17	1.42	41.3
55	8.73	49.70	1.51	39.8
60	9.37	48.71	1.65	37.7
65	8.54	50.39	1.46	40.7
70	8.53	55.84	1.31	43.2
75	8.65	56.93	1.31	43.3
80	8.54	51.4	1.33	42.9
85	8.73	40.79	1.84	35.2
90	8.63	41.18	1.80	35.7
95	8.73	45.24	1.66	37.6
100	8.73	49.20	1.53	39.6
105	8.73	53.26	1.41	41.5
110	8.73	54.95	1.37	42.3
115	8.73	55.54	1.35	42.5

Mean composition of the thin film was calculated from

the last 12 values of X.   This because the duration

of deposition of that film was 60 seconds.

Mean composition as a function of depth of the thick film

$= 40.3 \mp 1.6$ at.% Bi

Mean composition as a function of depth of the thin film

$= 40.4 \mp 2.6$ at.% Bi

The overall composition calculated from the total frequency changes of the two crystals (df_{Mg} and df_{Bi})

1. The thick film $= 40.4 \mp 1.2$ at.% Bi

2. The thin films $= 40.5 \mp 1.2$ at.% Bi

Table 2

Sample	Composition of the thick film at.% Bi	Composition of the thin film at.% Bi
14	36.1 ∓ 1	
7	40.3 ∓ 1.6	40.4 ∓ 2.6
11	41.1 ∓ 2.5	41.2 ∓ 2.3
5	41.1 ∓ 3.2	
6	42.4 ∓ 1.1	41.9 ∓ 1.3
3	45.8 ∓ 4	
4	45.9 ∓ 1.1	
15	48.4 ∓ 3.5	47.0 ∓ 1.3

Table 2:   Compositions of the amorphous alloys studied. Samples 3, 4 and 5 were prepared as single films. Samples 1, 2, 8, 9, 10, 13 were not fully studied because of large fluctuations in the rates of deposition.

4.3. Thickness Measurements

The thickness of the film is an important factor in the determination of the optical constants n and k (the real and imaginary parts of the complex refractive index respectively). The thicknesses were initially measured to an accuracy of 5 - 10% with a Varian A^O scope. The Varian A^O scope required a high reflectivity surface. The alloy films were overcoated with an aluminium reflecting surface in a separate vacuum system. The accuracy of the measured thicknesses depended on the quality of fringes to a great extent. The error in the measured thickness represented a large fractional error for the films used in the optical measurements. Therefore it was decided to take advantage of the accuracy with which the crystal rate monitor measured deposited mass in order to determine more accurate thicknesses.

In section (2.3.1) it was shown that the mass dM deposited on area A of the substrate, corresponding to a change df in the frequency of one monitor crystal, is given by the equation

$$dM \; / \; A \; = \; -(1/^C fo \;) \quad . \; df \qquad (4.3.1)$$

The number N_i of atoms in mass dM of any element is given by the relation

$$N_i \; = \; N_o \cdot dM_i \; / \; W_i \qquad (4.3.2)$$

where N_o is Avogradro's number and W_i is the atomic weight of that element. The atomic volume is

$$V_i \; = \; W_i \; /N_o \; \rho_i \qquad (4.3.3)$$

where ρ_i is the density in gm.cm^{-3} of that element the total volume of the alloy film is

$$V = V_{Mg} + V_{Bi}$$

or

$$V = (M_{Mg} / \rho_{Mg}) + (M_{Bi} / \rho_{Bi}) \qquad (4.3.4)$$

writing $V = Ad$ we obtain

$$d_{alloy} = 1/A \left\{ (M_{Mg} / \rho_{Mg}) + (M_{Bi} / \rho_{Bi}) \right\} \qquad (4.3.5)$$

where d is the thickness.

Equation (4.3.5) may also be obtained by adding the "thicknesses" of the two elements,

$$d_{Mg} = (M_{Mg}/A\rho_{Mg}) \quad \text{and} \quad d_{Bi} = (M_{Bi}/A\rho_{Bi})$$

or

$$d_{alloy} = d_{Mg} + d_{Bi} = 1/A \left\{ (M_{Mg}/\rho_{Mg}) + (M_{Bi}/\rho_{Bi}) \right\} \qquad (4.3.6)$$

Now, using equation (4.3.1), equation (4.3.6) can be written as

$$d_{alloy} = (1/\rho_{Mg}c_{fo}) \cdot df_{Mg} + (1/\rho_{Bi}c_{fo}) \cdot df_{Bi} \qquad (4.3.7)$$

Equation (4.3.7) was used to calculate the thickness of the Mg-Bi alloy films. The thicknesses evaluated using equation (4.3.7) and those measured with the Varian A$^\circ$ scope are given in table (3). A study of the effect of thickness variation on the optical results is made in Chapter 5.

Table 3

| | Calculated thickness (A^o) | | Measured thickness (A^o) | |
Sample	Thick ∓ 1%	Thin	Thick	Thin
3	1057		1146 ∓25	
4	1140		1250 ∓69	
5	1765		1984 ∓24	
6	1799	935	1840 ∓30	1030 ∓20
7	1378	717	1693 ∓35	899 ∓ 14
11	1591	945	1893 ∓29	1072 ∓10
14	848	351	1110 ∓18	464 ∓ 7
15			1363 ∓38	625 ∓20

Table 3. Calculated thickness of the alloy films using equation (5.3.7) and the measured thickness using a Varian A^o scope.

4.4 Density of Coevaporated Films

The method used to evaluate the densities of the coevaporated films is outlined. It was expected that the density of the alloy would be different from the densities of the two constituents. The density of the alloy is given by

$$\rho_{alloy} = (M_{Mg} + M_{Bi}) / A \cdot d_{alloy} \qquad (4.4.1)$$

From equations (4.3.6) we may obtain

$$\rho_{alloy} = (M_{Mg} + M_{Bi}) / (M_{Mg}/\rho_{Mg} + M_{Bi}/\rho_{Bi}) \qquad (4.4.2)$$

or

$$\rho_{alloy} = \rho_{Mg} \rho_{Bi} (M_{Mg} + M_{Bi}) / (\rho_{Bi} M_{Mg} + \rho_{Mg} M_{Bi}) \quad (4.4.3)$$

using equation (4.3.1), equation (4.4.3) can be written as

$$\rho_{alloy} = \frac{\rho_{Mg} \rho_{Bi} (\dfrac{A}{C_{f_{Mg}}} df_{Mg} + \dfrac{A}{C_{f_{Bi}}} df_{Bi})}{\rho_{Bi} \cdot \dfrac{A}{C_{f_{Mg}}} df_{Mg} + \rho_{Mg} \dfrac{A}{C_{f_{Bi}}} df_{Bi}}$$

or

$$\rho_{alloy} = \frac{\rho_{Mg} \rho_{Bi} (df_{Mg} + {^C f_{Mg}}/{^C f_{Bi}} \; df_{Bi})}{\rho_{Bi} \cdot df_{Mg} + \rho_{Mg} \; {^C f_{Mg}}/{^C f_{Bi}} \; df_{Bi}} \quad (4.4.4)$$

Often ${^C f_{Mg}}/{^C f_{Bi}} \approx 1$ and rarely deviated from unity. The densities of the Mg-Bi alloys calculated over a range 10 - 90 at.% Bi are illustrated in figure (4.1). The densities of the prepared Mg-Bi alloys are also presented together with earlier data (Herrell (1969)) and (Sutton (1975)) .

4.5   Condu.ction Mechanism in Amorphous Semiconductors

Mott and Davis (1971) suggested a model for the density of states and mobility as functions of energy, figure (4.2), to demonstrate the conduction mechanism in amorphous semiconductors. In this model a fairly narrow band of localized states is assumed to exist near the centre of the gap, of sufficiently high density to effectively pin the Fermi energy over a wide temperature range. With this model, three mechanisms of electrical conduction
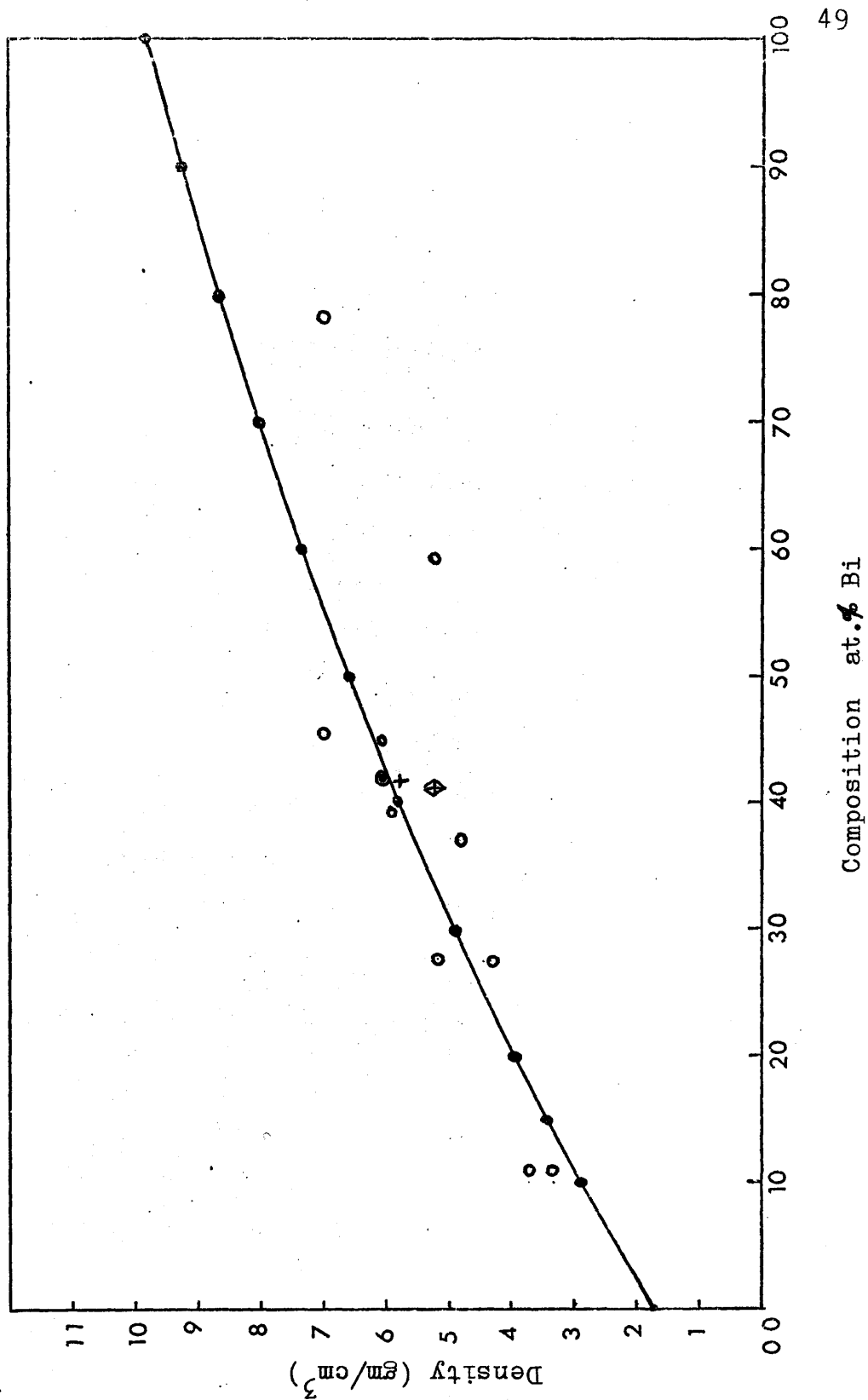
Figure (4.1) Density of coevaporated Mg-Bi Alloys

o   Herrell and Ferrier

+   Sutton

◉   Present work

can be distinguished.

1. Conduction due to carriers excited beyond the mobility edges into "non-localized" states. If the current is carried by holes, we expect the conductivity

$$\sigma = \sigma_0 \exp\left(-(E_F - E_V)/kT\right) \qquad (4.5.1)$$

where σ_0 is pre-exponential factor. E_V (eV) is the energy at the valence band mobility edge. E_F (eV) is the Fermi energy. σ_0 is expected to be approximately temperature independent. Hence, from equation (4.5.1) a plot of $\ln \sigma$ against $1/T$ will yield a straight line if $(E_F - E_V)$ is a linear function of T over the temperature range measured. If $E_F - E_V = E(o) - \gamma T$, then the slope of such a plot will be $E(o)/k$ and the intercept on the σ axis will be $\sigma_0 \exp(\gamma/k)$.

2. Conduction due to carriers excited into the localized states at the band edges E_A or E_B. If the main current is carried by holes, and conduction is by hopping, then

$$\sigma = \sigma_1 \exp\left(-(E_F - E_B + \Delta W_1)/kT\right) \qquad (4.5.2)$$

where ΔW_1 is the activation energy for hopping, and E_B is the energy at the band edge. σ_1 is expected to be about $10^2 - 10^4$ less than σ_0 due to the lower mobility and also the lower effective density of states.

3. Conduction due to carriers hopping between localised states near the Fermi energy level. The conductivity in this case may be given by

$$\sigma = \sigma_2 \exp\left(\frac{-\Delta W_2}{kT}\right) \qquad (4.5.3)$$

where ΔW_2 is the hopping energy of the order of the half the width of the narrow band at E_F, and $\sigma_2 \gg \sigma_1$. A straight line in a plot of ln σ against $1/_T$ is expected only if hopping is between nearest neighbours. At very low temperature the conductivity is expected to be of the form, (since tunnelling of carriers may be energetically favourable to more distant sites),

$$\sigma = A \exp \left(-B/_{T^{\frac{1}{4}}}\right)$$

where A is a constant dependent on the phonon frequency, and $B = 2.1 \left(\alpha^3/KN(E_F)\right)^{\frac{1}{4}}$, α is the decay parameter for localized wave functions. However, the total conductivity for all processes is obtained by integrating over all available energy states. Thus for states above E_F using Boltzman statistics

$$\sigma = e \int N(E) \, \mu(E) \, f(E) \, dE$$

where $N(E)$ is the density of states, $\mu(E)$ is the mobility and $f(E)$ is the Boltzman distribution function. Figure (4.3) illustrates the effect of temperature on the mode of conduction, and the temperature dependence of conductivity expected by using the model of figure (4.2).

4.6   Electrodes and Sample Geometry

Resistance measurements using aluminium electrodes in the early attempts to prepare amorphous Mg/Bi alloy films, showed that this material oxidized after deposition and exposure to the atmosphere, and gave non-ohmic contacts. Other workers have reported similar phenomena.   Sik (1974)
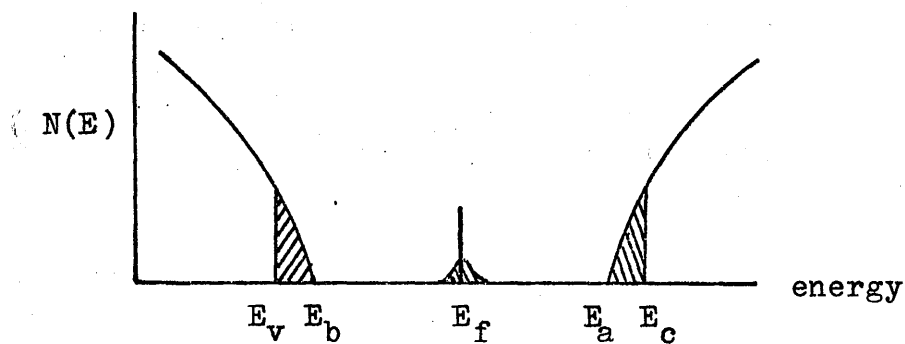
Figure (4.2) Model density of states as a function of energy
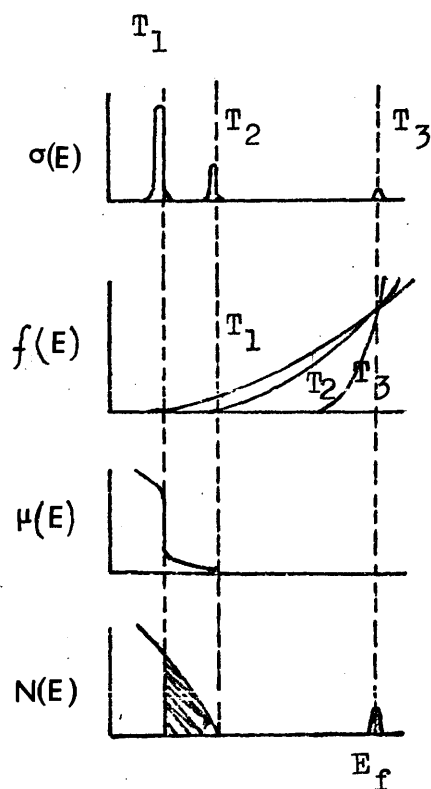(Mott and Davis (1971))

Figure (4.3) Illustration of the effect of temperature
on the mode of conduction

$$\sigma(E) = e N(E)\mu(E)f(E) \; ; \; T_1 > T_2 > T_3$$
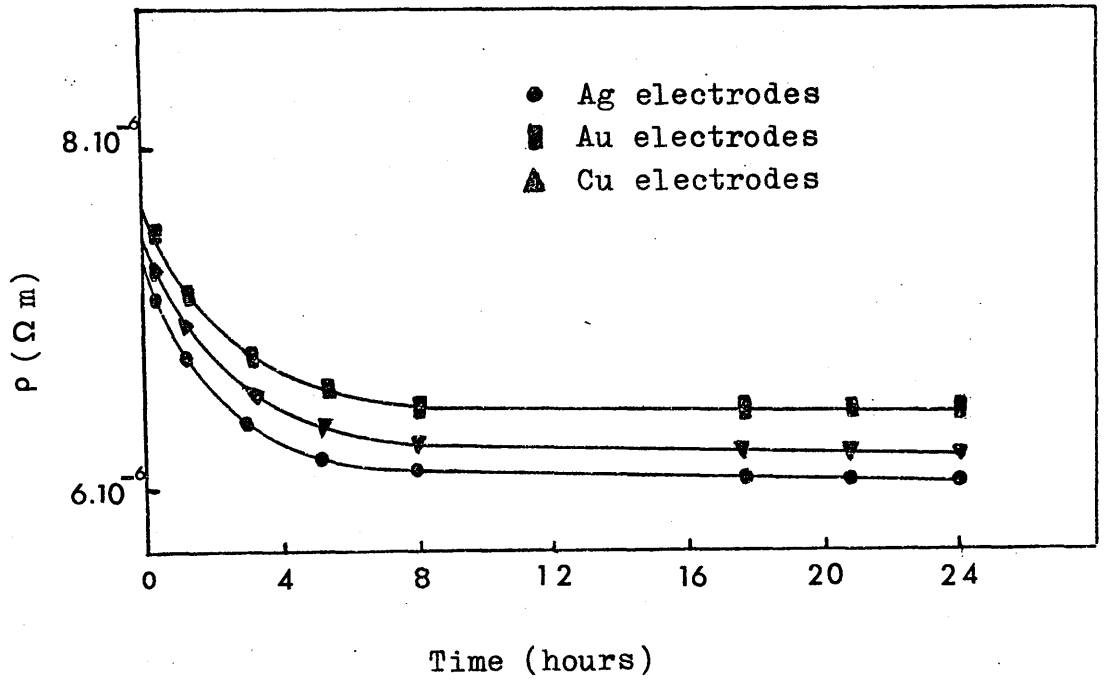
Figure (4.4)   Resistivity of three electrode
                materials as a function of time
                (Sik (1974)).

carried out tests using electrodes of various materials
(gold, silver, copper) to investigate whether the measured
conductivity of a sample was affected by the type of elec-
trodes material used, figure (4.4) Sik concluded, from
those tests, that for the materials which were investigated,
the absolute magnitude of the conductivity seemed to a good
approximation, to be independent of the electrode for the
materials and temperature range considered. Further, the
behaviour of the conductivity over a fairly long period of
time appeared to be independent of the electrodes for
these materials.

In our work on amorphous Mg-Bi alloy films, gold
electrodes were prepared in a separate vacuum system of
base pressure approximately (10^{-6} torr). The substrate
was exposed to atmosphere prior to mounting on the sample
block. The sample geometry, used for the d.c. resistivity
measurements, and the electrical connections are illustrated
in figure (4.5). The four probe technique, figure (4.6),
was used to measure the d.c. resistance of the amorphous
films though a small electrode resistance remained in
series with the sample. This technique eliminated lead
resistance. A measured current monitored across a 1 K-ohm
resistor was applied to the film, and the voltage developed
across the film was measured. The temperature was deter-
mined by means of a thermocouple strapped to the surface of
the substrate, also by means of the copper resistance ther-
mometer attached to the copper base plate. Typical resist-
ance temperature plots for two positions on the substrate
are shown in figure (4.7a,b).From these plots we may conclude

substrate and
gold electrodes

3

2

1
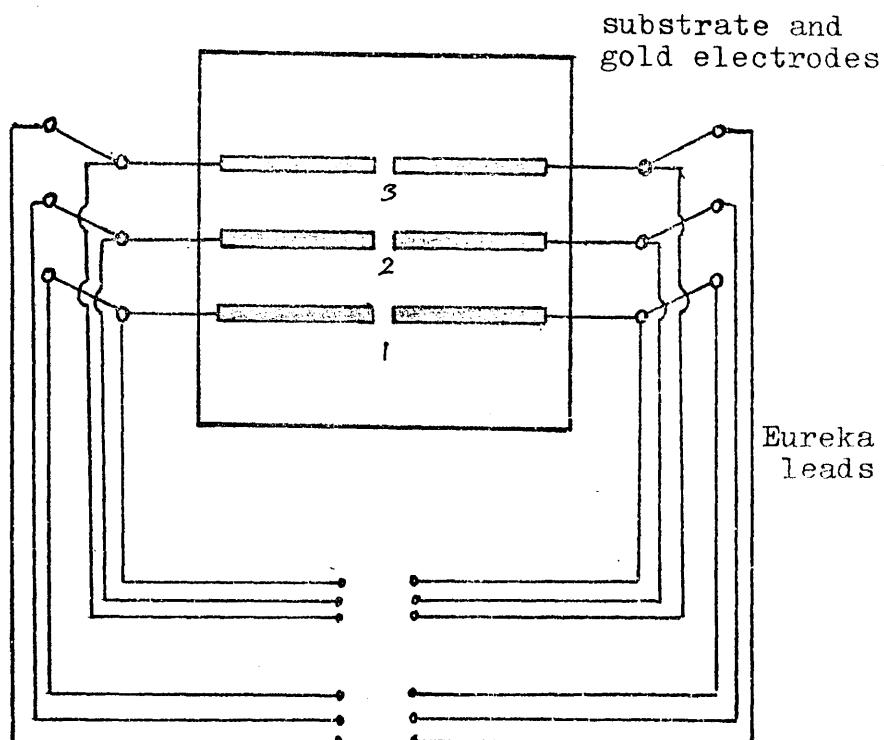
Eureka
leads

Figure (4.5)   Sample geometry used for d.c. resistivity

measurements, and electrical (Eureka leads)

connections.

R

V_f

18 v

1 k-ohm

Figure (4.6)   Four-probe circuits for alloy

films d.c. resistivity measurements.

Figure (4.7a)   Variation of d.c. resistivity as a function of
                temperature for sample 6 (42.4 ∓ 1.1 at.% Bi).
                Position 2 of figure (4.5).

Figure (4.7b) Variation of d.c. resistivity as a function of temperature for the same sample 6 (42.4 ∓ 1.1 at.% Bi) Position 1 of figure (4.5)

that variations in composition along the substrate are small.

4.7 Temperature Dependence of D.C. Conductivity

The d.c. resistivity of the amorphous Mg-Bi alloy films may be determined using the expression
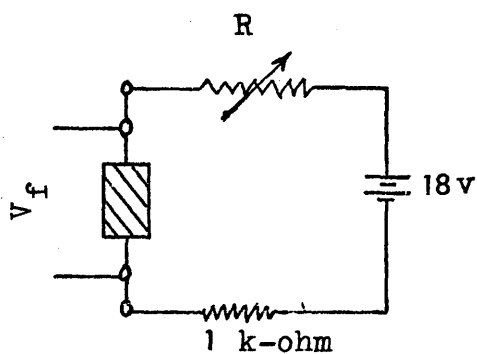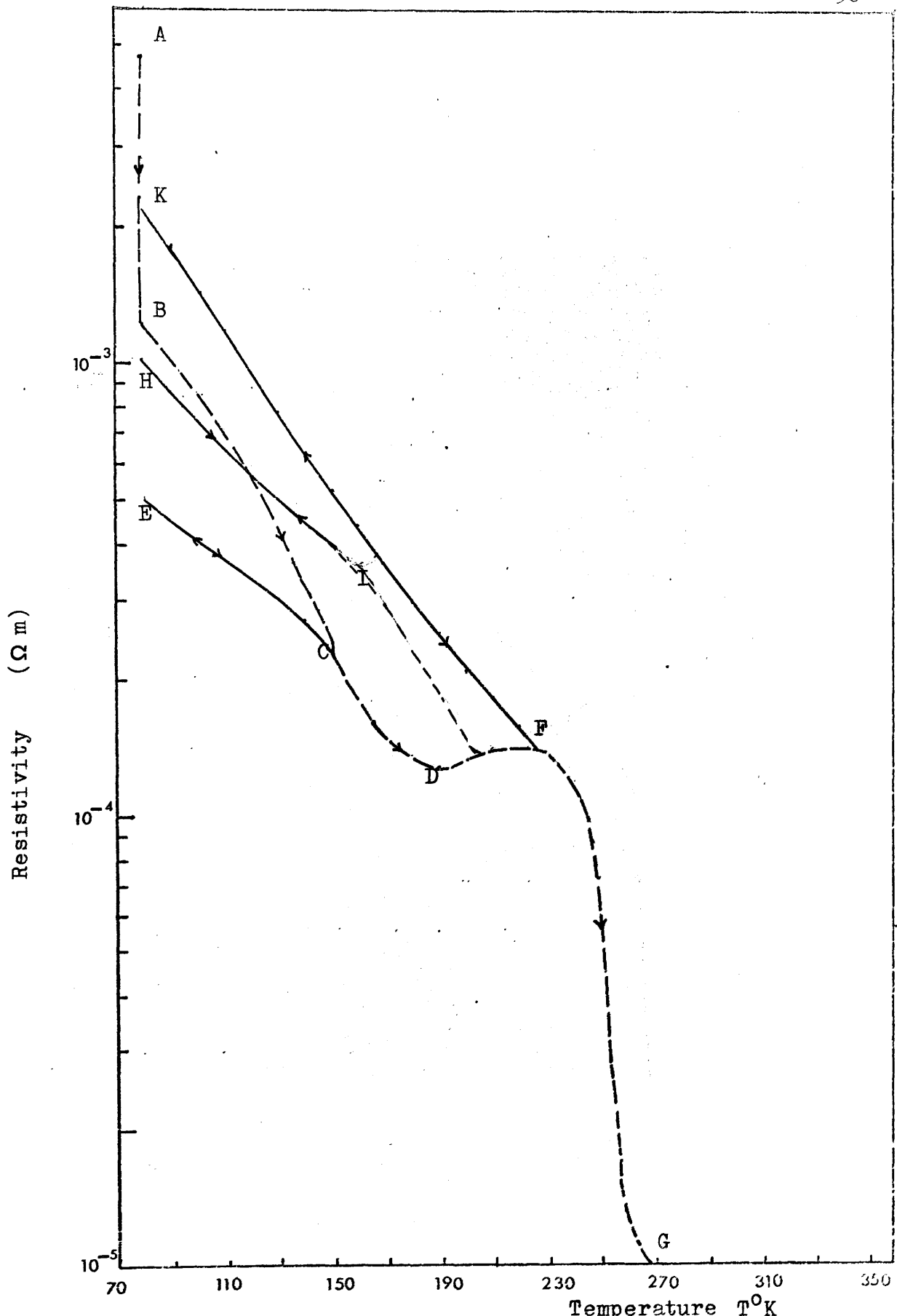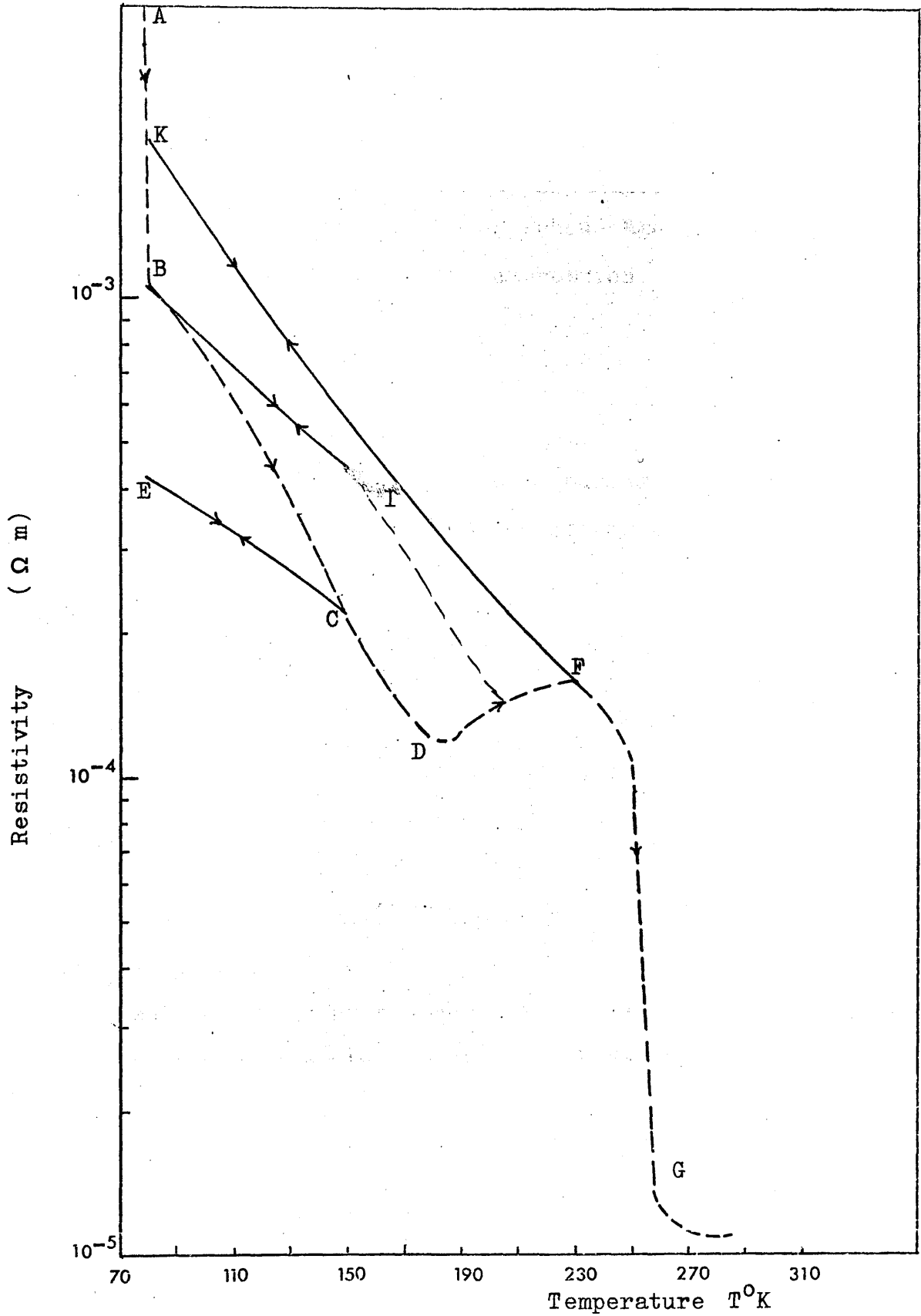
$$R = \rho \frac{L}{A}$$

where R is the resistance

L is the length between the measuring electrodes

A is the cross sectioned area of the sample between the measuring electrodes

ρ is the resistivity

The temperature dependence of the d.c. resistivity was measured for a number of the amorphous Mg-Bi alloy films near to, less than and greater than 40 at.% Bi prepared initially near to liquid nitrogen temperature. These measurements were carried out in order to invest-igate the effects when alloy films annealed to successively higher temperatures.

Typical behaviour of the resistivity as a function of temperature for a slightly bismuth rich film is illustrated in figure (4.8).   This is chosen here because it contains the general features encountered for the samples we have studied.   The resistivity immediately after deposition is represented by point A.   Irreversible changes in resist-ivity are shown hatched, whereas reversible paths are represented by solid lines.   Three distinct irreversible
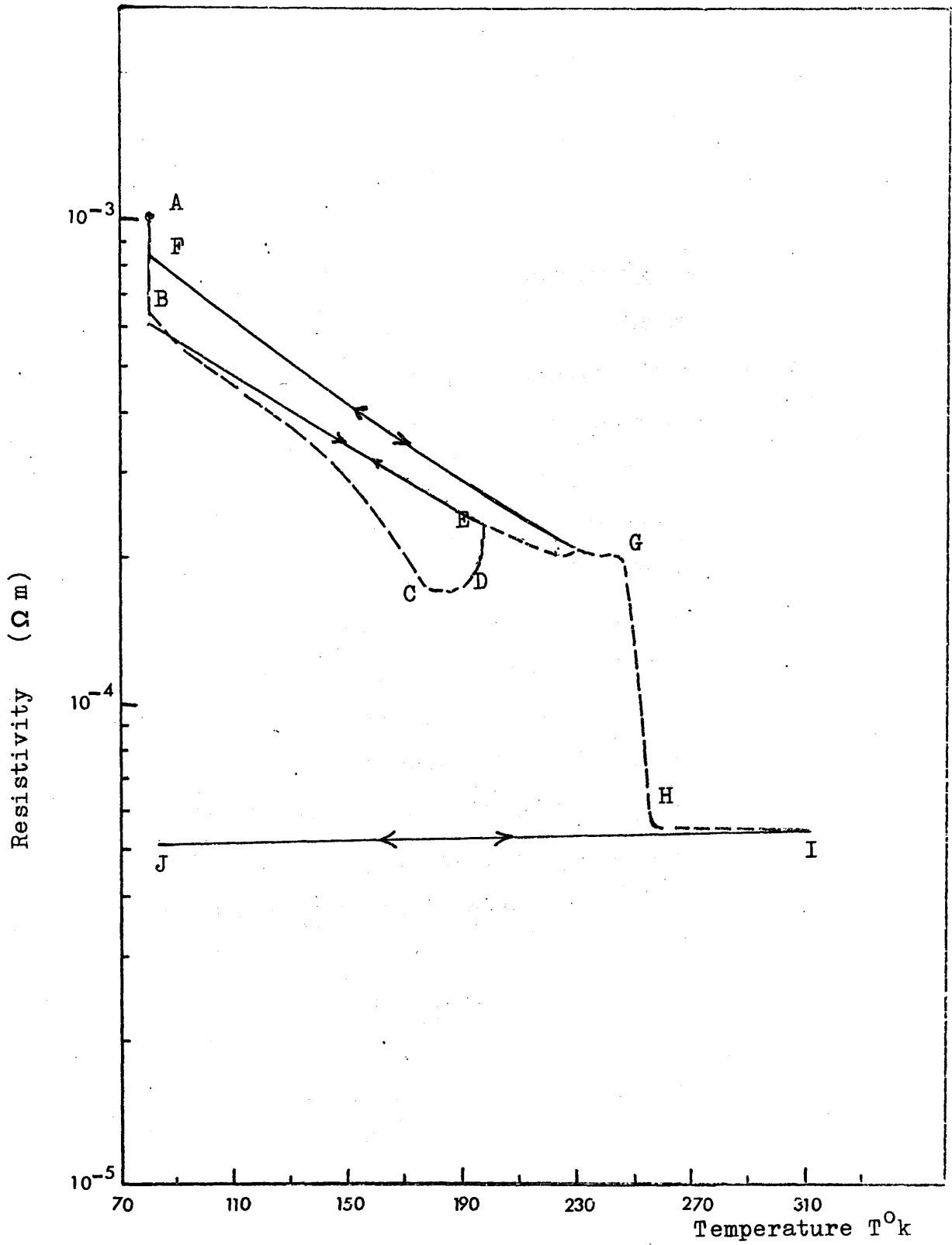
Figure (4.8)   Variation of the d.c. resistivity as a function of

temperature for sample 4 (45.9 ∓ 1.1 at.% Bi).

changes in resistivity, which occur as the sample is
heated from the deposition temperature are apparent in
figure (4.8).   The first change is an irreversible
decrease in resistivity (path A-B-C).   This is followed
by an irreversible increase in resistivity (path C-D-E).
Finally the film crystallizes which is characterized by
a sharp irreversible decrease in resistivity (path G-H).
From figure (4.8) we observe that the sharp drop in
resistivity occurs abruptly and over a small temperature
interval.   This was typical of samples with composition
near to stoichiometry.   The reversible changes shown in
figure (4.8) were generated by cooling the sample after
it had been warmed up and consequently annealed to various
temperatures.   Considering the reversible paths we
notice that a slight decrease in the slope of these paths
over the temperature range defined the first irreversible
path (A-B-C).   But annealing the film at even higher
temperatures causes in some cases a significant increase
in the slopes of reversible paths such as path (K-F),
figure (4.7a).   This behaviour is in agreement with that
observed by Sik (1974) , figure (4.9), and in contrast
to that observed by Herrell (1969)   who found that the
temperature coefficient of resistance T.C.R. defined as

$$T.C.R. \ = \ \frac{1}{R} \ \frac{dR}{dT} \ = \ \frac{d(\ln R)}{dT}$$

was the same for all reversible paths, which indicated
that although the conductivity had changed, the conduction
mechanism remained unchanged as the crystallization temp-
erature was approached.   Finally temperature cycling of
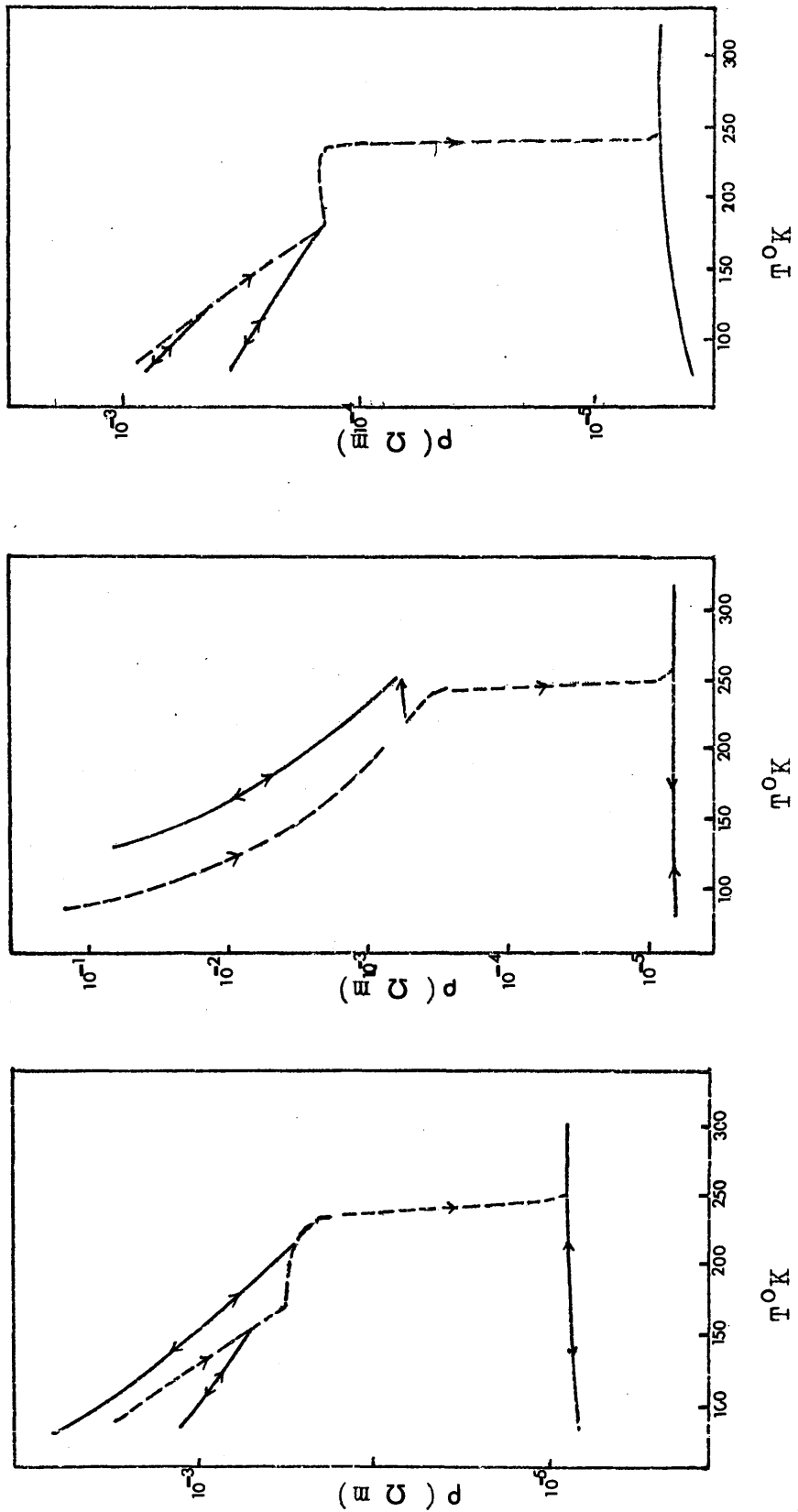
Figure (4.9)   Variation of the d.c. resistivity of three Mg-Bi
               alloys films (a) Magnesium rich.   (b) close to 40
               at.% Bi.   (c) Bismuth rich.   From Sik (1974).

the sample after crystallization indicates that the
resistivity follows the reversible path (I-J) with a
very small positive T.C.R. which indicates a metallic
type behaviour.

In figures (4.10,11) we have also shown the behav-
iour of d.c. resistivity as a function of temperature for
two samples with compositions (36.1 ∓ 1 at.% Bi and
48.4 ∓ 3.5 at.% Bi). From these figures we may observe
the general features encountered due to annealing the
alloy films to higher temperatures. In addition to that,
we may also note that the initial resistivity (the resist-
ivity measured immediately after deposition) of the Mg-Bi
alloy changes for different compositions. It increases
considerably as the composition tends to stoichiometry
figure (4.7). As well as, the initial resistivity
decreases for alloys with compositions away from the
stoichiometric composition (figures 4.10 and 4.11). The
initial resistivities for some of the alloys studied in
this work are listed below.

Composition (at.% Bi)	As deposited Resistivity (Ohm-meter)
36.1 ∓ 1	1.1×10^{-3}
40.3 ∓ 1.6	4.8×10^{-3}
42.4 ∓ 1.1	4.6×10^{-3}
45.9 ∓ 1.1	9.8×10^{-4}
45.8 ∓ 4	5.2×10^{-5}
48.4 ∓ 3.5	5.9×10^{-5}

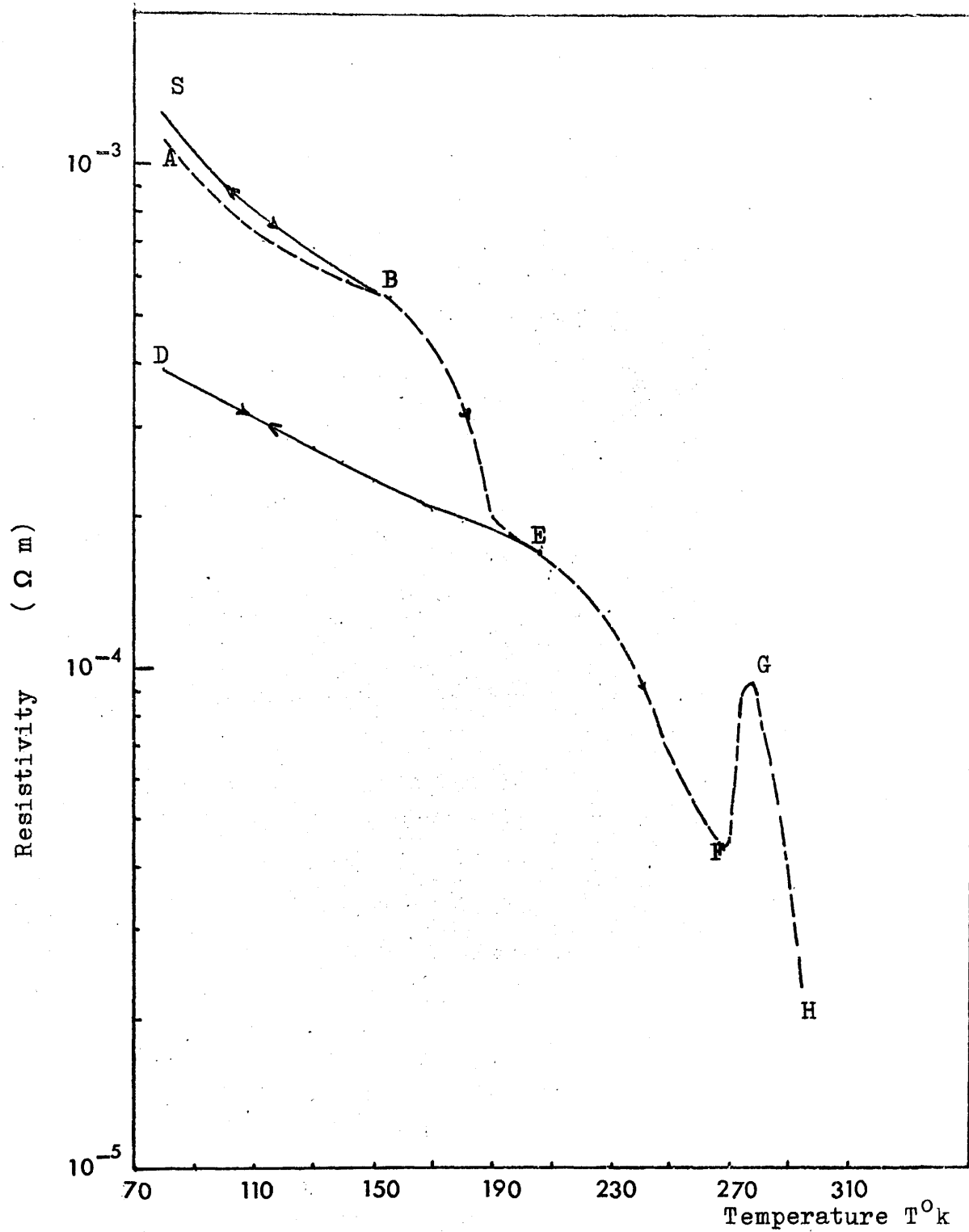From these results it is apparent that alloys near the

Figure (4.10) Variation of the d.c. resistivity as a function of
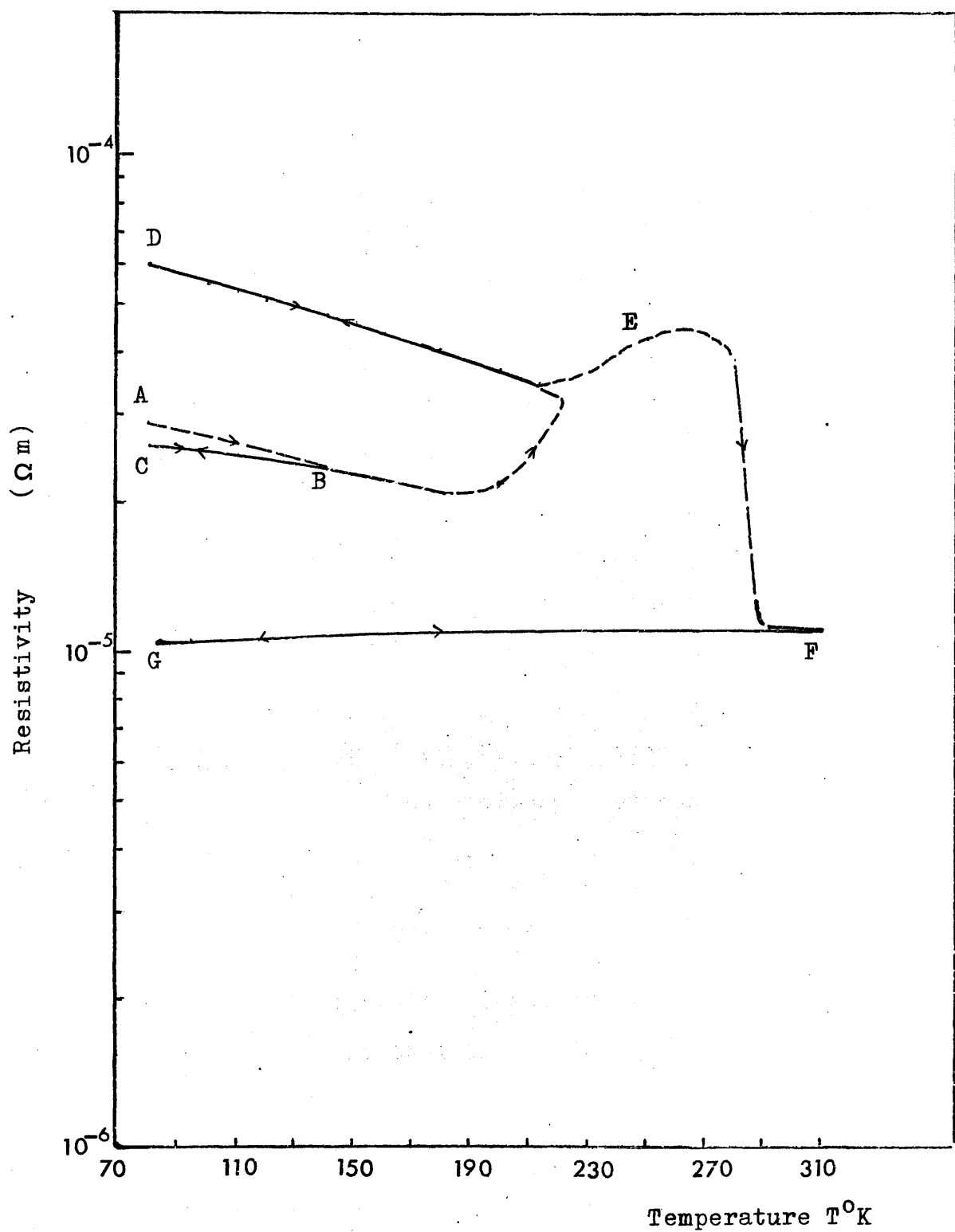temperature for sample 14 (36.1 ∓ 1 at.% Bi)

Figure (4.11)   Variation of the d.c. resistivity as a function

of temperature for sample 15 (48.4 ∓ 3.5 at.% Bi)

intermetallic compound Mg_3Bi_2 have minimum conductivity.
A fairly well defined range of temperatures upon which
the films, near the Mg_3Bi_2, crystalize may be determined.
From this range we find that crystallization occur at
T_c = 240 $\mp$ 10°K, whereas for alloys away from the stoich-
iometric composition the crystallization occurs upon a
broad range of temperature.   Therefore, it is difficult
to estimate a definite temperature range of crystallization
for these alloys.   In figure (4.10) which represents the
behaviour of d.c. resistivity as a function of temperature of
a magnesium rich alloy film, a decrease in the resistivity
path (D-E-F) is observed after the second annealing (210°K).
This behaviour we believe is due to developing metallic
regions.

4.8   Activation Energy for D.C. Conduction

The conductivity of an amorphous semiconductor may be
written as

$$\sigma = \sigma_0 \exp \left(\frac{-E}{kT} \right)$$

Comparing this relation with equations (4.5.1) (4.5.2) and
(4.5.3), it is apparent that the activation energy E will
be a function of temperature.   A plot of lnσ against $1/T$
will only yield a straight line over a particular range of
temperature, if the activation energy, E, is constant or
linearly dependent on temperature over that range and the
pre-exponential factor σ_0 is temperature in dependent over
the same range of temperature.   Figure (4.12) shows the plots
of lnσ versus $1/T$ that may be applicable to a general
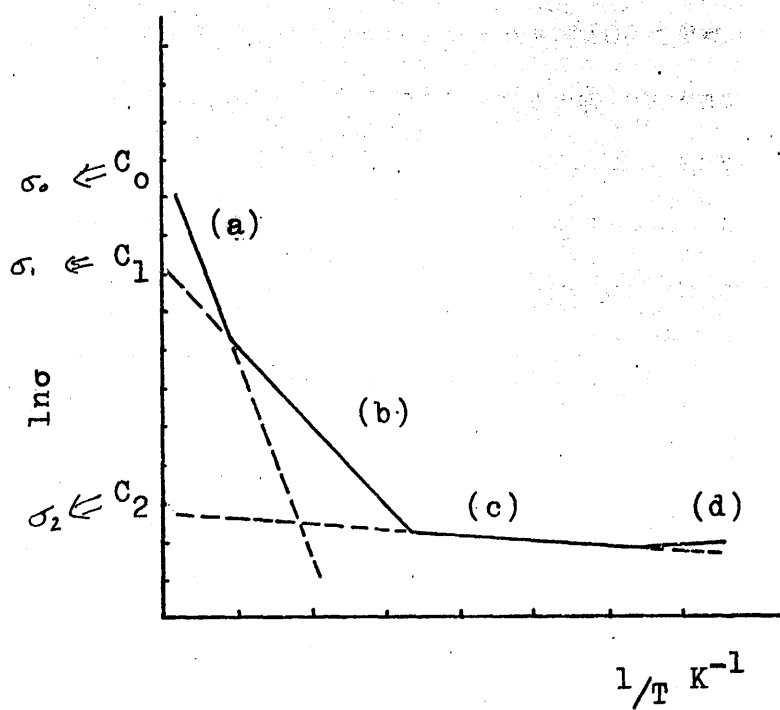
Figure (4.12)   Illustration of the temperature dependence
of conductivity applicable to amorphous
semiconductors.

amorphous semiconductor (Mott and Davis (1971)).

The $\ln \sigma$ against $1/_T$ graphs for the reversible paths (K-F) figure (4.7a), (F-G) figure (4.8) and (D-E) figure (4.10) are presented in figure (4.13). It is seen from these graphs that the points are not . . . linear except perhaps at high temperatures ($200 < T < 240$), therefore, any determination of the activation energy must be made with extreme caution. However, the activation energies calculated by extrapolating the most linear region of $\ln \sigma$ versus $1/_T$ curves are given below.

Sample	Composition at.% Bi	Activation Energy (eV)
14	36.1 ∓ 1	0.055 ∓ 0.01
6	42.4 ∓ 1.1	0.079 ∓ 0.01
4	45.9 ∓ 1.1	0.04 ∓ 0.01

Figure (4.13) The temperature dependence of d.c. conductivity.

(a) log σ versus $10^3/T$ of sample 14

(b) log σ versus $10^3/T$ of sample 4

(c) log σ versus $10^3/T$ of sample 6

4.9   Annealing Effects

The general features encountered due to annealing
the Mg-Bi alloy film were discussed in section (4.7).
We have reported three distinct irreversible changes in
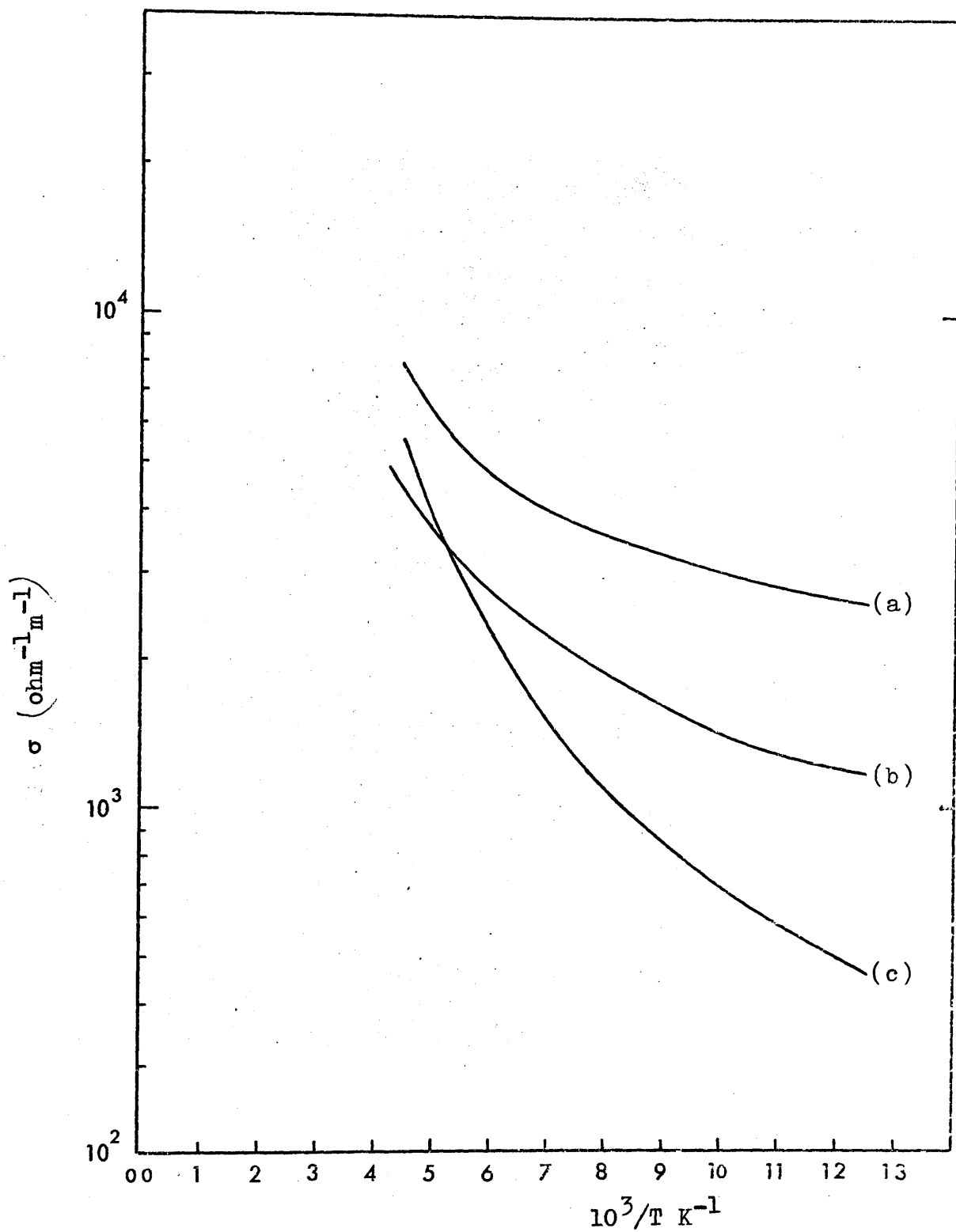the resistivity of the films.   First, irreversible drop
in the resistivity with a negative temperature coefficient
of resistance (T.C.R), followed by an increase in the
resistivity (positive T.C.R.), then the most striking
irreversible change in the resistivity associated with
the transformation of amorphous films to the polycrys-
talline state.   We have also seen reversible changes in
the d.c. resistivity which were generated by cycling the
temperature after the first and second irreversible
changes.

In this section we shall discuss the affects of
annealing the films to higher temperatures after deposition
near liquid nitrogen temperature.   At the preparation
temperature, near 77°K, the Mg-Bi alloy films are highly
disordered as is the case in any amorphous material and
exist as amorphous Mg_3Bi_2 with local concentration excesses
of magnesium or bismuth.   Now considering the annealing of
the alloy films to higher temperatures above the deposition
temperature, for the first annealing stage (irreversible
decrease in resistivity) we hypothesise a general annealing
of defects such as voids, dangling bonds and vacancies
which are formed during the film deposition.   As regards
the second annealing stage (200 - 230°K) in which the
resistivity rises, figure (4.14), this undoubtedly involves
atomic rearrangement, with more interdiffusion of the mag-
nesium and the bismuth removing local concentration maxima
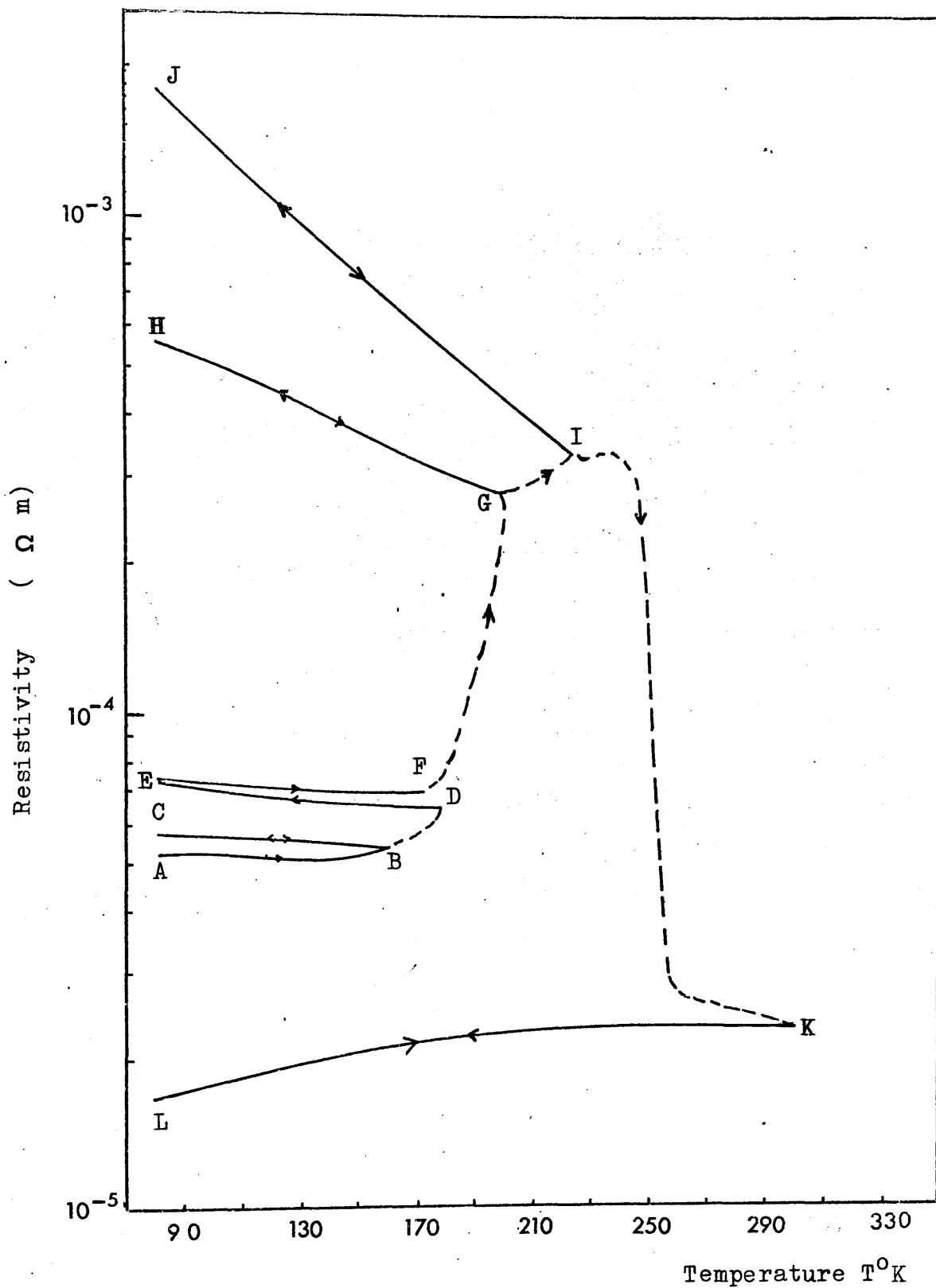
Figure (4.14) Variation of the d.c. resistivity as a function
of temperature for sample 3 (45.8 ∓ 4 at.% Bi).

of either constituent and producing a more uniform
system.   There is also in all probability some growth
of metallic regions and crystalline Mg_3Bi_2 at this stage,
figure (4.10).   Evidence which supports this view is
obtained from the optical measurements Chapter 5.
Earlier structural studies are also in agreement with
this view (Herrell (1969)).   Herrell made electron micro-
scope studies of magnesium bismuth films at liquid nitrogen
temperature and above.   After deposition a diffraction
pattern containing the broad halos characteristic of the
amorphous state was observed which remained unchanged until
annealling commenced, when the diffraction pattern started
to sharpen up.   At the same time, detail appeared on high
magnification images of the film corresponding to formation
of crystalline grains, which grew until above the crystall-
isation temperature the film became polycrystalline and no
further changes were observed up to room temperature.   In
some films the grains formed on anneal could be identified
as of being excess bismuth.

C H A P T E R   5

OPTICAL MEASUREMENTS

5.1   Introduction

The optical properties of any absorbing material are
specified by the variation of the complex refractive index
(N = n $-ik$) of that material with light wavelength (photon
energy), where n is "the ordinary refractive index" and k
the "extinction coefficient".   Different optical measure-
ments can be made to determine n and k, e.g. normal
incidence reflectance and transmittance, ellipsometric and
polarimetric measurements.   The most widely used method
is to obtain both n and k from the two independent
measurements of normal reflectance (R) and transmittance
(T) of the same material.   The equations for the reflectance
and transmittance are complicated, and a good deal of
computing is normally required.

The measurements chosen to determine the optical
constants n and k for the amorphous Mg-Bi alloy films
were the normal incidence transmittances of two films with
the same composition but different in thickness.   The
two films were prepared at the same time in the same
vacuum system.   Normal incidence transmittance measure-
ments have a number of advantages.   They may be made
easily, conveniently and with high accuracy.   Systematic
error in reflectance measurements (R) due to non-flatness

of the substrate and the sample surfaces can signifi-
cantly affect the measured R.   Also it is necessary
to provide an excellent reflection standard in order to
obtain accurate R.   Although the R - T method is
intrinsically more accurate (Nilsson (1968)) , these
systematic errors in R tend to nullify this advantage.

5.2   Equations

It is a considerable task to determine the optical
constants of a thin film from experimental data, mainly
because the equations normally used to carry out the
computation are extremely complex.   In this section we
shall give the equations without derivation since it is
cumbersome algebra.

When a light beam incident normally upon an absorbing
film supported by a transparent substrate, part of that
beam is transmitted, part of it is absorbed within the
film and another part is reflected.   The transmitted
beam is subject to multiple reflections within the film.
The films _thicknesses_ are of the same order as the wavelength of the
light, hence interference occurs between the successively
reflected beams.   The equations governing the transmittance
(T_f) and the reflectance (R_f) of an absorbing film deposited
on a transparent substrate are (Abeles (1967)) :

$$R_f = \frac{A \exp(\alpha) + B \exp(-\alpha) - C \cos \beta + D \sin \beta}{E \exp(\alpha) + F \exp(-\alpha) - G \cos \beta + H \sin \beta} \quad (5.2.1)$$

$$T_f = \frac{16 \ N_o N_2 \ (n^2 + k^2)}{E \exp(\alpha) + F \exp(-\alpha) - G \cos \beta + H \sin B} \quad (5.2.2)$$

where $\qquad \alpha = \dfrac{4 \pi kd}{\lambda}$, $\qquad \beta = \dfrac{4 \pi nd}{\lambda}$

$$A = ((n - N_0)^2 + k^2) \ ((n + N_2)^2 + k^2)$$

$$B = ((n + N_0)^2 + k^2) \ ((n + N_2)^2 + k^2)$$

$$C = 2 \ ((n^2 + k^2 - N_0^2) \ (n^2 + k^2 - N_2) + 4N_0 k^2 N_2)$$

$$D = 4k \ (N_2 - N_0) \ (n^2 + k^2 + N_0 N_2)$$

$$E = ((n + N_0)^2 + k^2) \ ((n + N_2)^2 + k^2)$$

$$F = ((n - N_0)^2 + k^2) \ ((n - N_2)^2 + k^2)$$

$$G = 2((n^2 + k^2 - N_0^2) \ (n^2 + k^2 - N_2^2) - 4N_0 k^2 N_2)$$

$$H = 4k(N_2 + N_0) \ (n^2 + k^2 - N_0 N_2)$$

λ is the wavelength of the light, d is the film thickness and N_0 and N_2 are the refractive indices of the surrounding medium (which is considered to be unity) and the substrate respectively. The refractive index of the film is $N = n - ik$. The reflectance R_f' and the transmittance T_f' from the substrate side of the film figure (5.1) are given by

$$R_f' = \frac{B \exp (\alpha) + A \exp (-\alpha) - C \ Cos \ \beta - D \ Sin \ \beta}{E \exp (\alpha) + F \exp (-\alpha) - G \ Cos \ \beta + H \ Sin \ \beta} \qquad (5.2.3)$$

$$T_f' = T_f \qquad\qquad\qquad (5.2.4)$$

The thin film can be replaced by a single interface with reflection and transmission coefficients R_f, T_f, R_f', T_f' figure (5.1). Multiple reflections within the substrate must be considered so that expressions for the overall transmittance T and reflectance R of the film and substrate may be evaluated. T and R can be found directly by adding the intensities of the contributing beams. Hence
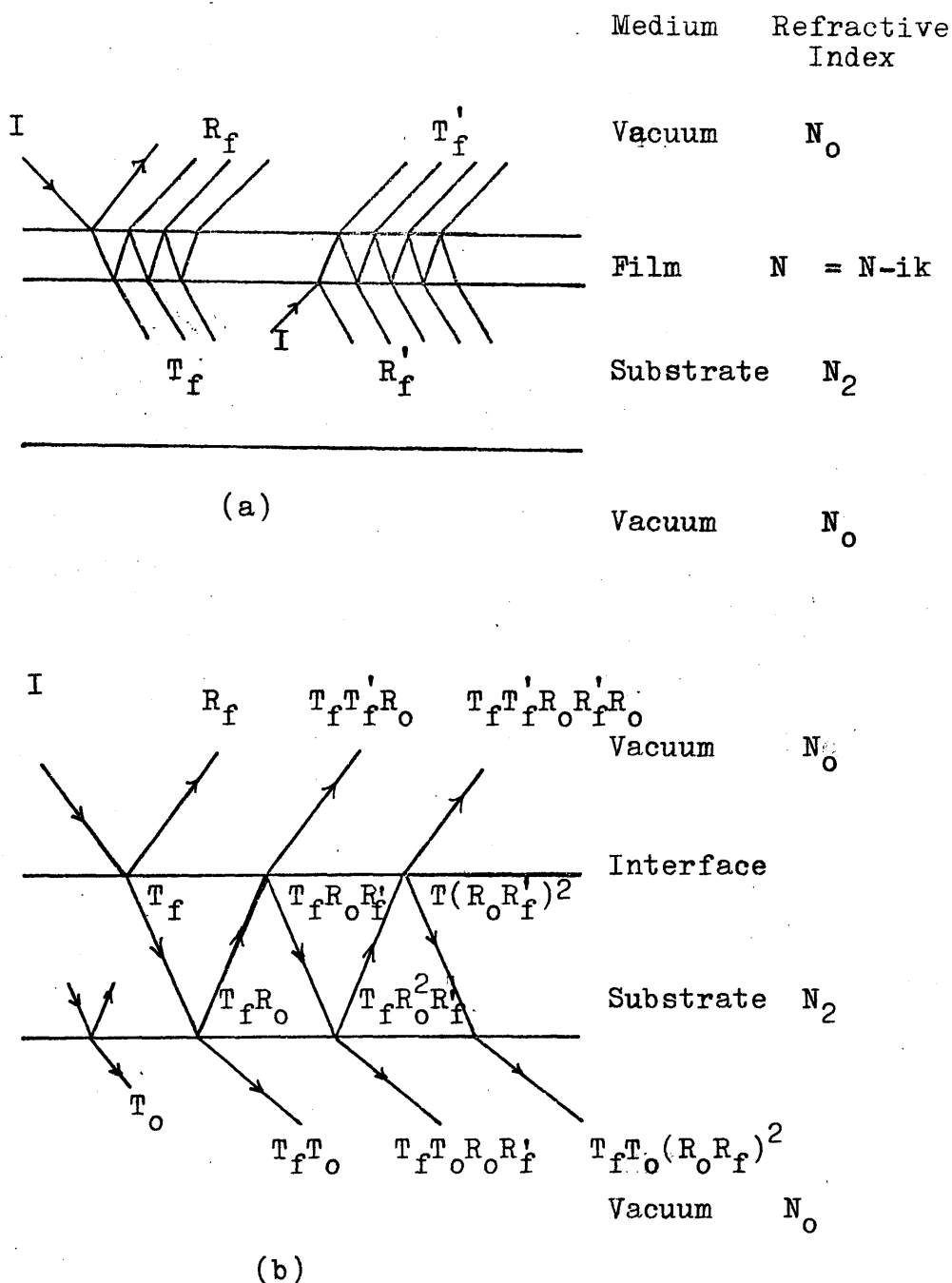
Figure (5.1) The path of the light beam within the sample and substrate. The beam is incident normally but has been drawn at an oblique angle for clarity (Sutton (1975)).

(a) Multiple reflections within the thin film sample.

(b) Multiple reflections within the substrate. The film has been replaced by a single interface.

from figure (5.1) the total reflected intensity

$$R = R_f + T_f T_f' R_o + T_f T_f' R_o R_f' R_o + \cdots \quad (5.2.5)$$

or

$$R = R_f + \frac{T_f^2 R_o}{1 - R_o R_f'} \quad (5.2.6)$$

Similarly, the total transmitted intensity

$$T = T_f T_o + T_f T_o R_o R_f' + T_f T_o R_f'^2 R_o^2 + \cdots \quad (5.2.7)$$

or

$$T = \frac{T_f T_o}{1 - R_o R_f'}, \quad (5.2.8)$$

T_o and R_o are the transmittance and the reflectance of the substrate respectively, these are given by

$$T_o = \frac{4 N_o N_2}{(N_2 + N_o)^2} \quad (5.2.9)$$

and

$$R_o = \left(\frac{N_2 - N_o}{N_2 + N_o} \right)^2 \quad (5.2.10)$$

R and T in equations (5.2.6) and (5.2.8) are functions of n and k, d, λ, N_2 and N_o. The refractive index for air at standard temperature ($0^\circ C$) and pressure (760 m m.Hg) is 1.00292– (Jenkins and White (1976)). The alloy films were prepared at temperature near to $77^\circ K$ and pressure 4×10^{-7} torr approximately. Hence N_o could be considered unity while dispersion relations were used for the refractive index N_2 of the substrate. For sapphire substrate the dispersion relation is (Malitson (1962))

$$N_2^2(\lambda) = 1 + \sum_{i=1}^{3} A_i \cdot \lambda^2 / (\lambda^2 - \lambda_i^2) \quad (5.2.11)$$

For $0.265 < \lambda < 5.58$ μm

where

$$A_1 = 1.023798 \qquad \lambda_1^2 = 0.00377588$$

$$A_2 = 1.058264 \qquad \lambda_2^2 = 0.0122544 \qquad \Big\} (A^\circ)^2$$

$$A_3 = 5.280792 \qquad \lambda_3^2 = 321.3616$$

5.3 Determination of the Refractive Index

The real and imaginary parts (n and k respectively) of the complex refractive index for the amorphous Mg-Bi alloys, were determined from the measured transmittances of the two films at any particular wavelength λ .

Equation (5.2.8) was inverted in terms of n and k and reduced to a quadratic equation in $x = e^{\alpha d}$.

Re-writing equation (5.2.8)

$$T(1 - R_0 R_f') = T_f T_o \qquad (5.3.1)$$

$$T(1 - R_0 R_f') = T_f T_o \qquad\qquad \text{rom}$$

substitution of T_f from equation (5.2.2) and R_f' from[1] equation (5.2.3) and putting $x = e^{\alpha d}$ we obtain

$$T - TR_0 \left(\frac{Bx + A/x - C \cos \beta - D \sin \beta}{Ex + F/x - G \cos \beta + H \sin \beta} \right)$$

$$= \frac{16 N_0 N_2 (n^2 + k^2)}{Ex + F/x - G \cos \beta + H \sin \beta} \qquad (5.3.2)$$

Rearranging equation (5.3.2) we get

$$T(Ex + F/x - G \cos \beta + H \sin \beta)$$

$$- TR_0 (Bx + A/x - C \cos \beta + D \sin \beta)$$

$$= 16 N_0 N_2 (n^2 - k^2) T_o$$

or

$$T (Ex^2 + F - x \ G \ Cos \ \beta + x \ H \ Sin \ \beta)$$
$$- TR_o(Bx^2 + A - x \ C \ Cos \ \beta - x \ D \ Sin \ \beta)$$
$$= 16 \ N_oN_2 \ (n^2 + k^2) \ T_ox \qquad (5.3.3)$$

Equation (5.3.3) may be written in the form

$$(E- R_oB)x^2$$
$$+((R_oC \ Cos \ \beta - G \ Cos \ \beta + H \ Sin \ \beta + R_o \ D \ Sin \ \beta)$$
$$- \frac{16 \ N_2N_oT_o \ (n^2 + k^2)}{T})x + (F - R_oA) = o \qquad (5.3.4)$$

Equation (5.3.4) was then solved as quadratic and the
summed solution was taken as the correct solution since
we required $a > o$.

The solution for equation (5.3.4), at any particular
wavelength, was found from T, by first setting n $= 1$
and $k_1 = o$ until convergence was obtained to give an
estimate for k_1, the new value for k, was then fed back
to obtain a better estimate for k_1. The same
procedure was followed to obtain an estimate for k_2 from
T_2. Then n was varied continuously until a minimum was
obtained for $(k_1(n) - k_2(n))$. For some wavelengths
close to "critical points" where the thickness of one of
the films was an integral number of half wavelengths exact
convergence was not obtained. In this case the programme
(Appendix A) returned a mean value, $\bar{k} = \frac{1}{2} (k_1 + k_2)$.

5.4   Transmittance Measurements

At any particular wavelength the normal incidence
transmittance was determined by first measuring the
reference beam intensity I_o with the sample removed

from the optical path. Then the transmitted beam intensity I_t, the attenuated signal, was measured with the sample placed in the optical path. Hence the transmittance T was defined as the ratio

$$T = I_t/I_o$$

I_o and I_t were measured as functions of wavelength in the range 0.8 - 2.8 μm (0.443 - 1.55 eV), since that was the range of interest, and the infra-red detector used was limited to wavelengths greater than 0.8 μm, and the quartz prism monochromater defined the minimum wavelength studied. Systematic error in T due to drift in the light output of the source, and due to inaccuracies in optical alignment was studied by repeating measurements of I_o and I_t. In later samples (14 and 15) the apparatus was modified to enable point by point comparison of I_o and I_t to be performed. T was measured to better than 1% at each position and each wavelength.

5.5   Sample Geometry and Beam Displacer

The optical samples were prepared in the form of two films with different thicknesses. The sample geometry used to measure the transmittance (T) is illustrated in figure (5.2). T was determined by measuring the transmitted beam intensity at two positions for each film, and dividing by the unattenuated beam intensity for the same positions.

A specifically designed beam displacer figure (5.3), was used to shift the light focussed at the sample. This enabled us to measure the transmitted beam intensity at
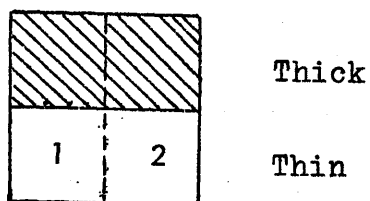
Thick

Thin

Figure (5.2) Optical sample geometry

Entrance

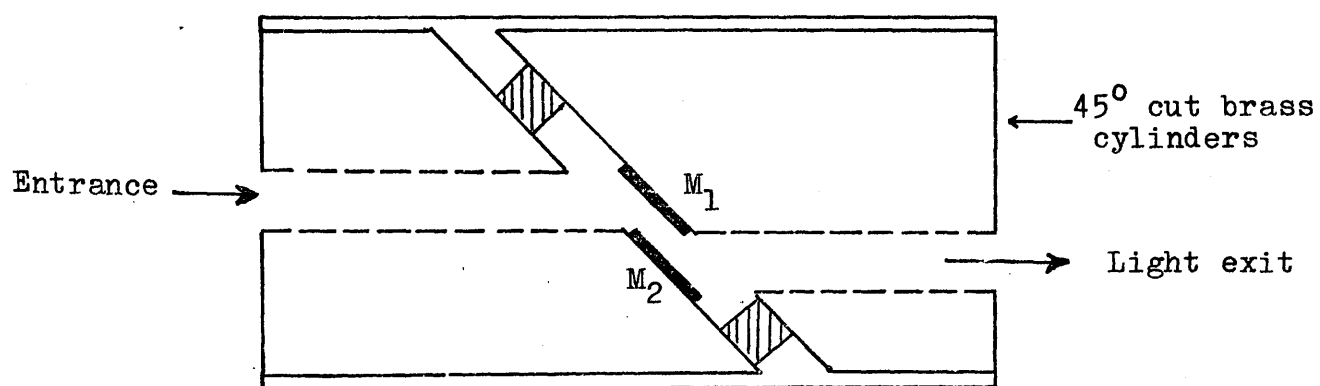45° cut brass
cylinders

Light exit

M_1

M_2

Figure (5.3) Beam Displacer.
M_1 and M_2 are the two reflecting mirrors.

four positions on the two films.   The beam displacer
was constructed from two plane mirrors mounted on brass
cylinders cut at 45°.   These cylinders were placed
opposite to each other inside another hollow cylinder.
The light was passed through a path at the centre of the
first cylinder, and after being reflected by the two
mirrors, it emerged from another path at the second side
of the other cylinder.   The light was shifted 6 mm from
its original path.   The beam displacer could be rotated
inside accurately aligned roller bearings.

5.6   Sample Temperature

It is seen from plate (2) that the optical sample
holder is remote from the copper thermometer and so its
temperature is not directly known.   To determine the
actual temperature of the substrate surface, a special
experiment was carried out.   The sensor of the convent-
ional copper-eureka thermocouple was strapped to the
surface of the sapphire substrate used for optical trans-
mittance measurements and the other junction was placed
in the reference temperature bath (in crushed melting ice).
The sample holder (the insert) was placed in its position
inside the vacuum system which was pumped overnight.   The
Meissner trap was filled with liquid nitrogen and the
holder was cooled down to near liquid nitrogen.   The
system was left for at least one hour.   The copper ther-
mometer reading at that point indicated that the temper-
ature of the copper base plate and the surroundings was
80 $\mp$ 1°K.   The potential difference across the thermo-

couple was then measured, and this was compared with potential difference developed across the same thermo-couple when calibrated (using liquid nitrogen and meltin crushed ice). The showed that the optical sample temperature was $83 \mp 1^{o}K$. When the optical sample holder was rotated 90° and then illuminated, the thermo-couple indicated an average of $5 \mp 2^{o}K$ temperature difference between the optical sample and the copper thermometer at various temperatures.

5.7 Transmittance of Mg-Bi Alloy Films

The transmittances (T_1 and T_2 for thick and thin films respectively) were measured at two positions for each film. Typical curves of T as a function of wave-length taken for sample (11) are shown in figure (5.4) to illustrate the difference in the measured transmittances at two positions. These differences are attributed to fluctuations in composition along with film thickness variation and partly due to small drifts in the light output of the source.

Transmittances as a function of wavelength for the deposited, annealed and crystalline alloys of different compositions (samples 14, 7, and 15) are illustrated in figures (5.5, 5.6 and 5.7). Sample 7 had the closest composition to the stoichiometric composition. The general features of the behaviour of the transmittances, for the alloys studied as a function of wavelength were similar, particularly samples 7 and 11. Significant changes in T occurred when the alloy films were annealed.

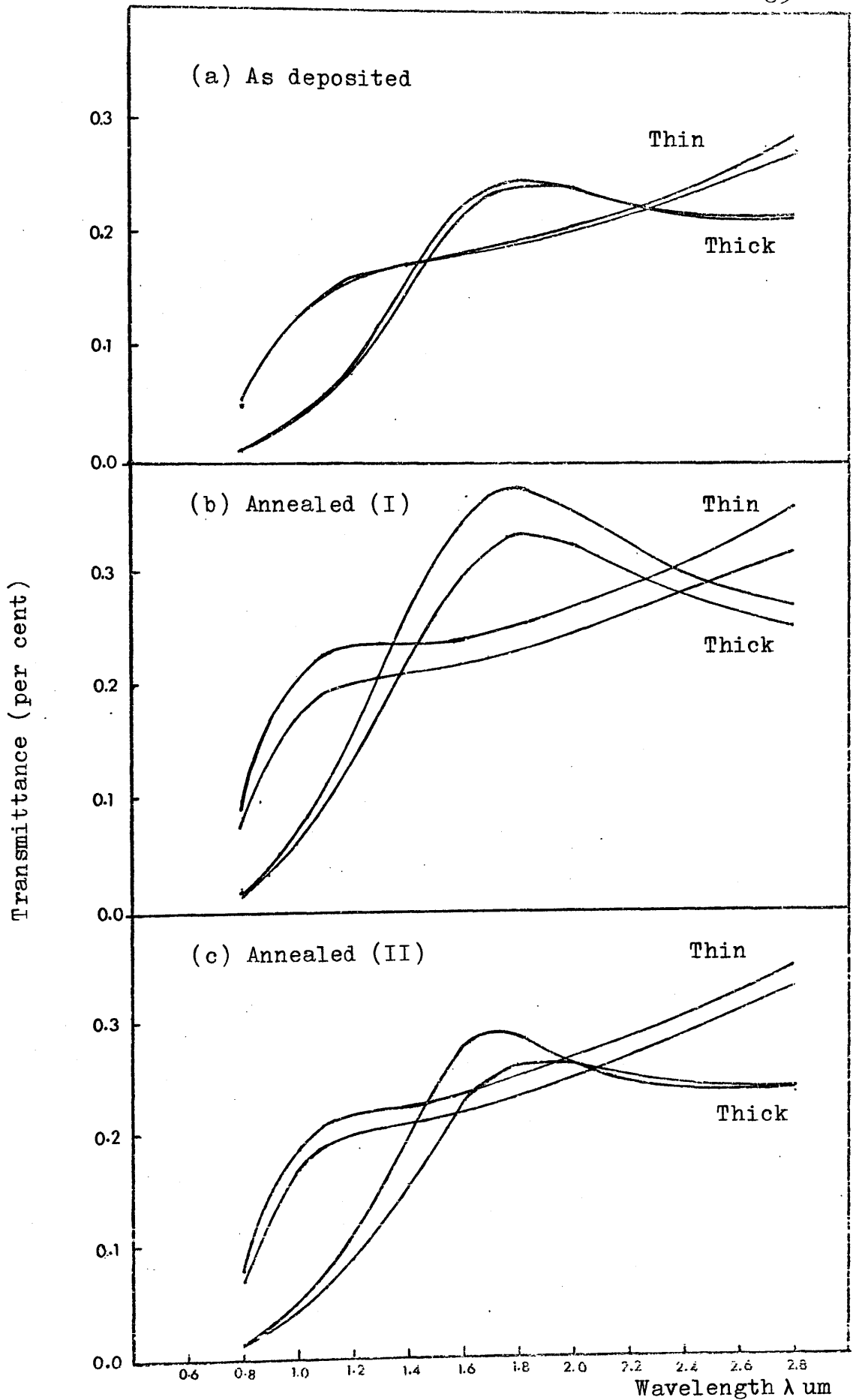Figure (5.4)   Optical transmission as a function of wavelength
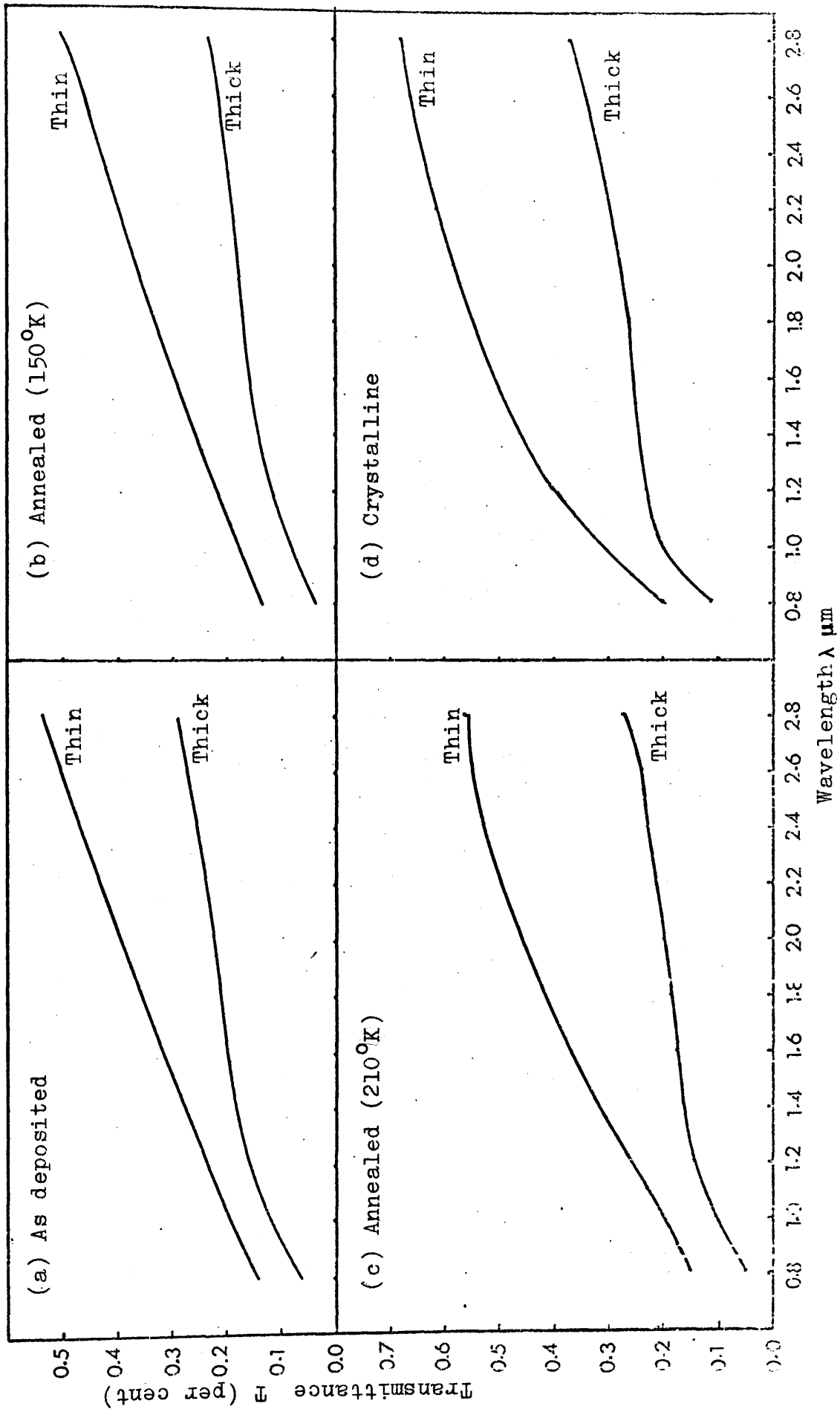for sample 11 (41.1 ∓ 2.5 at.% Bi).

Figure (5.5) Transmittance (T) as a function of wavelength
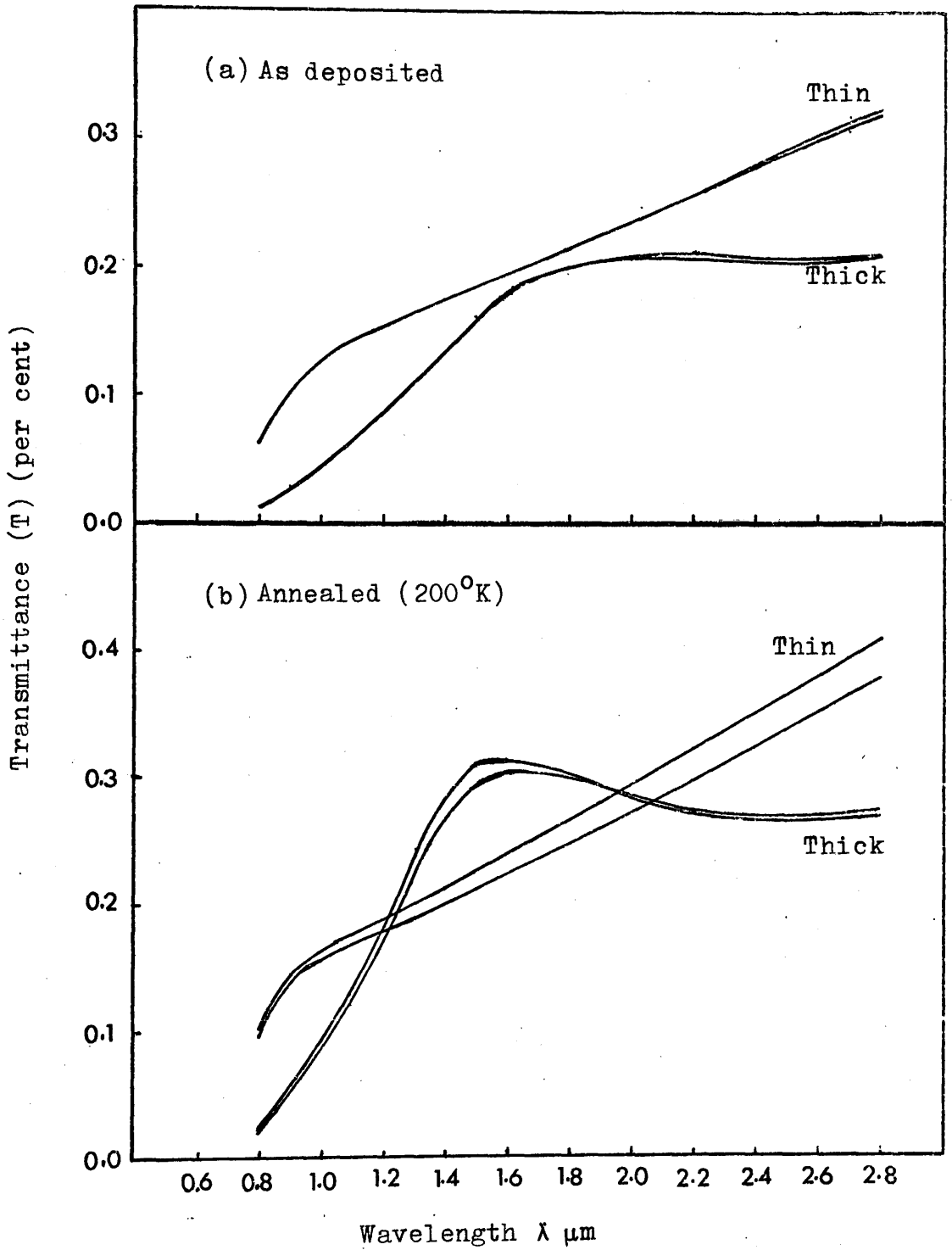for sample 14 (36.1 ∓ 1 at.% Bi).

Figure (5.6) Transmittances (T) as a function of wavelength
for sample 7 (40.4 ∓ 1.6 at.%)

(a) As deposited

(b) Annealed to 200°K.
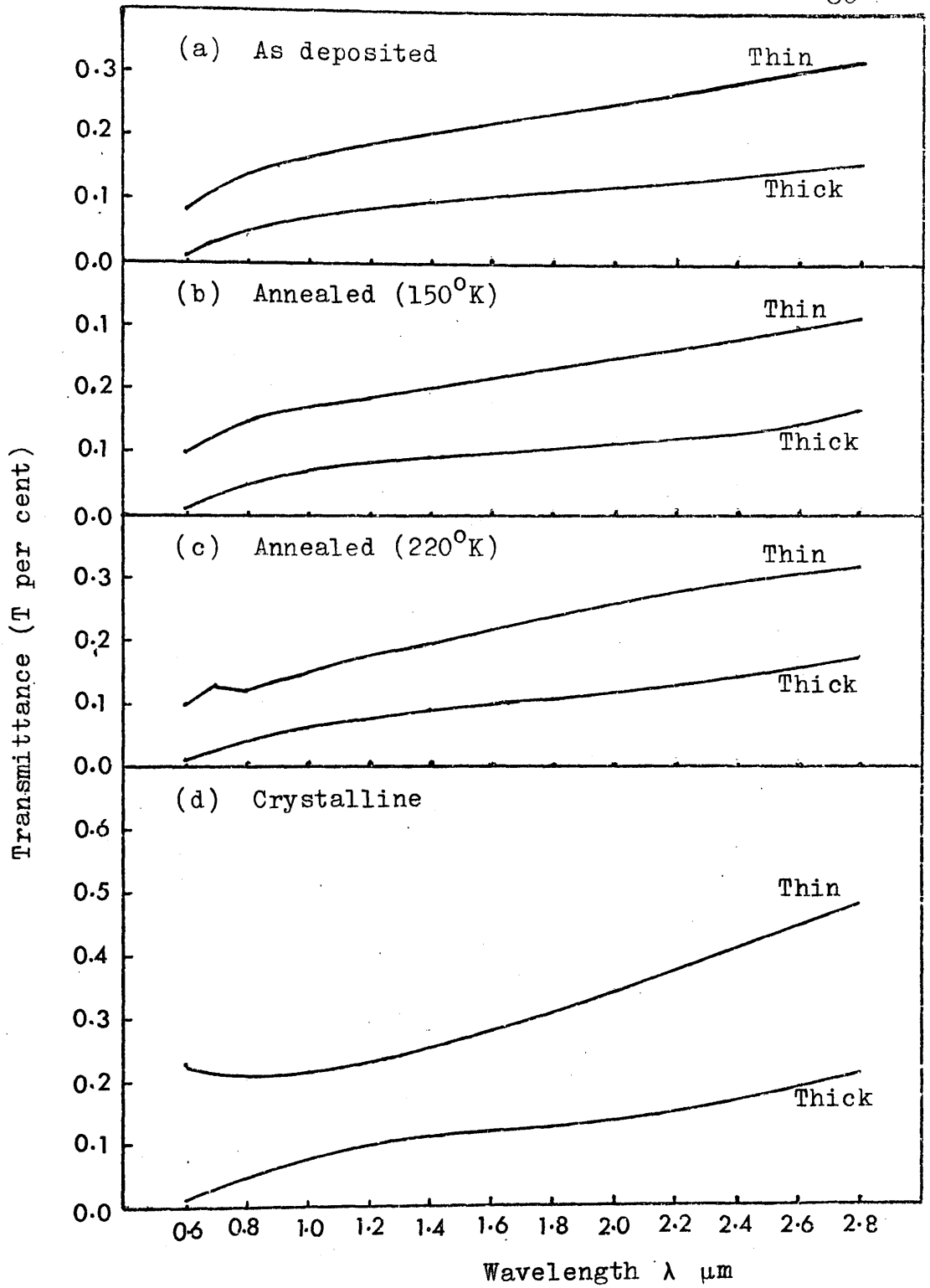
Figure (5.7) Transmittance (T) as a function of wavelength for sample 15 (48.4 ∓ 3.5 at.% Bi)

These changes in T indicated structural changes in the films. The most significant changes occurred were the additional attenuation at low energies and upon crystall-ization when the metallic absorption developed.

5.8 The Refractive Index of Mg-Bi Alloys

The method used to determine the real and imaginary parts, n and k, of the complex refractive index was outlined in section 5.4. When equation (5.3.4) was solved for n and k, more than one solution was found particularly in the vicinity of critcal values of d/λ.

This was not typical over the whole energy range 0.44 - 1.55 eV. Single solutions, physically correct solutions, were also found. For example n and k, at different energies, for three samples, are shown below to illustrate the multiple solutions.

Composition at.% Bi	Energy (eV)	n	k
36.1	1.55	(i) 4.287	1.618
		(ii) 9.921	0.952
	0.954	(i) 4.686	1.272
	0.729	(i) 4.907	0.929
	0.443	(i) 5.376	0.335
		(ii) 1.345	3.428
40.4	1.378	(i) 4.163	1.517
		(ii) 6.317	1.298

Composition at.% Bi	Energy (ev)	n	k
	0.954	(i) 4.181	1.24
		(ii) 6.296	0.672
		(iii) 10.506	0.255
	0.729	(i) 4.495	0.898
	0.459	(i) 4.951	0.300
48.4	1.55	(i) 4.352	1.145
		(ii) 7.21	0.825
	0.954	(i) 3.580	1.401
		(ii) 9.218	0.793
	0.729	(i) 3.455	1.594
	0.477	(i) 3.35	1.824

It is clear from these results that the single solutions, at certain energies, were consistant with one of the solutions at other energies. The criterian used to determine the physically correct solutions was;

a. The single solutions of n and k were taken as the physically correct solutions.

b. Since n and k varied slowly, and from the continuity with energy, values close to the single solutions were chosen at energies where the multiple solutions existed.

The variation of n and k with energy are illustrated for four samples 14, 7, 11 and 15, figures (5.8, 5.9, 5.10 and 5.11 respectively).
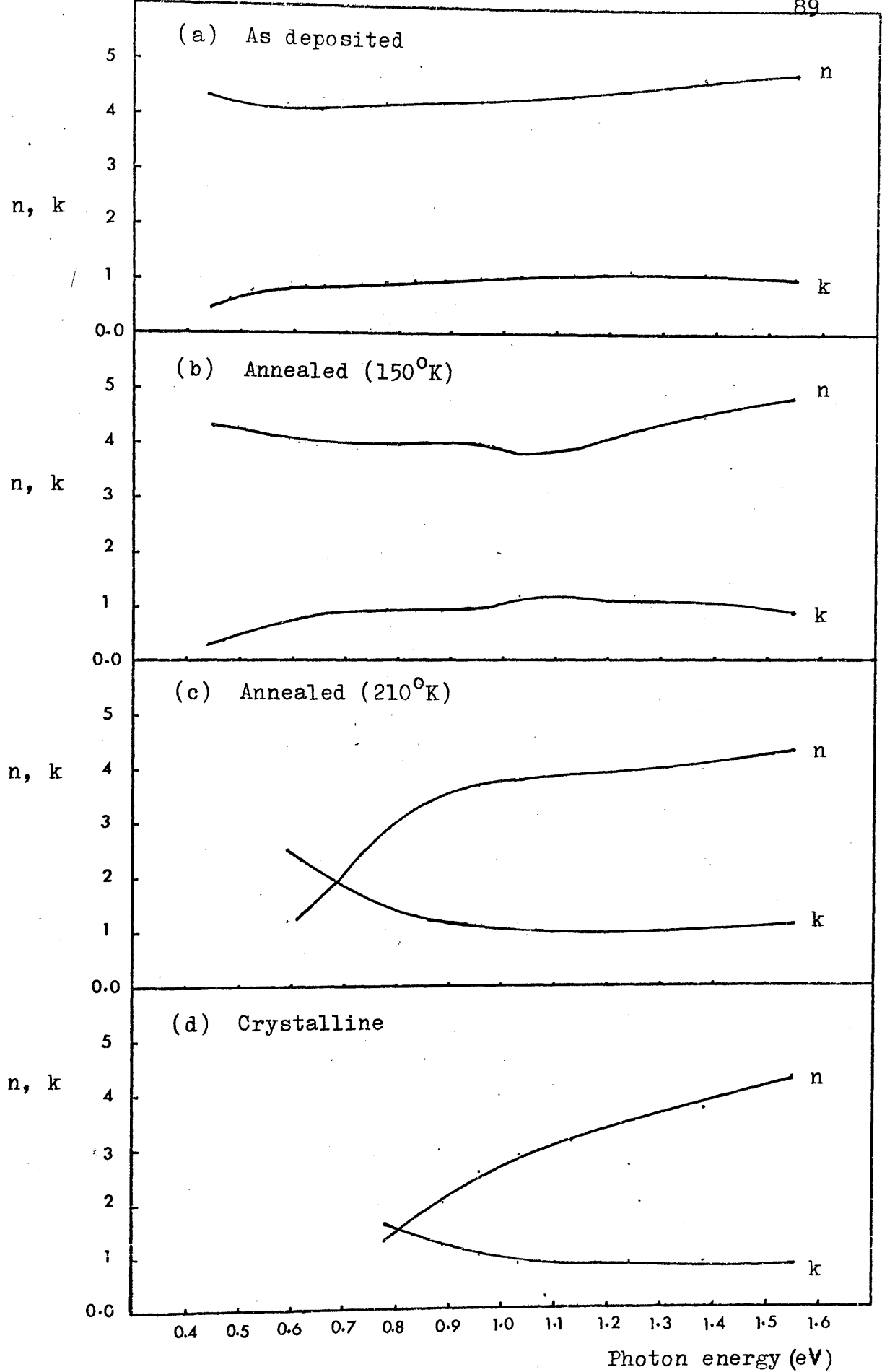
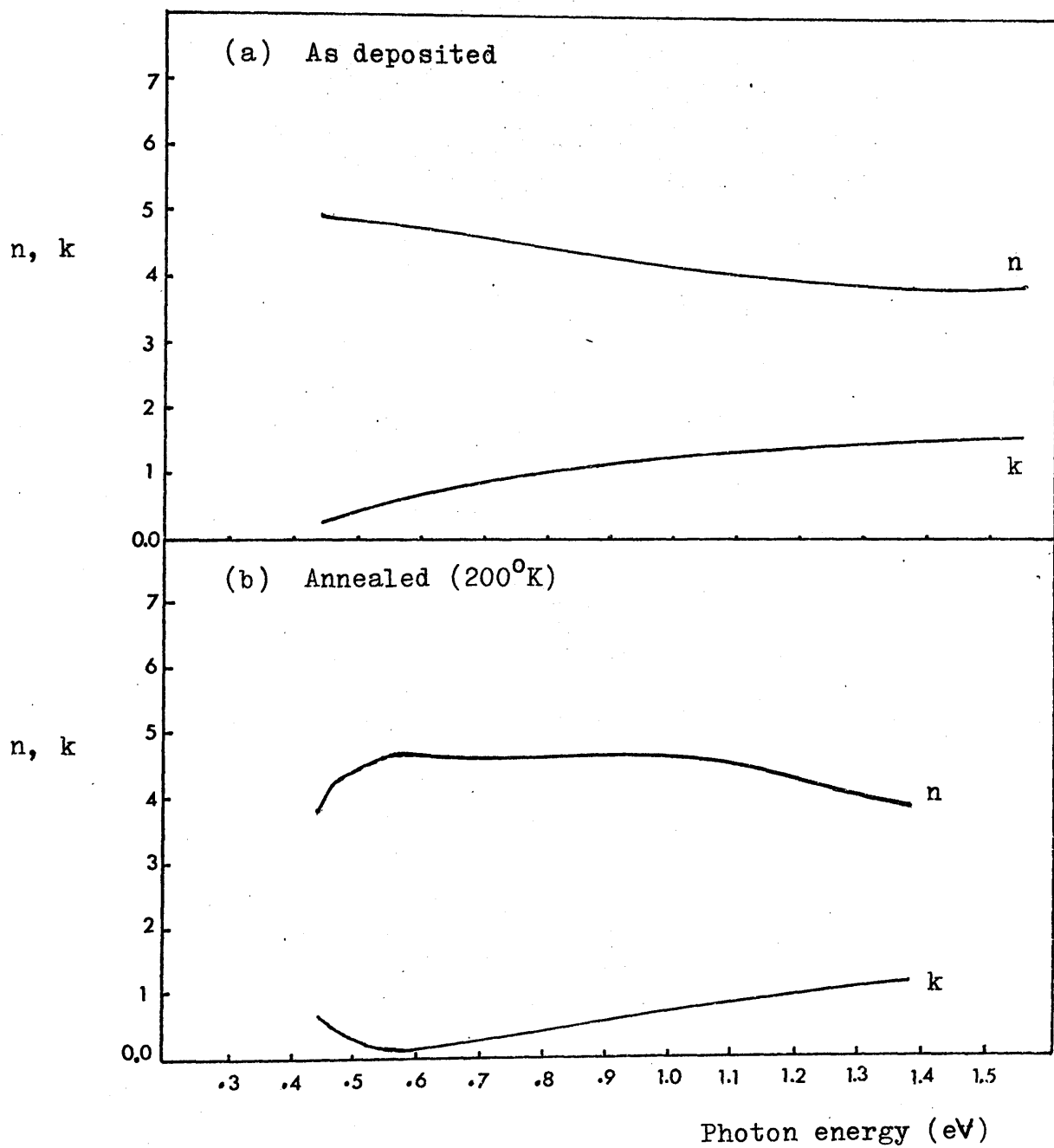Figure (5.8) Variation of n and K with photon energy for sample 14 (36.1 ∓ 1 at.% Bi).

Figure (5.9)   Variation of n and k with photon energy
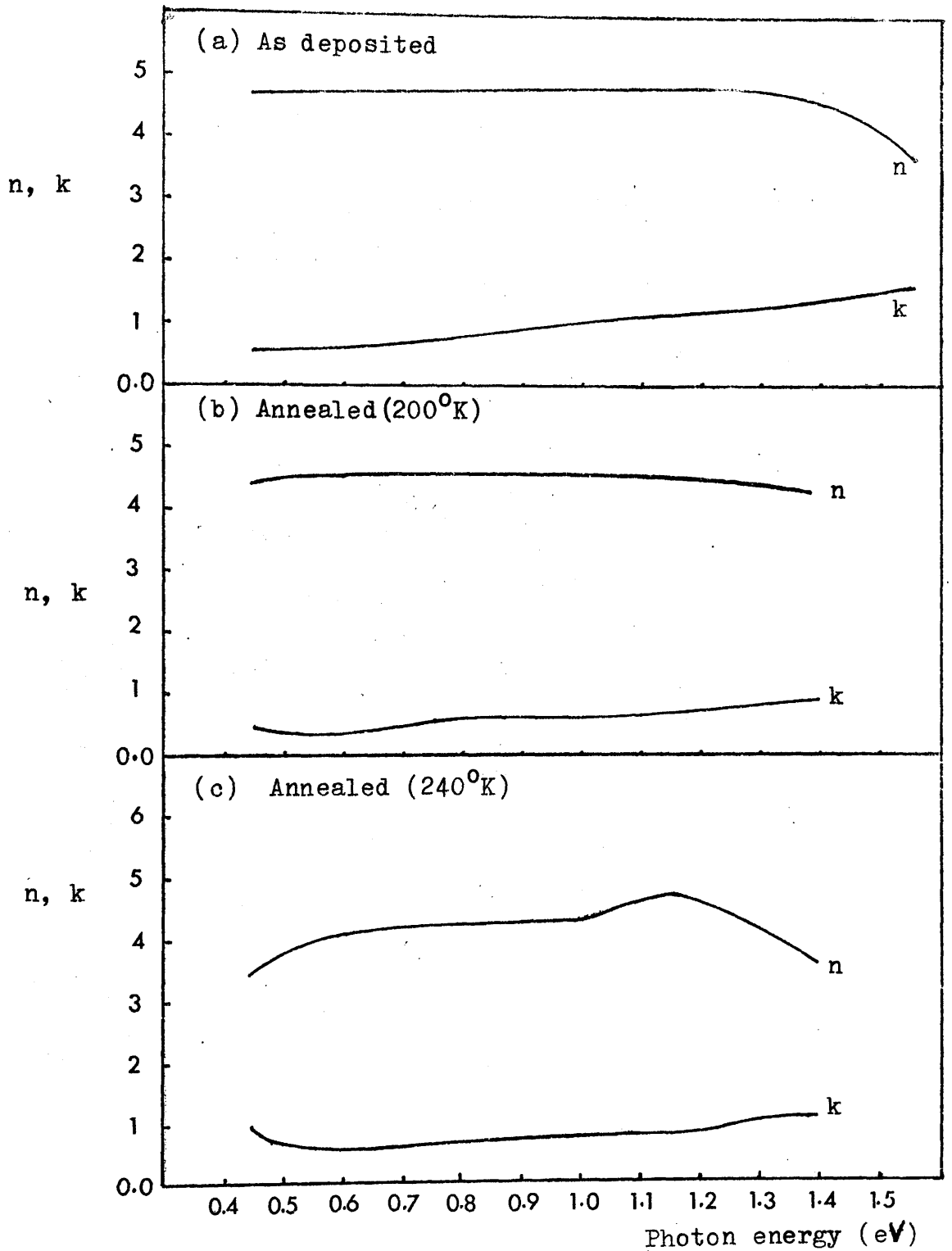for sample 7 (40.4 ∓ 1.6 at.% Bi).

Figure (5.10)   Variation of n and k with photon energy
for sample 11 (41.1 ∓ 2.5 at.% Bi).
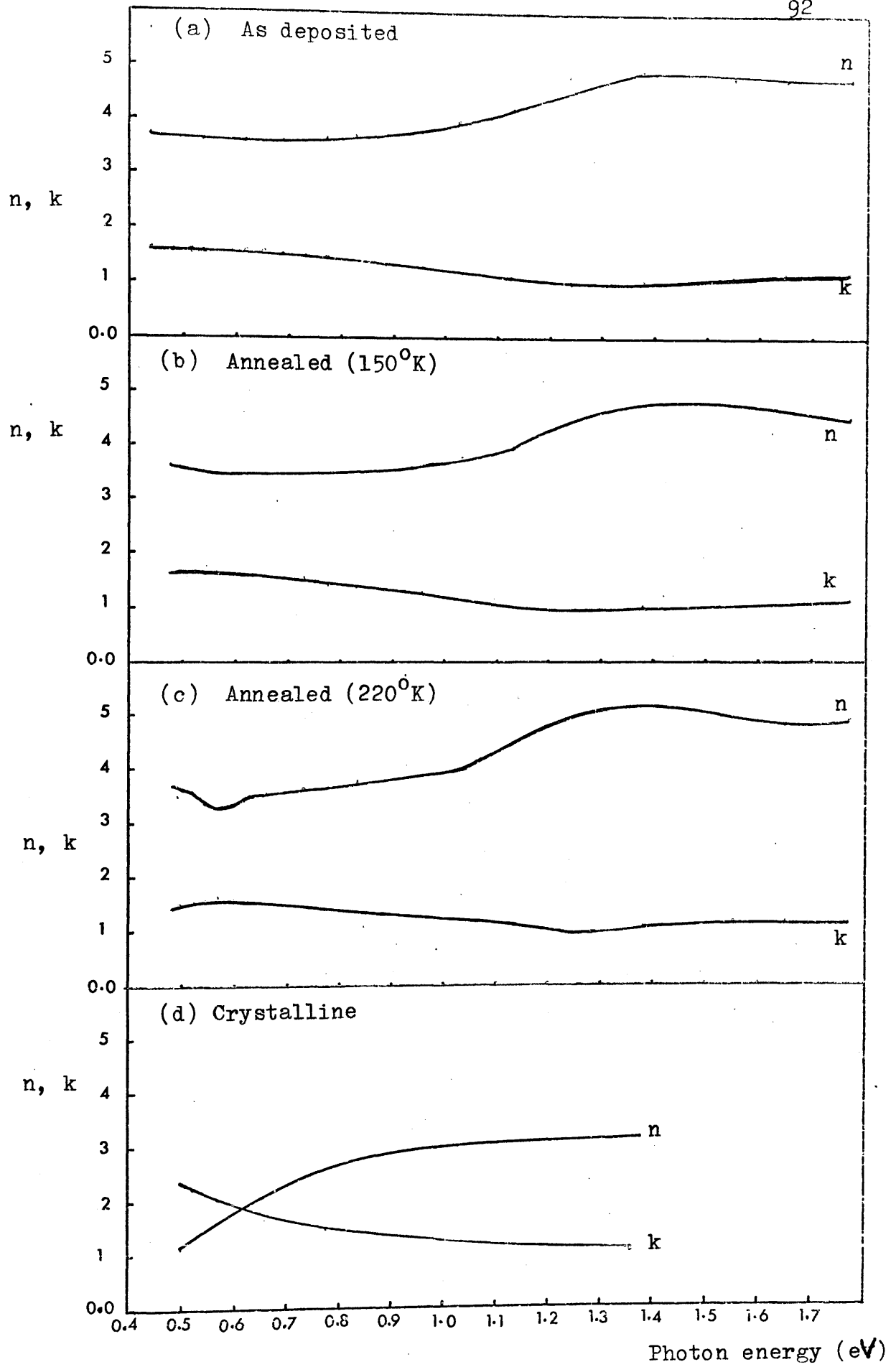
Figure (5.11)   Variation of n and k with photon energy for
sample 15 (48.4 ∓ 3.5 at.% Bi).

5.9   Optical Absorption in Amorphous Semiconductors

Electronic transitions between the valence and conduction bands in a crystal start at the absorption edge which corresponds to the minimum enery difference, Eg. between the lowest minimum of the conduction band and the highest maximum of the valence bands. These transitions are governed by the k-conservation selection rules whether being direct or indirect.   In amorphous semiconductors the k-conservation selection rule is relaxed because, near the band edges at least, $\Delta k \sim k$ and thus k is not a good quantum number.

The conductivity at frequency (ω), assuming that $kL \sim 1$ so that selection rules break down, is from the Kubo-Greenwood formula (Mott and Davis (1971)),

$$\sigma(\omega) = \frac{2\pi e^2 \hbar^2 V}{m^2 \omega} \int \left\{ f(E)-f(E+\hbar\omega) \right\} \; |D|^2 \; N(E)N(E+\hbar\omega)dE \quad (5.9.1)$$

where V is the volume per electron and D the matrix element for transitions occurring with energy $\hbar\omega$. If the matrix element D is assumed constant then equation (5.9.1) may be written as

$$\sigma(\omega) = \frac{1}{\omega} A \int_{E=0}^{\infty} \left\{ f(E)-f(E-\hbar\omega) \right\} \; N(E) \; N(E+\hbar\omega) \; dE \quad (5.9.2)$$

where

$$A = \frac{2\pi e^2 \hbar^2 V |D|^2}{m^2}$$

At $T = 0^{\circ}K$, The Fermi function $f(E)$ is such that

$$f(E) - f(E+\hbar\omega) = 1 \quad \text{for } E_f - \hbar\omega < E < E_f \quad \text{and}$$

$$= 0 \quad \text{for } E < E_f - \hbar\omega \quad \text{and} \quad E > E_f$$

consequently the integral becomes (for $T = 0^{\circ}k$)

$$\omega\,\sigma(\omega) = A \int_{E_f - \hbar\omega}^{E_f} N(E)\, N(E+\hbar\omega)\, dE$$

or

$$= A \int_{E_f}^{E_f + \hbar\omega} N(E-\hbar\omega)\, N(E)\, dE$$

If the energies are measured relative to the Fermi level (i.e. $E_f = 0$)

$$= A \int_{0}^{\hbar\omega} N(E-\hbar\omega)\, N(E)\, dE \qquad (5.9.3)$$

If the valence and conduction bands are assumed symmetric about the Fermi level then

$$N_c(E) = N_v(-E) = N(E)$$

Hence

$$\omega\,\sigma(\omega) = A \int_{0}^{\hbar\omega} N(E)\, N(\hbar\omega - E)\, dE \qquad (5.9.4)$$

For parabolic bands

$$N(E) = 0 \qquad 0 \leq E \leq E_g/2$$

$$= C\,(E - E_g/2)^{\frac{1}{2}} \qquad E < E_g/2$$

where $C = \dfrac{1}{2\pi^2} \left(\dfrac{2m}{\hbar^2}\right)^{3/2}$ for free electron bands

So $\quad \omega\sigma(\omega) = AC^2 \displaystyle\int_{E_g/2}^{\hbar\omega - E_g/2} (E - E_g/2)^{\frac{1}{2}} (\hbar\omega - E - E_g/2)^{\frac{1}{2}} dE \quad$ (5.9.5)

The limits of integration are determined by the zeros in $N(E)$ at the band edges. The transformation $E' = E - E_g/2$ gives

$$\omega\sigma(\omega) = AC^2 \int_{0}^{\hbar\omega - E_g} (E')^{\frac{1}{2}} (\hbar\omega - E_g - E')^{\frac{1}{2}} dE'$$

This integral is readily evaluated by Laplace transformation (Pipes (1946)) since the convolution integral for the Laplace transform is

$$L \left(\int_{0}^{t} h(u) h(t-u) \, du \right) = g^2(p)/p \qquad (5.9.6)$$

where $(L(h(t)) = g(p)$

Hence

$$L(\omega\sigma(\omega) / AC^2) = \left[L(\hbar\omega - E_g)^{\frac{1}{2}} \right]^2 /p$$
$$= L\left[\pi(\hbar\omega - E_g)^2 /8 \right]$$

That is

$$\omega\sigma(\omega) = AC^2 \frac{\pi}{8} (\hbar\omega - E_g)^2 \qquad (5.9.7)$$

or

$$(\hbar\omega)^2 \epsilon_2(\omega) = A'(\hbar\omega - E_g)^2 \qquad (5.9.8)$$

This result (Sutton (1975)) for the energy dependence of the absorption at the fundamental edge of an amorphous semiconductor was first published by Tauc et. al. (1965). A quadratic energy dependence of $\omega\sigma(\omega)$ has also been derived by Mott and Davis (1970) for states varying

linearly with energy near the extremities of the valence and conduction bands neglecting transitions in which both the initial and final states are localized. Their result is written as

$$\alpha \hbar \omega = B (\hbar \omega - E_g)^2 \qquad (5.9.9)$$

where α is the absorption coefficient and B constant of the order 10^5 cm^{-1} eV^{-1}. n the real part of the refractive index (N = n -ik) is assumed constant.

5.10   Energy Band Gaps

5.10.1   Energy Band Gap of Mg$_3$Bi$_2$

The optical band gap (E_g) for the amorphous and the annealed Mg-Bi alloys, table (1) were determined using relation (5.9.8). Plots of $\hbar \omega (\varepsilon_2)^{\frac{1}{2}}$ versus $\hbar \omega$ were used to estimate (E_g) which may represent an extrapolated rather than a real zero in the density of states. The energy gap of amorphous Mg$_3$Bi$_2$ was estimated from the op cal band gaps of samples 7 and 11 (40.4 and 41.1 at.% Bi), figures (5.12 and 5.13). These graphs are linear above 0.6 eV, this was determined from linear regression analysis of the data between 0.6 and 1.378 eV. From this analysis the gradient of $\hbar \omega (\varepsilon_2)^{1/2}$ versus $\hbar \omega$ was, figure (5.12), $(A')^{\frac{1}{2}} = 4.39$ giving $A' = 19.37$. The dependence of the optical absorption given by equation (5.9.8) is often written as (Mott and Davis (1971)) equation (5.9.9). Since

$$\alpha = \frac{\omega \varepsilon_2}{nc} \quad , \text{ equation (5.9.8) becomes}$$

$$\alpha \hbar \omega = \frac{A'}{\hbar nc} (\hbar \omega - E_g)^2 \qquad (5.10.1)$$

hence

$$B = 0.98 \times 10^6/n \ \text{cm}^{-1}. \ eV^{-1}$$

n varied from 3.86 to 4.9 for sample 7

$$B = 2.5 \times 10^5 \ \text{cm}^{-1} \ eV^{-1}$$

This is similar to values of B for other semiconductors obeying equation (5.9.9). Sutton (1975) found $B = 2.1 \times 10^5 \ \text{cm}^{-1}. \ eV^{-1}$ for an alloy 40.1 at.% Bi prepared by the co-evaporation method.

From intersections of the extrapolated lines figures (5.12 and 5.13), with the energy axes a mean optical band gap $E_g = 0.264 \mp 0.006$ eV is determined for the stoichiometric composition Mg_3Bi_2.

Sample Composition at.%	As Deposited		Annealed (I)		Annealed (II)	
	$E_g(1)$ eV	$E_g(2)$ eV	$E_g(1)$ eV	$E_g(2)$ eV	$E_g(1)$ eV	$E_g(2)$ eV
36.1	0.214	0.162	0.158	0.194	0.290	0.357
40.4	0.266	0.254	0.438	0.406		
41.1	0.268	0.266	0.427	0.329	0.325	0.304
48.4	0.128		0.141		0.170	

Table (1)   Optical band gap for the as deposited, and annealed Mg-Bi alloys. $E_g(1)$ and $E_g(2)$ refer to position 1 and 2 on the sample.

5.10.2 Variation of the Optical Band Gap with Composition

The optical band gaps for Mg-Bi alloys away from the

Figure (5.12) $\hbar\omega(\epsilon_2)^{\frac{1}{2}}$ versus photon energy $\hbar\omega$ for
the (as-deposited and annealed) amorphous
Mg-Bi alloy sample 7 (40.4 $\mp$ 1.6 at.Bi).
1, 2 refer to position 1 and position 2 on
the optical sample.
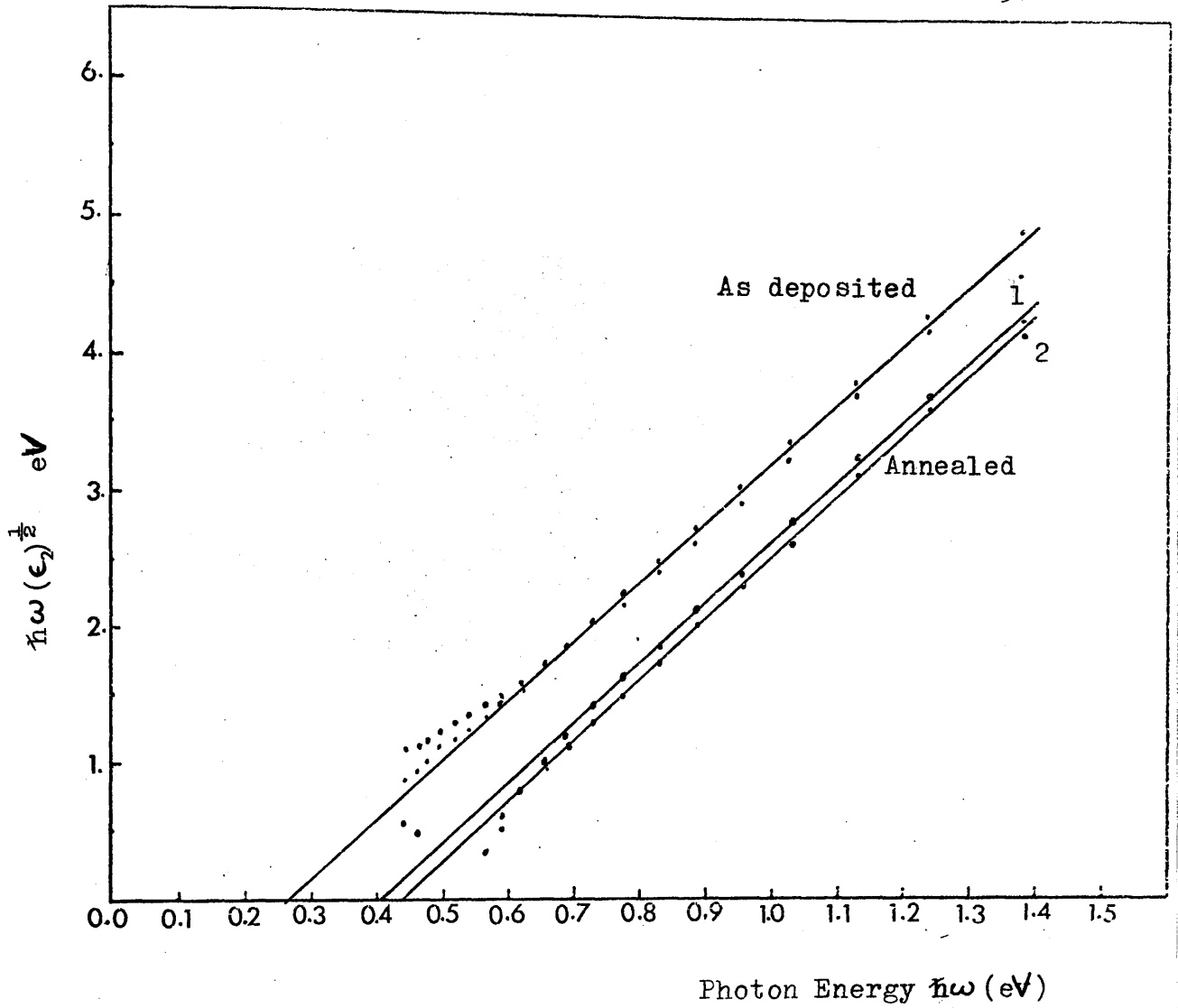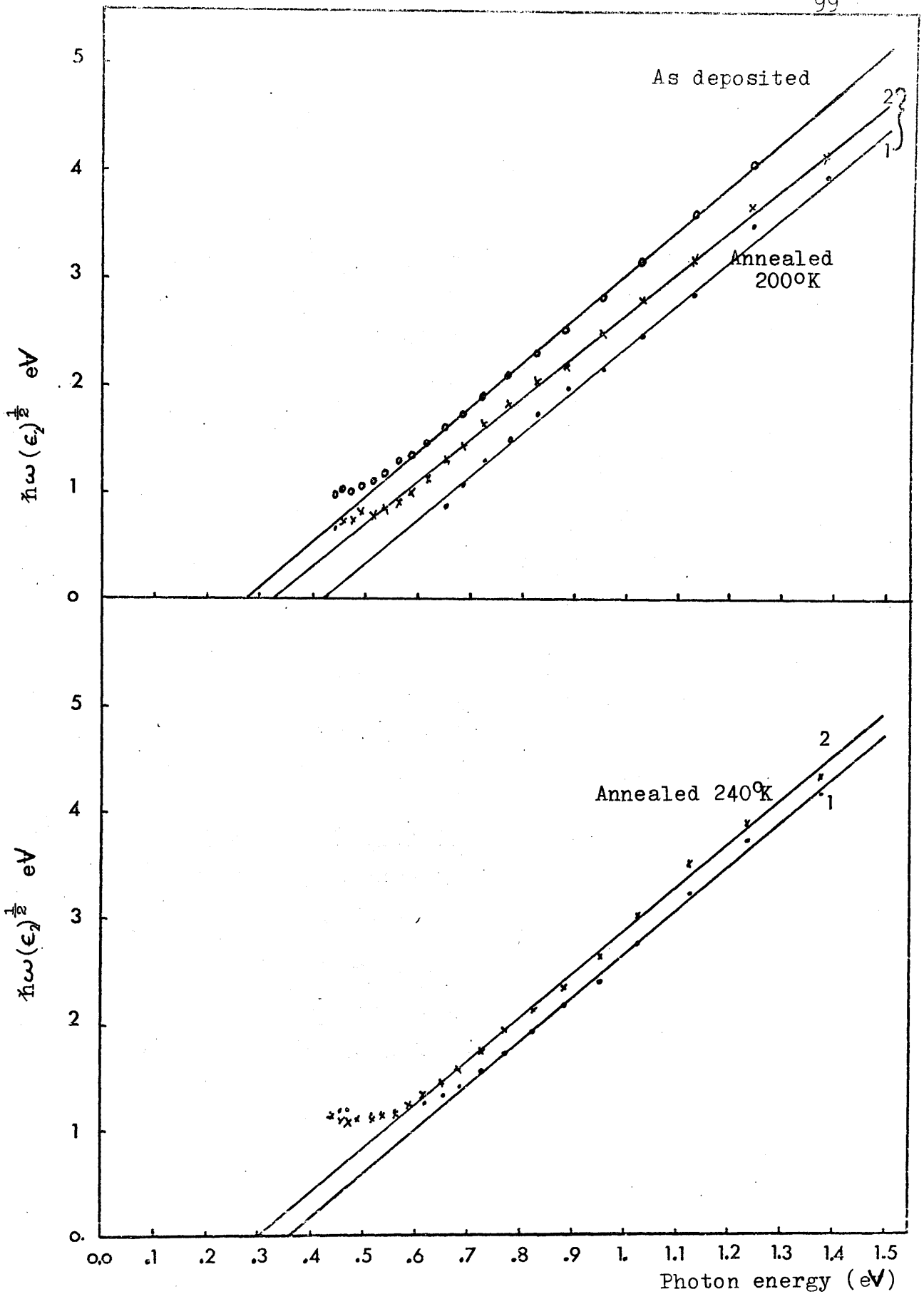
Figure (5.13) $\hbar\omega(\epsilon_2)^{\frac{1}{2}}$ versus photon energy $\hbar\omega$ the (As-deposited and annealed) amorphous Mg-Bi sample 11 (41.1 ∓ 2.5 at.% Bi)

1, 2 refer to position 1 and position 2 on the optical sample to illustrate the effect of transmission vatiations.

stoichiometric composition were determined following
the same analysis used for alloys close to Mg_3Bi_2.
The linear regression analysis was used to find the
best fit of the data points for two samples 14 and 15
(36.1 at.% Bi and 48.4 at.% Bi respectively). The
optical band gaps for these two samples are given
table (1). It is clear from those results that alloys
away from the stoichiometric composition do not have a unique
optical gap . Furthermore the optical
band gap varies as the composition departs from that
appropriate to Mg_3Bi_2. This change in the optical band
gap is due to the effect of excess of magnesium or bismuth
upon the absorption due to Mg_3Bi_2. Sutton (1975) reported
similar changes in the optical gap due to changes in comp-
osition.

5.10.3 Annealing Effects on Energy Gaps

In Chapter 4, we studied the behaviour of the d.c
resistivity of Mg-Bi alloys as a function of temperature.
It was shown that annealing the alloys to higher temper-
atures resulted in rearrangement, interdiffusion between
the atoms and produced more uniform films. In this
section we discuss the changes in optical band gap due
to annealing.

The procedure used to determined the optical band
gap for the annealed films followed the same pattern
setup for the amorphous alloys. The two samples 7 and
11 with composition close to Mg_3Bi_2 were annealed to

200°k. The common feature, figures (5.12,5.13) encount-
ered for both samples was that dramatic increase in the
optical gap from 0.264 eV to approximately 0.43 eV. The
two films were still amorphous at that point. Unfortunately
sample 7 cracked and flaked off during anneal state (II).
Sample 11 was annealed to 240°K (crystallization temperature
range 240 $\mp$ 10°K), the optical gap decreased at this stage,
with additional absorption at all energies observed, see
figure (5.4).

Optical band gaps for alloy films with compositions
away from the stoichiometric compound also varied due to
annealing. This variation in the gap was not strictly
similar to that observed in the case of alloys close to
Mg_3Bi_2. For bismuth or magnesium rich alloy films the
optical gap continued to increase while annealed to success-
ively higher temperature. During anneal stage II, a
metallic absorption was more pronounced for the magnesium
rich film (sample 14) particularly after this had crys-
tallized. From these observations it was clear that the
optical band gap was sensitive to the temperature treat-
ment after depositions.

5.11   Model Densities of States

Two model densities of states have been suggested to explain the electrical and the optical properties of the amorphous Mg-Bi alloys.   These are:

5.11.1   Rigid Band Model Density of States

Herrell and Ferrier (1969) and Sik (1974) have explained the properties of the amorphous Mg-Bi alloys in terms of a "rigid band model" figure (5.14).   In this model the shape of the energy bands is insensitive to compositional variation while the position of Fermi level varies within the mobility gap as the composition is changed.   For the intermetallic compound Mg_3Bi_2, The Fermi level is exactly in the middle of the gap.   Excess of either magnesium or bismuth causes the Fermi level to move towards the conduction band or the valence band respectively.   From his d.c. conductivity measurements, Sik estimated an activation energy 0.06 $\mp$ 0.01 eV for conduction at low temperature (T < 200°k) and 0.11 $\mp$ 0.01 eV for conduction at higher temperatures.   The conduction at high temperatures is due to carriers excited to non-localised   states above E_c' (or $_\wedge E_c$ below).   The activation energy corresponding to excitation of carriers to local-ized states at the band edge will only be observed when the Fermi level is near the centre of the gap (for compos-itions very close to the intermetallic compound).   For other compositions the Fermi level will be close to, or within the tail of, localized states at the band edge and
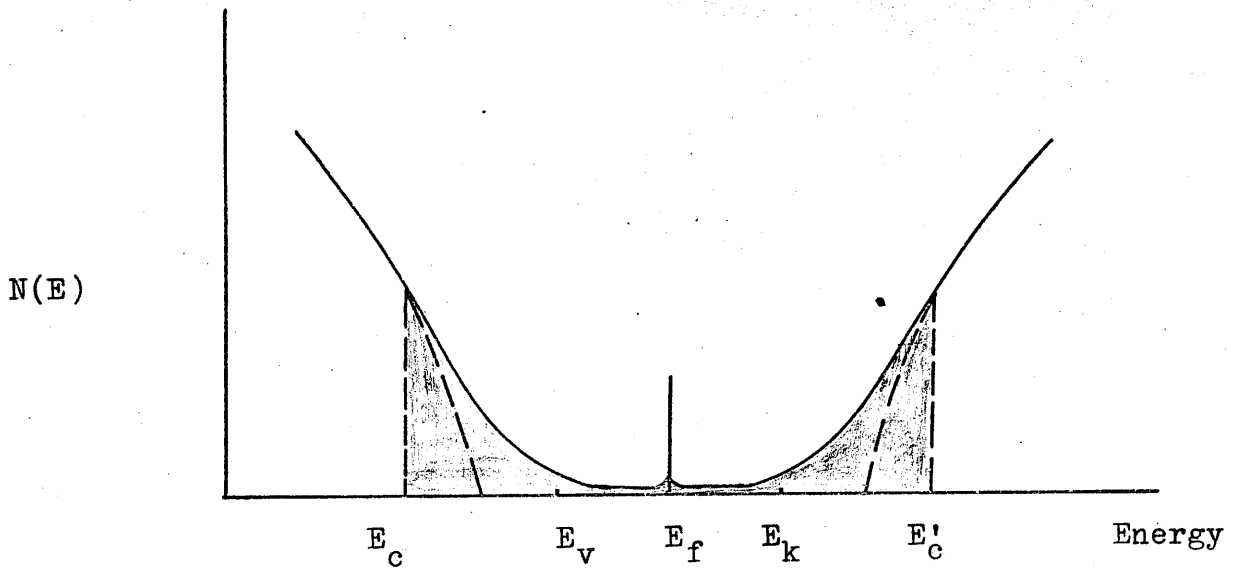
N(E)

Figure (5.14)   Rigid band model density of states
(Sik (1974)).

Localised states are shaded

therefore a direct transition, from conduction due to hopping between localized levels at the Fermi level to that due to carriers excited above the mobility edge at E_c', is expected. Sik gave an estimate of the density of state $N(E_f) \approx 10^{21}$ cm^{-3} ev^{-1}. As regards the annealing effects Sik suggested that this might produce changes in the density of states as shown in figure (5.15). The tails of localized states produced by a high degree of disorder, extend well into the gap. The band of levels near E_f may be caused by specific defects. Initial annealing processes may remove some specific defects causing a reduction in the size of the defect band which may shift the position of the Fermi level slightly. This shift could explain the irreversible changes noted during annealing stage I (a decrease in the activation energy and an increase in the conductivity) due to E_f moving closer to the tail of the localized states. Further annealing processes are expected to reduce the extent of the tails of localized states, figures (5.15,c,d). An increase in the activation energy and a decrease in conductivity could result from the changes in the density of states in figure (5,15,c,d).

5.11.2   Sutton's Interpretation

Sutton (1975) concluded from his optical studies of a number of Mg-Bi alloys that the "rigid band model" was not appropriate for these alloys. Instead this author suggested two model densities of states, outlined
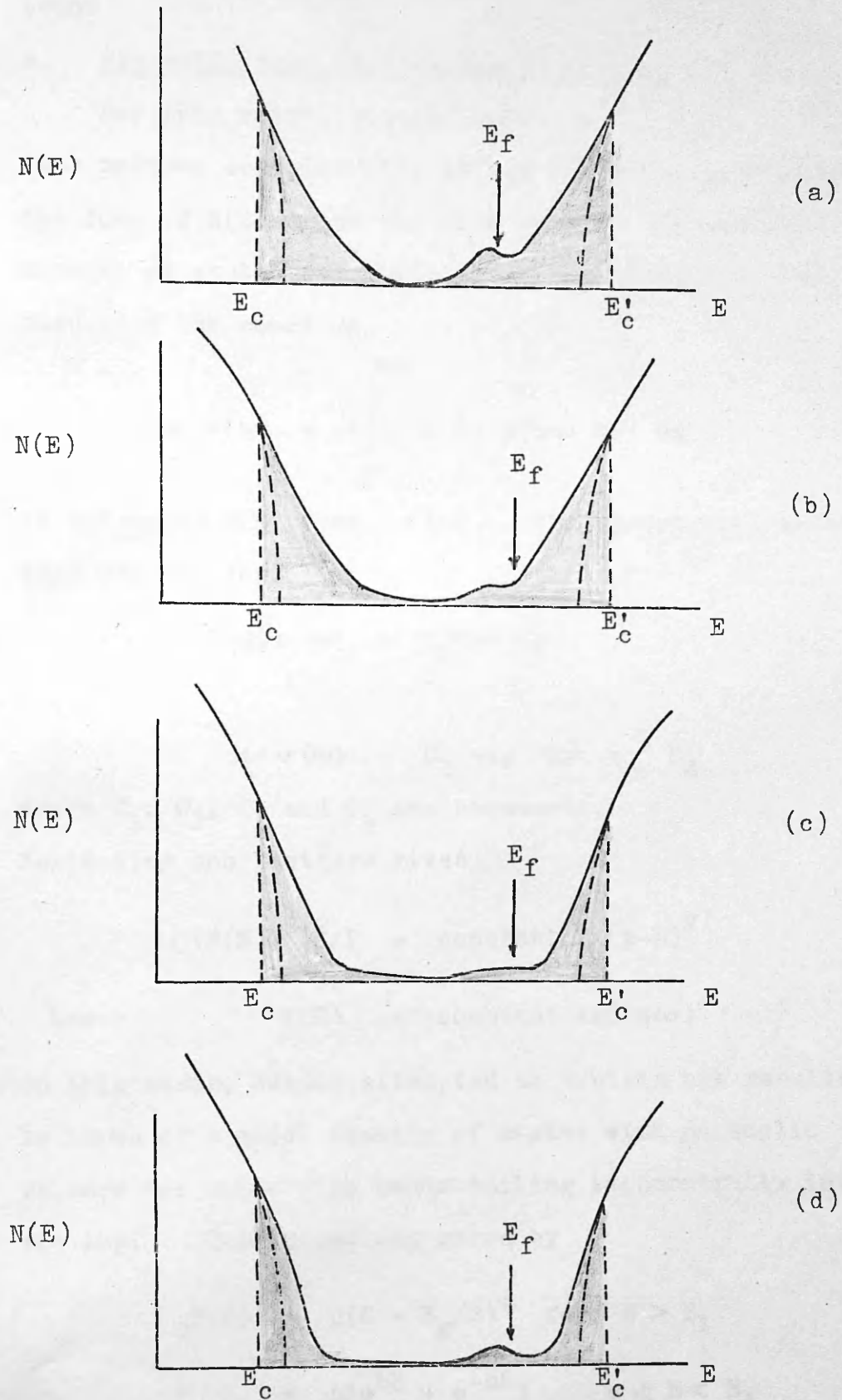
Figure (5.15) The effects of annealing on the density of
states (Sik (1974)). Curves a,b,c and d, show
the changes produced by annealing at successively
higher temperatures. Localised states are shaded

below

a. <u>Parabolic Band Tailing Exponentially into the Gap</u>

For this model, Sutton looked to the form of $\sigma(\omega)$ (the optical conductivity) at low energies to indicate the form of $N(E)$ below the band edges. He assumed a density of states symmetric about the Fermi level ($E_f = 0$), then used the equation

$$\omega \, \sigma(\omega) \; = \; A \int_0^{\hbar\omega} N(E) \, N(\hbar\omega - E) \; dE$$

to determine $N(E)$ from $\sigma(\omega)$. The exponential absorption edge was the form

$$\log_\Lambda^\omega \sigma(\omega) \; = \; C_1 \hbar\omega + C_2$$

or

$$\omega \, \sigma(\omega) \; = \; C_3 \exp \hbar\omega \; + \; C_4$$

where C_1, C_2, C_3 and C_4 are constants. Neglecting the last term gives

$$\left[L(N(E)) \right]^2 / P \; = \; \text{constant } P/(p-a)^2$$

hence

$$N(E) \; = \; \text{constant } \exp(\hbar\omega)$$

On this basis, Sutton attempted to explain his results in terms of a model density of states with parabolic valence and conduction bands tailing exponentially into the gap. This model was given by

$$N(E) \; = \; c(E - E_g/2)^{\frac{1}{2}} \quad \text{for} \quad E > E_1$$

$$= \; a(e^{bE} + e^{-bE}) \qquad 0 < E < E_1$$

with $N(E) = N(-E)$ and $E = 0$ at the centre of the gap.

a or b and E_g were two independent parameters while c was a scale factor.

b.   <u>Parabolic Bands with Gaussian Tails</u>

This is a semiquantitative model for the density of electron states in a system of randomly located hard-core scatterers and is applicable to disordered materials (Eggarter and Cohen (1970)) . In this model, the material is imagined to be divided into cells of volume L^3 where L is the spatial extent of a typical wave packet. The number of scatterers in each cell is treated as a random quantity and the total density of electron states is a sum of the contributions from the individual cells. The total density of states derived from this model can be written as

$$n(E) = c' F b'(e - E_g/2) \quad , \text{ for one band,}$$

where
$$F(\varepsilon) = (2\pi)^{-\frac{1}{2}} \int_0^\infty Z^{\frac{1}{2}} \exp -(\varepsilon - Z)^2/2 \ dZ$$

and c', b', E_g are constants. ε is an energy parameter. For $\varepsilon \geq 2$, $F(\varepsilon) = \varepsilon^{\frac{1}{2}}$ giving the normal parabolic energy dependence away from the band edges while at low energies ($\varepsilon < o$) the asymptotic form is

$$F(\varepsilon) = \exp(-\varepsilon^2/2) / \left| 2\varepsilon \right|^{3/2} \quad \text{and}$$

produces a Gaussian tail.

In figure (5.16), the two models are illustrated for a number of Mg-Bi alloys less than, close to and greater than 40 at.% Bi.
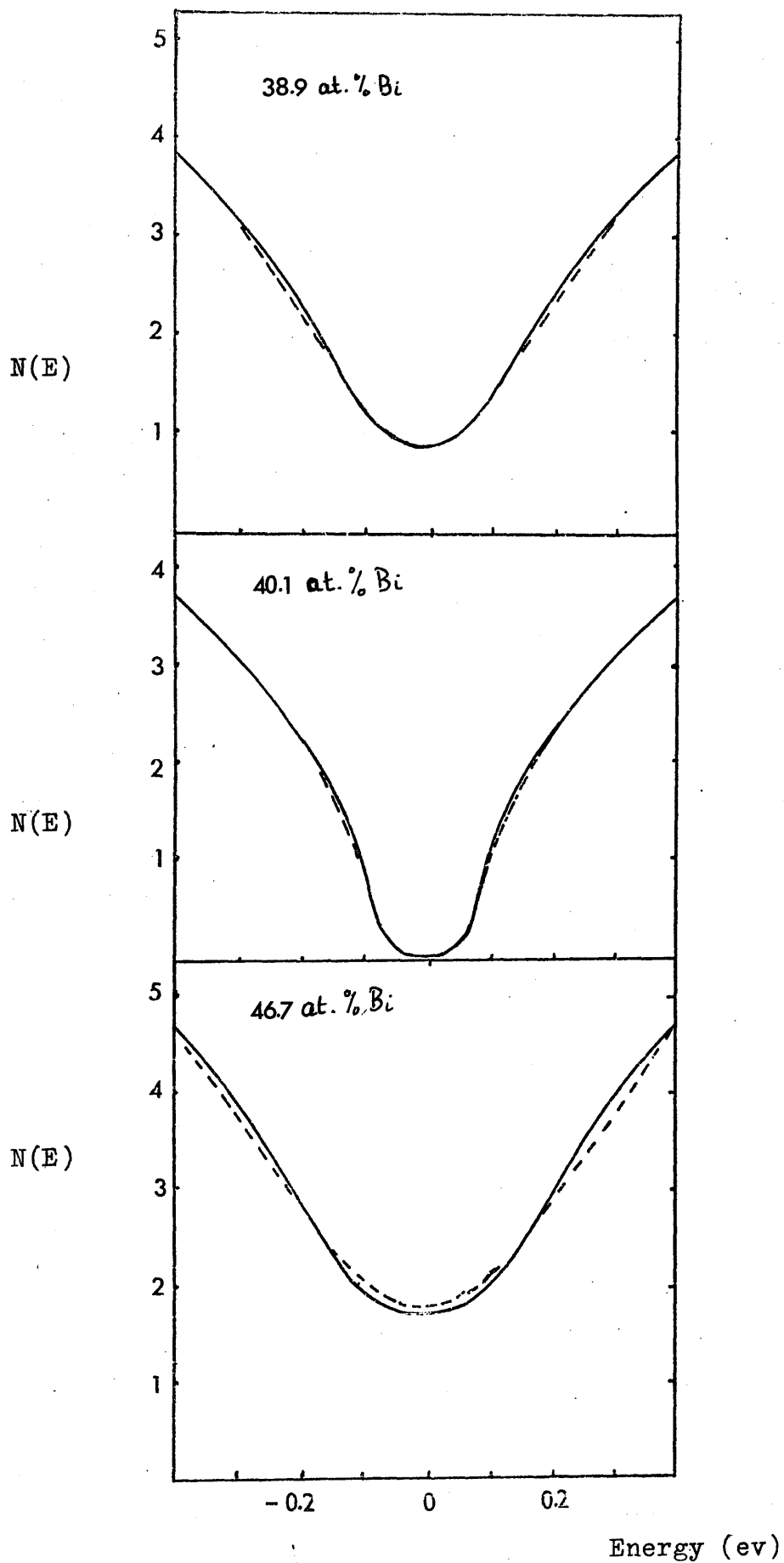
Figure (5.16)   Model densities of states (Sutton (1975)).
Solid line from model (a)
Dotted line from model (b)

5.12   Discussion of the Optical Results

From the early data available, the optical band gap
for alloys close to the intermetallic compound was 0.7 eV
(Sik and Ferrier (1974))   and 0.152 $\mp$ 0.005 eV (Sutton
(1975)) .   These authors found that the optical gap,
although significantly different, was invariant with
small variations in compositions about the intermetallic
compound.

Such a large and disturbing difference between the
two optical band gaps reported earlier was a serious
discrepancy.   The task of this work has been to try to
resolve this problem.   We have studied the d.c. conduct-
ivity and the optical properties of the Mg-Bi alloys pre-
pared by the coevaporation technique.   In Chapter 4, the
densities of the Mg-Bi alloys and the behaviour of the
d.c. resistivity were in general agreement with most of
the earlier results.   This has enabled us to compare the
optical results with those reported by Sik (1974)   and
Sutton (1975).   From our optical measurements we have
determined a new optical band gap   =   0.264 $\mp$ 0.006 eV which is
invariant with composition within $\mp$ 2 at.% Bi   but
becomes sensitive to excess of either magnesium or bismuth.
A dramatic increase in the optical gap has been observed
as a result of annealing (prior to crystallization).   In
the light of these new results and the electrical results
presented in Chapter 4 we may comment on the data for the
optical band gap.   Sik and Ferrier (1974)   used an approxi-
mation to calculate the absorption coefficient which is

known to be most seriously in error at low energies
causing an overestimate of the energy gap.   (Sutton
(1975) measured the as deposited film absorption in
the range E < 1.2 ev where the additional absorption
is particularly significant at very low energies.   It
appears that this disguised the true energy gap.

As regards the model density of states outlined
earlier, ·   ι some of the electrical and the optical
results can be explained in terms of these model densities
of states.   But the new evidence of the dramatic changes
in the optical band gap and the additional attenuation
below 0.6 ev (which can be considered as states on the
bands tails) makes it difficult to distinguish between model

densities of states.

Appendix A

The computer programme used to determine the real and the imaginary parts of the complex refractive index (n and k) from T_1 and T_2 of two different thicknesses of Mg-Bi alloy films is given.

```
      REAL N,K1,K2,KB
      READ (5,10) I,D1,D2
10    FORMAT (I3,2F5.3)
      WRITE (6,15)
15    FORMAT (8H1 WVLGTH,4X,6HENERGY,7X,1HN,8X,2HKB,8X,2HK2,6X,5HALPHA,
     1 7X,1HY,8X,2HE2,7X,5HSIGMA)
      DO 200 J = 1,I
      READ (5,20) W,T1,T2
20    FORMAT (F5.3, 2F6.4)
      L = 0
      N = 1.0
30    N = N + 0.1
      L = L + 1
      IF (L.GE.70) GO TO 200
      K1 = SOLVE (N,D1,T1,W)
      K2 = SOLVE(N,D2,T2,W)
      IF (N-1.1) 35,35,40
35    DELTA = K1-K2
      GAMMA = DELTA
      GO TO 30
40    DELTA = K1-K2
      IF (ABS(DELTA)-ABS(GAMMA)) 50,45,45
45    GAMMA = DELTA
      GO TO 30
50    GAMMA = DELTA
      N = N + 0.1
      L = L + 1
      K1 = SOLVE (N,D1,T1,W)
      K2 = SOLVE(N,D2,T2,W)
      DELTA = K1-K2
      IF (ABS(DELTA)-ABS(GAMMA)) 50,55,55
55    CONT = N
      N = N - 0.21
      N = 0
60    GAMMA = DELTA
      N = N + 0.01
      M = M + 1
      IF (M.GE.21) GO TO 120
      K1 = SOLVE (N,D1,T1,W)
      K2 = SOLVE(N,D2,T2,W)
      DELTA = K1-K2
      IF (M.GE.2) GO TO 65
      GO TO 60
65    IF (ABS(DELTA)-ABS(GAMMA)) 60,70,70
70    N = N-0.021
      M = 0
75    GAMMA = DELTA
      N = N+ 0.001
      M = M + 1
      IF (M.GE.21) GO TO 120
      K1 = SOLVE (N,D1,T1,W)
      K2 = SOLVE(N,D2,T2,W)
      DELTA = K1-K2
      IF (M.GE.2) GO TO 80
      GO TO 75
80    IF (ABS(DELTA)-ABS(GAMMA)) 75,100,100
100   EN = 1.24/W
      IF (K1.LE.0.0) GO TO 140
      IF (K2.LE.0.0) GO TO 140
      KB = 0.5*(K1+K2)
      ALPHA = 12.5664*KB/W
      Y = SQRT(EN*ALPHA)
      E2 = 2.0*N*KB

      SIGMA = EN*SQRT(E2)
      WRITE (6,110) W,EN,N,KB,K2,ALPHA,Y,E2,SIGMA
110   FORMAT (9(F8.3,2X))
      N = CONT
      GO TO 30
120   WRITE (6,130) N,K1,K2
130   FORMAT (7HFAULT 1,3(F8.3,2X))
      GO TO 30
140   WRITE (6,150) N,K1,K2
150   FORMAT (7HFAULT 2, 3(F8.3,2X))
      GO TO 30
200   CONTINUE
      STOP
      END
```

```fortran
      FUNCTION SOLVE (N,DN,T,W)
      REAL N,K,N2
      L = 1
      K = 0.0
      N2 = TWO(W)
      BETA = 12.5664*N*DN/W
      RO = ((N2-1.0)*(N2-1.0))/((N2+1.0)*(N2+1.0))
      A1 = N - 1.0
      A2 = N + 1.0
      A3 = N - N2
      A4 = N + N2
30    SQ = K*K
      A5 = N*N + SQ
      A = (A1*A1+SQ)*(A4*A4+SQ)
      B = (A2*A2+SQ)*(A3*A3+SQ)
      C = 2.0*((A5-1.0)*(A5-N2*N2)+4.0*SQ*N2)
      D = 4.0*K*(N2-1.0)*(A5+N2)
      E = (A2*A2+SQ)*(A4*A4+SQ)
      F = (A1*A1+SQ)*(A3*A3+SQ)
      G = 2.0*((A5-1.0)*(A5-N2*N2)-4.0*SQ*N2)
      H = 4.0*K*(N2+1.0)*(A5-N2)
      B1 = E-RO*B
      B2 = (G-RO*C)*COS(BETA)-(H+RO*D)*SIN(BETA)+16.0*N2*A5*(1.0-RO)/T
      B3 = F-RO*A
      B4 = B2*B2-4.0*B1*B3
      IF (B4.LE.0.0) GO TO 60
      Z = (B2 + SQRT(B4))/(2.0*B1)
      Z = ABS(Z)
      TRY = (ALOG(Z)*W)/(12.5664*DN)
      IF (ABS(TRY-K).LE.1.0E-4) GO TO 50
      L = L+1
      K = TRY
      GO TO 30
50    SOLVE = TRY
      GO TO 70
60    Z = B2/(2.0*B1)
      Z = ABS(Z)
      SOLVE = (ALOG(Z)*W)/(12.5664*DN)
70    RETURN
      END




      FUNCTION TWO(X)
      FIRST = (1.023798*X*X)/(X*X-3.77588E-3)
      SECOND = (1.058264*X*X)/(X*X-1.22544E-2)
      THIRD =(5.280792*X*X)/(X*X-321.3616)
      TWO = SQRT(1.0+FIRST+SECOND+THIRD)
      RETURN
      END
```

R E F E R E N C E S

1. F. Abeles, Advanced Optical Techniques (Edited by A.C.D. Van Heel), North-Holland, Amsterdam (1967).

2. L. Banyai, Physique des Semiconducteurs (Ed. M. Hulin) p.417, Dunod, Paris (1964).

3. K.H. Berhrndt, Physics of Thin Films (Advances in Research and Development), Vol. 3 (1966) Ed. G. Hass and R.E. Thun.

4. T.M. Dauphinee and H. Preston-Thomas, Rev. Sci. Instrum., Vol. 25, p.884 (1954).

5. T.P. Eggater and M.H. Cohen, Phys. Rev. Letters, Vol. 25, p.807 (1970).

6. R.P. Ferrier and D.J. Herrell, Phil. Mag. Vol. 19, p.853 (1969).

7. R.P. Ferrier, J.M. Prado and M.R. Anseau, J. Non-Crystalline Solids, Vol. 8-10, p. 788 (1972).

8. A.I. Gubanov, Quantum Electron Theory of Amorphous Conductors, Consultants Bureau, New York (1965).

9. H.L. Hackforth, Infrared Radiation, McGraw-Hill (1960).

10. R.A. Heising, Quartz Crystals for Electrical Circuits, Van Nostrand, Princeton, New Jersey, (1946).

11. D.J. Herrell, Ph.D. Thesis, University of Cambridge, (1969).

12. B.R. Ilschner and C. Wagner, Acta Metall. Vol. 6, p.712 (1958).

13. A.F. Ioffe and A.R. Regel, Prog. Semicond. Vol. 4, p.237, (1960).

14. P.O. Nilsson, Applied Optics, Vol. 7, p.426 (1968).

15. N.F. Mott and E.A. Davis, Electronic Processes in Non-Crystalline Materials, Clarendon Press, Oxford, (1971).

16. A.M. McLeod and A.R. Long (to be published).

17. I.H. Malitson, H. Opt. Soc. Am., Vol. 52 p.1377 (1962).

18. D.J. Pacey, Vacuum, Vol. 9, p.201, (1959).

19. L.A. Pipes, Applied Mathematics for Engineers and Physicists, McGraw-Hill, New York (1946).

20. M.J. Sik and R.P. Ferrier, Phil. Mag. Vol. 29, p.877 (1974).

21. M.J. Sik, Ph.D. Thesis, University of Cambridge, unpublished (1969)

22. C.M. Sutton, Solid State Comm. Vol. 16, p.327 (1975).

23. C.M. Sutton, Ph.D. Thesis, Victoria University of Wellington, New Zealand, (1975).

24. J.H. Slowik and F.C. Brown, Phys. Letters, Vol. 29, p.934 (1972).

25. J. Tauc, A.Abraham, L. Pajova, R. Grigorovici and A. Vancu, Physics of Non-Crystalline Solids, Proc. Intern. Conf. Delft, (1964), North Holland, Amsterdam (1965).

26. J.Tauc, Amorphous and Liquid Semiconductors, Ed. by J. Tauc, Plenum Press (.1974).